APPLICATION OF CONVENTIONAL WELL LOGS FOR ROCK CLASSIFICATION TO ENHANCE CHARACTERIZATION OF HETEROGENEITY IN CARBONATE FORMATIONS

A Dissertation

by

MEHRNOOSH SANEIFAR

Submitted to the Office of Graduate and Professional Studies of
Texas A&M University
in partial fulfillment of the requirements for the degree of

DOCTOR OF PHILOSOPHY

Chair of Committee,	Zoya Heidari
Committee Members,	A. Daniel Hill
	Walter Ayers
	Michael Pope
Head of Department,	A. Daniel Hill

May 2015

Major Subject: Petroleum Engineering

ABSTRACT

Characterization of carbonate reservoirs is challenging as the result of heterogeneous distribution of petrophysical properties and mineralogy. Common rock classification techniques are strongly dependent on core measurements, whereas core data are usually sparse and inadequate for reliable heterogeneity analysis. I introduce an integrated rock classification workflow, based on conventional well logs and core data, which incorporates geological attributes and petrophysical, compositional, and elastic properties estimated from conventional well logs. The proposed rock classification method may enhance (a) assessment of petrophysical and compositional properties, (b) prediction of acid stimulation performance, (c) selection of completion depth intervals, and (d) production enhancement strategies in carbonate formations.

In the proposed workflow, I incorporate diagenetic and depositional attributes by taking into account the impact of shapes of different pore types and minerals in each geological facies on resistivity logs and elasticity. Rock quality and rock-fluid quality indices are introduced to take into account the impact of dynamic petrophysical properties, rooted in diagenesis, for real-time rock classification. Furthermore, I apply an analytical technique for the depth-by-depth assessment of elastic rock properties, as well as interparticle and intraparticle porosity, in a limiting case where shear-wave slowness measurements are not available. In addition, I take advantage of Mercury Injection Capillary Pressure (MICP) measurements, where available, to characterize pore-throat radius distribution and modality using a multi-modal Gaussian function. I finally use supervised and unsupervised learning techniques to classify rock types based on static and dynamic petrophysical, compositional, and elastic properties.

I successfully applied the proposed workflow in four carbonate formations, Hugoton, Happy Spraberry, Veterans, and SACROC fields. Although the main focus of this dissertation is carbonate rock classification, I also introduced rock classification techniques based on conventional well logs in organic-rich shale formations. The reliability of these techniques was investigated in the Haynesville Shale. The identified petrophysical rock classes in all field cases were validated using core-derived rock classes, lithofacies descriptions, and thin-section images, where available. The results showed improvement in the assessment of petrophysical properties, compared to the conventional assessment techniques.

The contributions of the proposed techniques include (a) incorporation of geological and petrophysical attributes for an integrated rock classification, (b) application of conventional well logs for the depth-by-depth assessment of elastic moduli and interparticle and intraparticle porosity, applicable where acoustic well logs are not available, (c) simultaneous characterization of pore modality and pore-throat radius distribution for rock classification in carbonate formations.

DEDICATION

To my parents, Roza and Majid, for their unconditional love and encouragement.

To my brothers, Daryoush and Soroush, who were always there for me during the difficult times with their heartwarming support that kept me going.

ACKNOWLEDGEMENTS

First and foremost, my wholehearted appreciation goes to my parents for giving me life and etiquettes to live it to the best. Thanks for teaching me to be strong and to believe in myself that I can achieve the impossible. Without you, I would have not been where I am today.

Completion of this Ph.D. would have not been possible without the support of my dear supervisor. I would like to express my deepest gratitude to Dr. Zoya Heidari for her motivation and invaluable technical guidance during my Ph.D. Her generosity with her time and her absolute passion for providing enriching feedback for excelling a progressing research were truly inspirational. Also, I would like to extend my sincere appreciation to Dr. A. Daniel Hill, Dr. Walter Ayers, and Dr. Michael Pope for serving as my committee members and for their insightful technical comments and assistance during my Ph.D. study.

Special thanks go to Gia Alexander for her administrative assistance and professional editorial inputs for improving my papers and dissertation. It was a great privilege to have her in our research team and to receive her valuable feedback on my technical writing.

I would like to thank all my friends at Texas A&M University and my teammates in the Multi-Scale Formation Evaluation research group for their continuous support and encouragement. Special thanks go to Alvaro Aranibar, Clotilde Chen Valdes, Emmanuel

Oyewole, and Roy Conte, the co-authors of my papers. I deeply appreciate their collaboration and technical contribution to my papers.

A note of special gratitude goes to Dr. Yunghe Sun, Editor-in-Chief, Dr. Kyle Spikes and Dr. Chicheng Xu, Associate Editors, and the four anonymous reviewers of the *SEG Interpretation Journal* for their excellent technical and editorial feedback, which improved the first version of my paper. I also would like to thank Dean Wehunt, the Executive Editor, and four anonymous reviewers of the *SPE Production & Operations Journal* for their valuable technical and editorial comments on my paper. Furthermore, I am grateful to Michael L. Sweet, AAPG Editor, Terrilyn Olson, AAPG Senior Associate Editor, AAPG reviewers, Jack Breig, Dario De Benedictis, and Raymond P. Sorenson, and AAPG Consulting Geologist, Frances Plants Whitehurst, for their constructive editorial feedback that improved my paper in the *AAPG Bulletin*. Special thanks go to Mark Linroth for many technical discussions and valuable feedback on my research related to the impact of formation heterogeneity on Water-Alternating-Gas injectivity problems.

My summer internship at the Chevron Energy Technology Company was a valuable educational experience that helped me advance my knowledge and research in the areas of petrophysics, rock classification, and characterization of carbonate formations. I am very grateful to my mentors, Dr. Mark Skalinski and Dr. Paul Theologou, and to my supervisor, Dr. Emmanuel Toumelin for this enriching opportunity, and of course my Ph.D. supervisor, Dr. Zoya Heidari, for kindly approving me to go to this internship.

I would like to express my gratitude to the financial sponsors of the research conducted in this dissertation. The work was funded by the Texas A&M University Joint Industry Research Program on Multi-Scale Formation Evaluation, jointly sponsored by Aramco Services Company, BHP Billiton, BP, Chevron, ConocoPhillips, and Devon Energy, as well as the Crisman Institute for Petroleum Research at the Harold Vance Department of Petroleum Engineering.

NOMENCLATURE

a	Archie's Winsauer factor
$Britt_{index}$	Rock brittleness index, %
B^{∞}	Bulk volume saturated by mercury at infinite pressure
c	Count of the differences in the adjacent rock classes
C	Covariance matrix
C_{clay}	Volumetric concentration of clay, fraction
C_H	Spatial heterogeneity coefficient
C_k	Organic carbon percentage in kerogen, %
$C_{minerals}$	Volumetric concentration of minerals, fraction
E	Rock effective Young's modulus, GPa
E_{max}	Maximum Young's modulus, GPa
E_{min}	Minimum Young's modulus, GPa
E_{Britt}	Normalized Young's modulus, fraction
G	Shape factor of capillary pressure curve
h	Lag distance, ft

H	Vertical calculation domain length, ft
i	Individual rock component
I_{clay}	Clay concentration index, fraction
I_{RS}	Resistivity separation Index, fraction
$\bar{k}$	Average permeability, md
k	Permeability, md
K	Bulk Modulus, GPa
K_i	Bulk modulus of rock component, GPa
K^*_{sc}	Rock effective bulk modulus, GPa
L	Horizontal calculation domain length, ft
L_p	Demagnetizing factor
m	Archie's porosity exponent
n	Archie's saturation exponent
N	Total number of rock components/data pairs/data points
P^{*i}	Shape factor
P_c	Capillary pressure measurement, psi

P_d	Displacement pressure, psi
Q^{*i}	Shape factor
r	Pore-throat radius, μm
R^{*i}	Shape factor
R_{Deep}	Deep electrical resistivity, ohm
$R_{Shallow}$	Shallow electrical resistivity, ohm
$R_{sim.}$	Simulated resistivity, ohm
$R_{measured}$	Measured resistivity, ohm
S_{Hg}	Mercury saturation, %
$\left(S_{Hg}\right)_{inc}^{\mathrm{mod}el}$	Modeled incremental mercury saturation, %
$\left(S_{Hg}\right)_{inc}^{\mathrm{meas}}$	Incremental mercury saturation, %
S_w	Water saturation, fraction
T	Total number of the pore-throat radius modes
$T^{(i)}$	Wu’s tensor
V	Eigenvector matrix
V^T	Transpose of eigenvector matrix

$\overline{w}$	Average fracture width, in
w_i	Ideal fracture width, in
$(wk_f)_0$	Acid fracture conductivity under zero closure stress, md-ft
wk_f	Overall acid fracture conductivity, md-ft
x_i	Volumetric concentration of rock component, fraction
$\bar{x}$	Mean values of x variables
$x_{inter\text{-}por}$	Volumetric concentration of interparticle pores (porosity), fraction
$x_{intra\text{-}por}$	Volumetric concentration of intraparticle pores (porosity), fraction
y_i	Depth-by-depth measurements/estimated properties from well logs
$\bar{y}$	Mean values of y variables
z_i	Individual data point
V_{bk}	Kerogen bulk volumetric concentration, fraction
V_{bnk}	Non-kerogen bulk volumetric concentration, fraction
Δt	Compressional-wave slowness, μs/ft
Γ	Interfacial tension
$\gamma(h)$	Variance

Λ	Matrix of eigenvalues
λ_x	Horizontal correlation length, ft
$\lambda_{x,D}$	Dimensionless horizontal correlation length
λ_z	Vertical correlation length, ft
$\lambda_{z,D}$	Dimensionless vertical correlation length
μ_i	Shear modulus of rock component, GPa
μ^*_{sc}	Rock effective shear modulus, GPa
ϕ	Porosity, fraction
ϕ_k	Gas-filled kerogen porosity, fraction
ϕ_{nk}	Non-kerogen porosity, fraction
ϕ_t	Total porosity, fraction
ρ_b	Bulk density, g/cm^3
ρ_{bnk}	Non-kerogen bulk density, g/cm^3
ρ_k	Kerogen density, g/cm^3
ρ_{grain}	Grain density, g/cm^3
ρ_{hc}	Hydrocarbon density, g/cm^3

ρ_{nk}	Non-kerogen matrix density, g/cm^3
ρ_w	Water density, g/cm^3
σ	Standard deviation
σ_c	Closure stress, psi
σ_D	Dimensionless standard deviation
σ_i	Electrical conductivity of rock component, mho/m
σ^*_{sc}	Rock effective electrical conductivity, mho/m
υ	Poisson’s ratio, fraction
υ_{max}	Maximum Poisson’s ratio, fraction
υ_{min}	Minimum Poisson’s ratio, fraction
υ_{Britt}	Normalized Poisson’s ratio, fraction
θ	Contact angle

ACRONYMS

CPU	Computer Processing Unit
ECS	Elemental Capture Spectroscopy
DEM	Differential Effective Medium
EOR	Enhanced Oil Recovery
FC	Fluid Corrected
GR	Gamma Ray, GAPI
KNN	*k*-Nearest Neighbors algorithm
MICP	Mercury Injection Capillary Pressure
NN	Artificial Neural Network
PEF	Photoelectric Factor, b/elec
RC	Rock Class
RFQI	Rock Fluid Quality Index
RQI	Rock Quality Index
SACROC	Scurry Area Canyon Reef Operators Committee
SCA	Self-Consistent Approximation

SEM	Scanning Electron Microscope
SOM	Self-Organizing Map
TOC	Total Organic Content, %
UN_NN	Unsupervised Artificial Neural Network
WAG	Water-Alternating-Gas Injection
XRD	X-Ray Diffraction

TABLE OF CONTENTS

Page

LIST OF FIGURES

LIST OF TABLES

Page

CHAPTER I

INTRODUCTION

Reservoir characterization can be challenging in heterogeneous carbonate formations due to vertical and lateral variations of petrophysical properties and mineralogy in these formations. This dissertation introduces an integrated rock classification scheme for characterizing formation heterogeneity in carbonate reservoirs. The introduced rock classification technique incorporates geological lithofacies interpreted from core (where available) with estimates/measurements of static and dynamic petrophysical properties, mineralogy, and elastic properties based on conventional well logs. The integrated rock classification method can be applied for optimizing completion design and production enhancement in carbonate formations. Although the main focus in this dissertation is carbonate rock classification, I also introduce similar well-log-based rock classification techniques that are applicable in organic-rich shale formations for enhanced selection of fracture locations and well development.

1.1 Background

Post-depositional processes (i.e., diagenesis) strongly impact pore structure and mineralogy in carbonate formations. Grain dissolution, cementation, and compaction can re-arrange grain packing and pore shape/size distribution. Mineralogy can be altered by dolomitization and recrystallization of aragonite and calcite (Ahr 2008). The aforementioned mechanisms result in complex pore structure and heterogeneous distribution of petrophysical properties (e.g., permeability), as well as mineralogy and elastic properties in carbonate formations. A reliable characterization of the distribution of these rock properties in the formation can contribute to the success of well development strategies such as acid fracture stimulation and enhanced oil recovery techniques (e.g., Water-Alternating-Gas injection).

Rock classification is a common reservoir characterization method that categorizes rock groups with similar rock properties. This technique can be employed to improve the assessment of petrophysical and compositional properties in complex formations (Lucia 1995; Jennings and Lucia 2003; Lucia 2007). However, a reliable rock classification in carbonate formations should incorporate the impact of both depositional attributes and diagenetic modifications on rock properties (Skalinski and Kenter 2014). Purely descriptive classification schemes such as Dunham (1962) and modifications by Embry and Klovan (1971), as well as generic pore typing methods (Choquette and Pray 1970; Lucia 1995 and 2007; Ahr 2008), do not include diagenetic overprint corresponding to fluid flow in carbonate rocks. Petrophysical partitioning techniques such as Leverett's *J*-function (Leverett 1941) and *FZI* method (Amaefule et al. 1993) classify rock types by artificial binning the permeability and the porosity core measurements. Winland's *R35* identifies rock classes based on the major pore system attribute derived from saturation-dependent Mercury Injection Capillary Pressure

(MICP) measurements (Pittman 1992). These techniques are closely related to the dynamic petrophysical properties rooted in diagenesis, but they do not take into account the depositional features of carbonate rocks (Leverett 1941; Pittman 1992; Amaefule et al. 1993). Archie's rock classification (Archie 1952) only qualitatively takes into account both texture and pore types. Furthermore, aforementioned conventional core-based rock classification methods are highly dependent on core measurements, while an extensive core database might not be available for most wells. In the absence of an extensive core database, the conventional rock classification techniques in carbonate formations might not be capable of capturing the heterogeneity in these complex formations.

On the other hand, well logs can provide real-time information about petrophysical, compositional, and elastic properties with a relatively high vertical resolution. Serra and Abbott (1980) applied well logs to conduct rock classification based on distinct log responses that were defined as electrofacies. Analytical well-log-based rock quality factors are other alternatives for petrophysical rock classification. Previous publications showed the application of these analytical methods in siliciclastic formations (Gandhi et al. 2010; Heidari et al. 2011). These factors qualitatively include the dynamic petrophysical properties for reliable rock classification.

Furthermore, a reliable assessment of elastic properties and rock classification based on these rock properties can provide insight into the formation fracturing potential. High Young's modulus can indicate formation capability to overcome the closure stress effectively and promise continuous fracture conductivity (Deng et al. 2012). Therefore, formation intervals with optimum elastic properties can guarantee fracture endurance throughout the well production life. However, selection of the fracture candidate zones can be challenging in carbonate formations, because of the heterogeneous distribution of petrophysical properties, mineralogy, and elastic properties. Common rock classification techniques that incorporate formation elasticity are based on real-time compressional and shear-wave slowness measurements (Leslie and Mons 1982). However, the shear-wave slowness measurements are not always available. Effective medium theories, on the other hand, can be used to assess elastic properties, in the absence of shear-wave slowness measurements, by incorporating elasticity, shapes, and concentrations of rock constituents (i.e., pores and grains) (Berryman 1995; Brie et al. 1985).

Pore shape is among the rock properties that affect both formation elasticity and electrical conductivity of the formation (Berryman 1995; Wang 2001; Brie et al. 1985; Zhan et al. 2012). The electrical conductivity of different pore types in the formation can be incorporated in the effective medium theories for the assessment of porosity (Kazatchenko et al. 2004). Application of different effective medium theories such as the Self-Consistent Approximation (SCA) and the Differential Effective Medium (DEM) theories in carbonate formations has been previously investigated (Kazatchenko et al. 2004; Markov et al. 2005; Kumar and Han 2005; Gomez et al. 2009). Kazatchenko et al. (2004) applied the conductive and the elastic SCA theories for the assessment of porosity and elastic moduli of carbonate core samples. Markov et al. (2005) and Kumar and Han (2005) used the DEM method to model elastic moduli in carbonate core samples. Gomez et al. (2009) showed that DEM may estimate the elastic moduli accurately, but it is not reliable for modeling the electrical conductivity. On the other hand, they showed that the SCA is a robust approach for the joint modeling of electrical conductivity and elastic properties in carbonate rocks (Gomez et al. 2009). Thus, the conductive and the elastic SCA theories can be used to estimate concentrations of different pore types and elastic moduli in carbonate formations, by incorporating the impact of shapes of different pore types and minerals on electrical conductivity measurements and formation elasticity, respectively.

1.2 Statement of Problem

The conductivity of an acid fracture is dependent on the rate and the homogeneity of dissolution of carbonate rocks in the acid. Heterogeneous distribution of petrophysical properties and mineralogy can result in non-uniform dissolution of the rock, creating acid etching on fracture faces that maintain fracture conductivity under closure stress. Characterization of small-scale distribution of petrophysical properties, mineralogy, and elastic properties, can improve prediction of acid fracture conductivity and can optimize completion design.

Core/outcrop measurements of petrophysical properties (i.e., permeability) are commonly used to assess formation heterogeneity (Oeth et al. 2011; Goggin et al. 1992; Kittridge et al. 1990). However, core data might be inadequate for characterizing formation heterogeneity, and measurements of petrophysical properties obtained from outcrops might not be representative of the true reservoir conditions. Diagenetic processes that carbonate rocks undergo at reservoir conditions can result in complex pore structure and heterogeneous distribution of minerals, which cannot be identified from outcrops. As an alternative to core/outcrop measurements, well logs can be used to assess petrophysical properties and mineralogy at all depths along the wellbore. Nevertheless, assessment of petrophysical properties based on well logs can be challenging in complex carbonate formations, as the result of the rapid vertical and lateral variation of these rock properties in the formation. Rock classification can be used to improve assessment of petrophysical and compositional properties based on well logs in carbonate formations.

Moreover, rock classification can contribute to better understanding the impact of formation heterogeneity on fluid injection problems during enhanced oil recovery. Water-Alternating-Gas (WAG) injection which is composed of alternating flow of water and gas reduces the high mobility of gas, preventing early breakthrough that can result in poor sweep efficiency. However, loss of injectivity during WAG cycles has been a major limiting factor in many WAG projects. Heterogeneous distribution of petrophysical properties (i.e., permeability) can impact the injectivity during WAG injections. The effective fluid mobility is reduced not only in the layer with higher permeability, but also in the adjacent layers with lower permeability. Thus, a larger fraction of gas flows into the layers of higher porosity and permeability, compared to layers with poor petrophysical properties. This results in reduced injectivity and a lower oil recovery (Rogers and Grigg 2001).

In this dissertation, I propose an integrated rock classification workflow based on conventional well logs and core data to characterize formation heterogeneity and to improve the assessment of petrophysical and compositional properties in carbonate formations. The application of conventional well logs is emphasized in this dissertation, as the advanced logging tools (e.g., Nuclear magnetic resonance and Formation Micro-Imager) are not available in all wells. Furthermore, a contribution of the proposed rock classification workflow, compared to the conventional rock classification techniques in carbonates, is the integration of depositional and diagenetic attributes. The rock classification workflow takes into account the impact of both depositional and diagenetic attributes in rock classification by considering the effect of the shapes of different pore types and minerals in each geological facies on formation resistivity and elasticity. The workflow also uses the visible trend of mud filtrate invasion on resistivity well logs with different volumes of investigation to qualitatively account for the dynamic petrophysical properties, rooted in diagenesis.

Furthermore, I conduct pore typing based on pore-size distribution functions derived from MICP measurements and populate pore types in core and well-log scales. I investigate the impact of pore systems on electrical resistivity measurements by evaluating the conformity of resistivity measurements and identified pore types.

Additionally, incorporation of elastic properties in rock classification can assist in determining the fracture locations for an enhanced acid fracture design. I estimate elastic properties from well logs, in the absence of a shear-wave slowness log, by incorporating shapes, elasticity, and volumetric concentrations of different rock constituents. Finally, I take advantage of learning algorithms to distinguish the well log signatures, corresponding to mineralogy, elastic, and static and dynamic petrophysical properties, for rock classification.

1.3 Research Objectives

This dissertation focuses on integration of geological attributes, obtained from core data, and petrophysical properties, mineralogy, and elastic properties, estimated from conventional well logs, for rock classification in complex carbonate formations. The main objective is to develop an integrated rock classification scheme in carbonate formations to improve characterization of spatial heterogeneity. The introduced rock classification scheme has broad well development applications such as predicting acid fracture conductivity and quantifying the impact of formation heterogeneity on fluid injectivity loss during enhanced oil recovery (i.e., Water-Alternating-Gas injection). The following list summarizes the detailed objectives pursued by this research:

i. Create ties between geological attributes and petrophysical properties.
ii. Apply analytical techniques to estimate the volumetric concentrations of different pore types in the formation by incorporating the impact of pore shapes on resistivity well log.
iii. Apply analytical techniques for depth-by-depth assessment of elastic moduli from conventional well logs, where a shear-wave slowness log is not available.

iv. Derive pore-size distribution functions from MICP measurements to characterize complex pore systems.

v. Apply visible trends of mud-filtrate invasion on resistivity well logs, to qualitatively characterize distribution of dynamic petrophysical properties in the formation.

vi. Introduce rock classification techniques based on conventional well logs, with minimal dependency on core measurement. These techniques can be applied where core data are not available.

vii. Conduct permeability assessment by applying a core-based porosity permeability correlation in each rock class. Estimates of permeability are then used for variogram analysis and determination of the correlation length, which is an input to the acid fracture conductivity model.

viii. Investigate the application of well logs and well-log-based estimates of petrophysical properties and mineralogy for variogram analysis. The correlation length is determined in each case and compared against the correlation length determined from variograms of well-log-based estimates of permeability.

ix. Introduce a coefficient of spatial heterogeneity to characterize the spatial variation of petrophysical rock classes and lithofacies.

x. Apply rock classification and coefficient of spatial heterogeneity introduced in (10) to investigate and quantify the impact of formation heterogeneity on fluid injectivity abnormalities experienced during Water-Alternating-Gas enhanced oil recovery.

1.4 Method Overview

Fig. 1.1 shows the proposed workflow for an integrated rock classification in carbonate formations. The proposed rock classification workflow is adaptable to different data scenarios driven by the availability of (a) slabbed cores, thin-section images, and Scanning Electron Microscope (SEM) images for characterizing geological attributes and geometries of rock components, (b) visible well-log signatures, related to dynamic petrophysical properties (e.g. separation of resistivity logs, as the result of mud-filtrate invasion into the formation), (c) core data (e.g., permeability and porosity measurement), (d) dynamic petrophysical data (e.g., relative permeability curves and MICP measurements), and (e) 3D micro-CT scan images.

The proposed rock classification scheme incorporates geological (i.e., depositional and diagenetic) attributes, static and dynamic petrophysical properties, mineralogy, and elastic properties. Geological facies are defined based on the diagenetic and depositional attributes, where thin-section images, SEM images, and slabbed cores are available. Furthermore, shapes of different rock components in each geological facies are determined from an analysis on thin-section images, SEM images, and slabbed cores for the assessment of elastic properties and porosity (i.e., interparticle and intraparticle porosity).

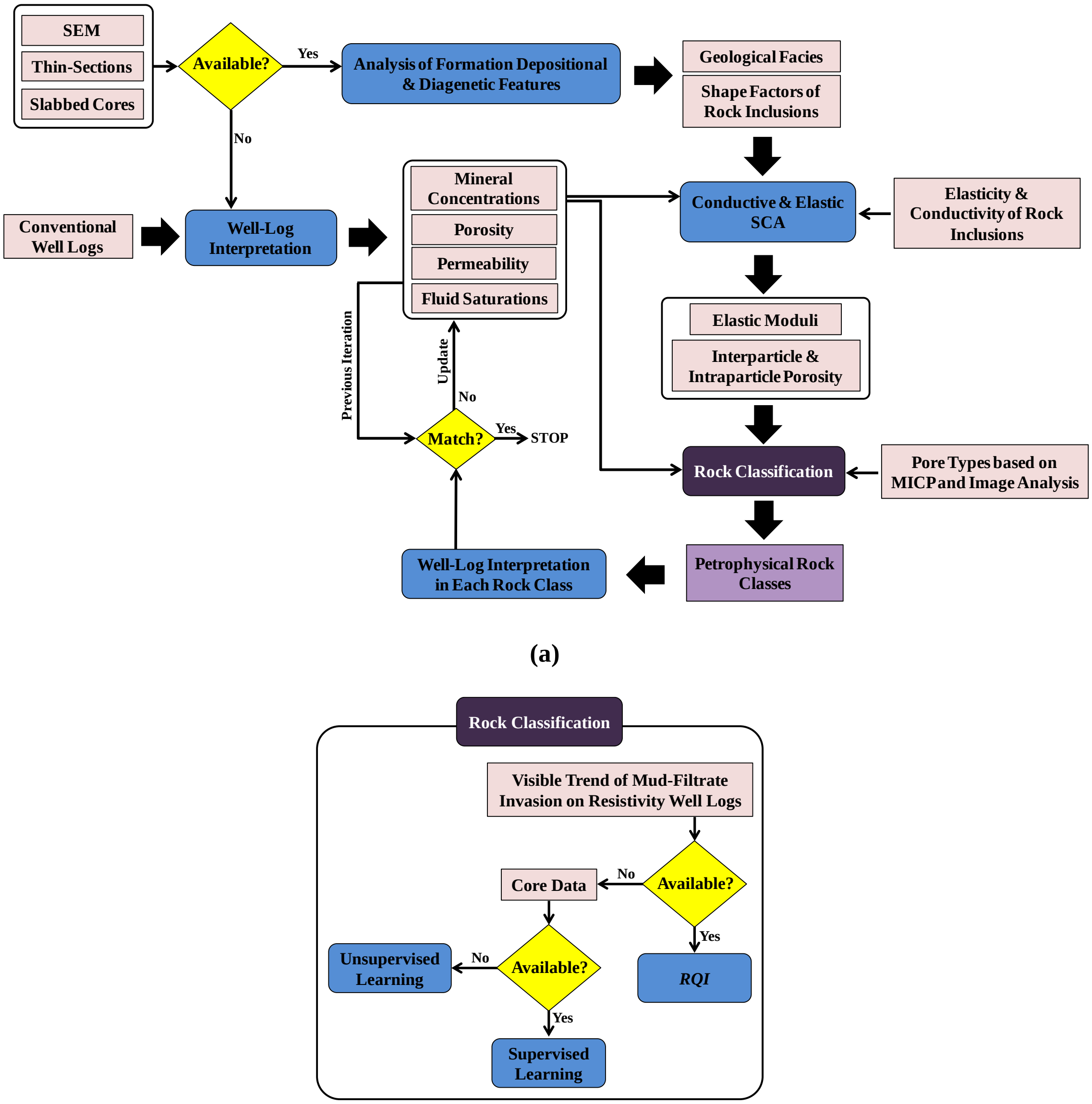

(a)

(b)

Fig. 1.1—Proposed method: (a) workflow for an integrated rock classification in carbonate formations; (b) selection of the appropriate technique for rock classification based on availability of input data.

Multi-mineral analysis of well logs is conducted for preliminary assessment of petrophysical and compositional properties. The conductive and the elastic SCA theories are then applied to estimate depth-by-depth volumetric concentrations of interparticle (i.e., interconnected) and intraparticle pores (e.g., vugs), as well as elastic bulk and shear moduli using well logs in each geological facies in the formation.

Finally, a petrophysical rock classification is conducted based on well-log-derived depth-by-depth estimates of petrophysical properties, mineralogy, and elastic properties. In this step, three different approaches can be implemented based on the availability of data and well-log signatures. For the case, where the trend of mud-filtrate invasion on the resistivity well logs is apparent, a real-time analytical factor (i.e., *RQI*) is introduced to be applied for rock classification. In the case where an extensive core database is available, a supervised learning approach is used for rock classification. This is a rare case, as core data are usually sparse and not sufficient for characterizing the heterogeneity in carbonate formations. Alternatively, unsupervised learning is proposed for rock classification, where core data are inadequate. Furthermore, dynamic petrophysical properties (e.g., MICP measurements) can be incorporated in rock classification to account for pore size distribution in the formation. The results of petrophysical rock classification are used to update the estimates of permeability in each rock class. The updated results serve as inputs to the next iteration of well-log interpretation, the SCA theories, and petrophysical rock classification. The new petrophysical rock classes can be used to update estimates of permeability until a convergence criterion is met.

1.5 Outline of Dissertation

Following the introductory chapter, this dissertation includes six additional chapters. Chapter II introduces an integrated rock classification approach that incorporates estimates of petrophysical, compositional, and elastic properties based on conventional well logs, with depositional and diagenetic attributes interpreted from core. I apply the introduced technique in two wells in the upper Leonardian carbonate interval of the Veterans field, in west Texas.

Chapter III elaborates on pore typing based on attributes of multi-modal Gaussian functions derived from MICP measurements. This chapter also investigates the impact of pore structure on electrical resistivity by assessing the conformity between MICP-based pore types and resistivity measurements. The work described in this chapter is conducted in the SACROC Unit, located in west Texas.

Chapter IV focuses on the use of conventional well logs for characterizing formation heterogeneity, where core data are not adequate. This chapter introduces rock classification techniques based on conventional well logs, with minimal dependency on core data, which can be used for enhanced assessment of permeability. The introduced techniques are applied in two carbonate formations, Happy Spraberry oil field and Hugoton gas field. Furthermore, this chapter investigates the application of well logs and estimates of petrophysical properties and mineralogy, obtained from well logs, for variogram analysis. The outcome of variogram analysis is characterization of formation heterogeneity incorporated for prediction of acid fracture conductivity.

Chapter V investigates and quantifies the impact of formation heterogeneity on loss of injectivity during WAG injection. Rock classification and heterogeneity analysis are conducted in ten wells in the SACROC Unit, located in the west Texas to study this phenomenon.

In addition to rock classification in carbonate formations, which is the main focus in this dissertation, I introduce similar rock classification techniques in organic-rich shale formations. Chapter VI describes the introduced rock classification techniques and their application in the Haynesville Shale.

Finally, Chapter VII summarizes the concluding remarks of the research stemming from this dissertation and recommendations for future research.

CHAPTER II

INTEGRATED ROCK CLASSIFICATION IN CARBONATE FORMATIONS BASED ON ELASTIC AND PETROPHYSICAL PROPERTIES ESTIMATED FROM CONVENTIONAL WELL LOGS*

A reliable rock classification in a carbonate reservoir should take into account petrophysical, compositional, and elastic properties of the formation. However, depth-by-depth assessment of these properties is challenging, as a result of the complex pore geometries and significant heterogeneity caused by diagenesis. Common rock classification methods of carbonate formations do not incorporate the impact of both depositional and diagenetic modifications on rock properties. Furthermore, elastic properties, which control fracture propagation and the conductivity of fractures under closure stress, often are not accounted for in conventional rock classification techniques. I apply an integrated rock classification technique, based on both depositional and diagenetic effects that can ultimately enhance (a) assessment of petrophysical properties, (b) selection of candidates for fracture treatment, and (c) production from carbonate reservoirs.

---

*Reprinted with permission from “Integrated Rock Classification in Carbonate Formations Based on Elastic and Petrophysical Properties Estimated from Conventional Well Logs” by Mehrnoosh Saneifar, Roy Conte, Clotilde Chen Valdes, Zoya Heidari, and Michael C. Pope, 2015. *AAPG Bulletin*, Preliminary Ahead of Print version, Copyright 2015 by the AAPG whose permission is required for further use.

I applied the conductive and the elastic Self-Consistent Approximation (SCA) theories to estimate depth-by-depth volumetric concentrations of interparticle (e.g., interconnected pore space) and intraparticle (e.g., vugs) pores, as well as elastic bulk and shear moduli, in the formation. This process incorporated the impact of shape and volumetric concentrations of rock components on electrical conductivity and elastic properties.

I documented a successful application of the technique in two wells in the upper Leonardian carbonate interval of the Veterans field, in west Texas. The identified rock types were verified using thin-section images and core samples.

2.1 Introduction

Assessment of petrophysical, compositional, and elastic properties in carbonate formations is challenging, due to the abrupt vertical variation of pore structure and lithology. Pore shape is among the rock properties that affects formation elasticity and therefore, needs to be incorporated for a reliable assessment of elastic properties (Brie et al. 1985; Wang 2001; Zhan et al. 2012). Pore shape also affects electrical conductivity of the formation (Brie et al. 1985). Effective medium theories were introduced for modeling effective elastic moduli and electrical conductivity of fluid-bearing rocks, which take into account pore/grain shapes as well as volumetric concentrations of individual rock constituents (Brie et al. 1985; Berryman 1995).

Furthermore, a reliable assessment of elastic properties can provide insight into the formation fracturing potential. Poisson’s ratio may represent the fracture initiation possibility, and Young’s modulus may reflect the ability of the rock to maintain a fracture (Rickman et al. 2008). High Young’s modulus in carbonate rocks can resist the closure stress effectively and promise continuous fracture conductivity (Deng et al. 2012). Therefore, formation intervals with optimum elastic properties can guarantee fracture endurance throughout the well production life. However, selection of the best zones for fracturing can be challenging in carbonate formations, because of the heterogeneous distribution of petrophysical, compositional, and elastic properties. A reliable rock classification based on elastic properties, as well as petrophysical properties and mineralogy in the formation, can improve completion design, reservoir characterization, and ultimately production from a complex carbonate formation.

I introduced and applied an integrated rock classification scheme that incorporates petrophysical, compositional, and elastic properties, as well as depositional and diagenetic attributes. The first step in the method was geological facies classification based on both depositional and diagenetic attributes. I utilized the conductive and the elastic SCA theories to estimate depth-by-depth volumetric concentrations of interparticle (i.e., interconnected) and intraparticle (e.g., vugs) pores, as well as elastic bulk and shear moduli using well logs in each geological facies in the formation. Finally, I conducted petrophysical rock classification based on well-log-derived depth-by-depth estimates of petrophysical, compositional, and elastic properties. I applied the introduced technique in two wells in the upper Leonardian carbonate interval of the Veterans field, in west Texas (Saneifar et al. 2015).

The contributions of the introduced rock classification technique compared to the previously introduced methods include (a) application of conventional well logs for the depth-by-depth assessment of elastic moduli and interparticle and intraparticle porosity, where acoustic well logs are not available, (b) incorporation of the elastic properties in carbonate rock classification, and (c) creating ties between geological facies and petrophysical attributes for an integrated rock classification.

2.2 Veterans Oil Field, West Texas: Geological Setting

Veterans oil field is located in the Glasscock County, Texas, on the eastern side of the Midland Basin, near its Eastern Shelf (**Fig. 2.1**). The reservoir is an upper Leonardian succession of detrital carbonate deposited in slope and basinal environments (**Fig. 2.2**). The detrital carbonate units extend from the Eastern Shelf margin into the Midland basin and may represent a combination of debris flows and submarine fan depositional processes (Cook 1983). Hydrocarbon production from this interval in the Veterans Field is highly variable. For instance, Well A produced oil at economic rates following fracture stimulation, whereas, the coeval section in Well B failed to produce oil after similar fracture stimulation (Saneifar et al. 2015).

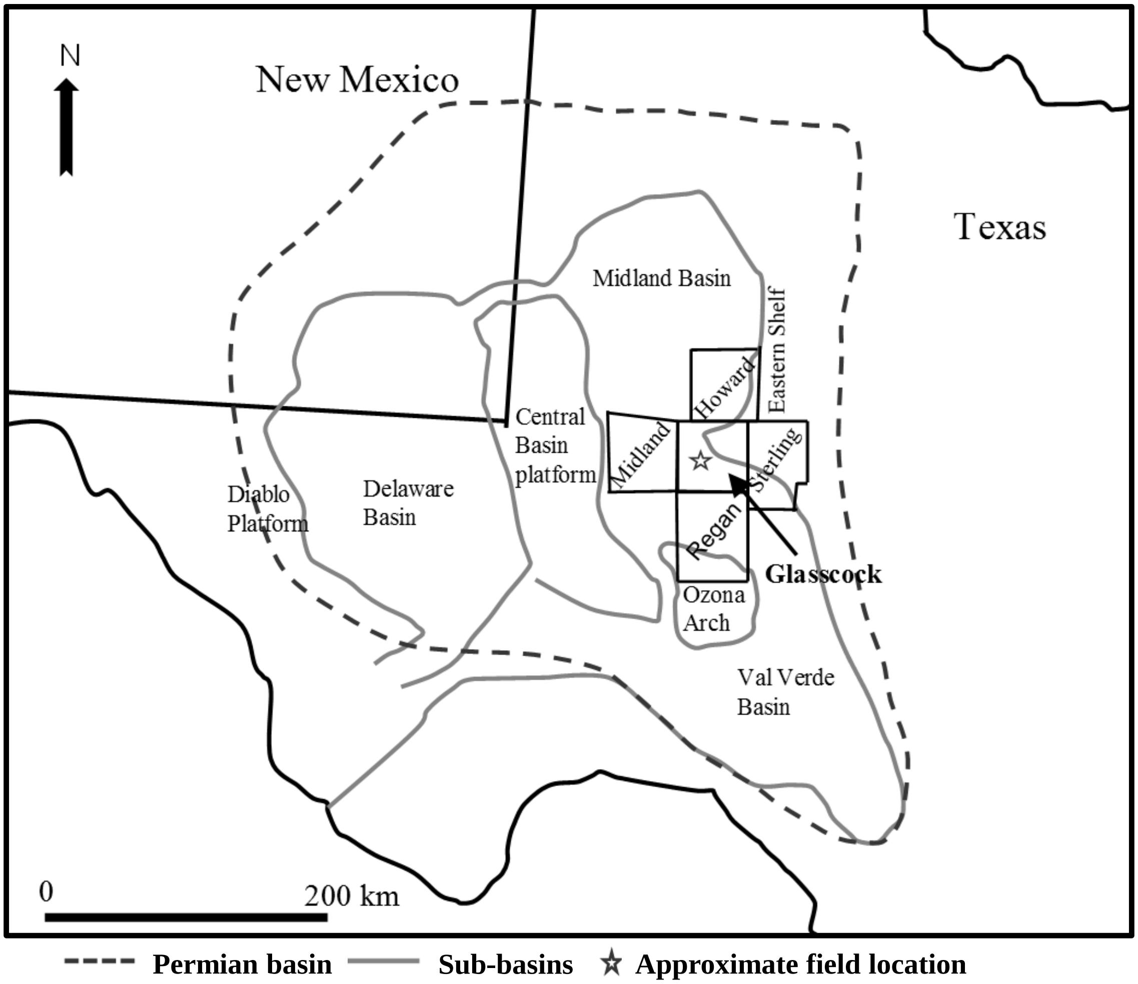

Fig. 2.1—Regional map of the Permian Basin showing Glasscock County and the approximate field location (Saneifar et al. 2015).

The upper Leonardian detrital carbonate succession in the Veterans Field best fits a base-of-slope apron depositional model in which carbonate aprons develop along relatively steep slopes and are fed by several small submarine canyons that by-pass fine-grained upper slope sediments (Schalger and Chermak 1979; Mullins and Cook 1986; Playton et al. 2010; Conte 2014).

<table>
<tr><th>System</th><th>Series</th><th colspan="2">Midland Basin</th><th>Eastern Shelf</th></tr>
<tr><td rowspan="5">Permian</td><td rowspan="5">Leonardian</td><td rowspan="2">Spraberry</td><td rowspan="2">This Study</td><td>Upper Clear Fork</td></tr>
<tr><td>Middle Clear Fork</td></tr>
<tr><td colspan="2">Dean Sandstone</td><td>Tubb Sandstone</td></tr>
<tr><td colspan="2" rowspan="2">Lower Leonard (Carbonates and Shales)</td><td>Lower Clear Fork</td></tr>
<tr><td>Wichita</td></tr>
</table>

(a)

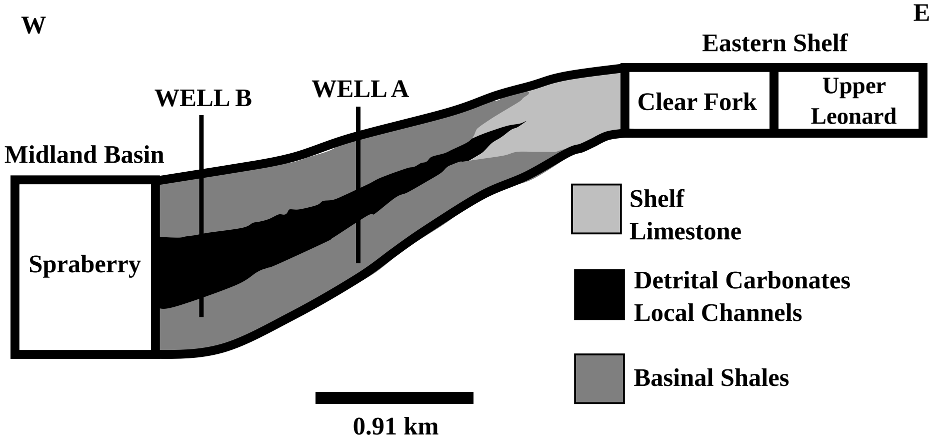

(b)

(After Conte 2014)

Fig. 2.2—Veterans Field Example Stratigraphy: (a) Leonardian stratigraphic chart of the Eastern Shelf and Midland Basin stratigraphy; (b) Upper Leonardian detrital carbonate succession stratigraphy in Veterans Field Glasscock County, Texas. The succession is underlain and overlain by shale (Saneifar et al. 2015).

The following section reviews the common rock classification techniques in carbonate formations and their reliability in capturing heterogeneity in carbonate formations.

2.3 Method

First, geological facies were classified based on the analysis of depositional and diagenetic features, using thin-sections, slabbed cores, and Scanning Electron Microscope (SEM) images (**Fig. 2.3**). Well-log interpretation was the next step for preliminary assessment of porosity (i.e., total and interconnected), permeability, water saturation, and mineral concentrations. The shape factors of rock inclusions, elasticity and conductivity of rock inclusions, and estimates of mineral concentrations from well-log interpretation were applied to assess interparticle and intraparticle porosity, as well as elastic moduli using the conductive and the elastic SCA theories. Petrophysical rock classification was implemented using an unsupervised artificial neural network, with an input of well-log-based estimates of (a) interparticle and intraparticle porosity, (b) elastic moduli of the formation, (c) mineral concentrations, and (d) number of petrophysical rock classes. The results of rock classification were used to update the estimates of permeability and water saturation in each rock class. The updated results were inputs to the next iteration of well-log interpretation, the SCA theories, and petrophysical rock classification. The iteration continued until a convergence criterion for the assessment of permeability and water saturation was met (Saneifar et al. 2015).

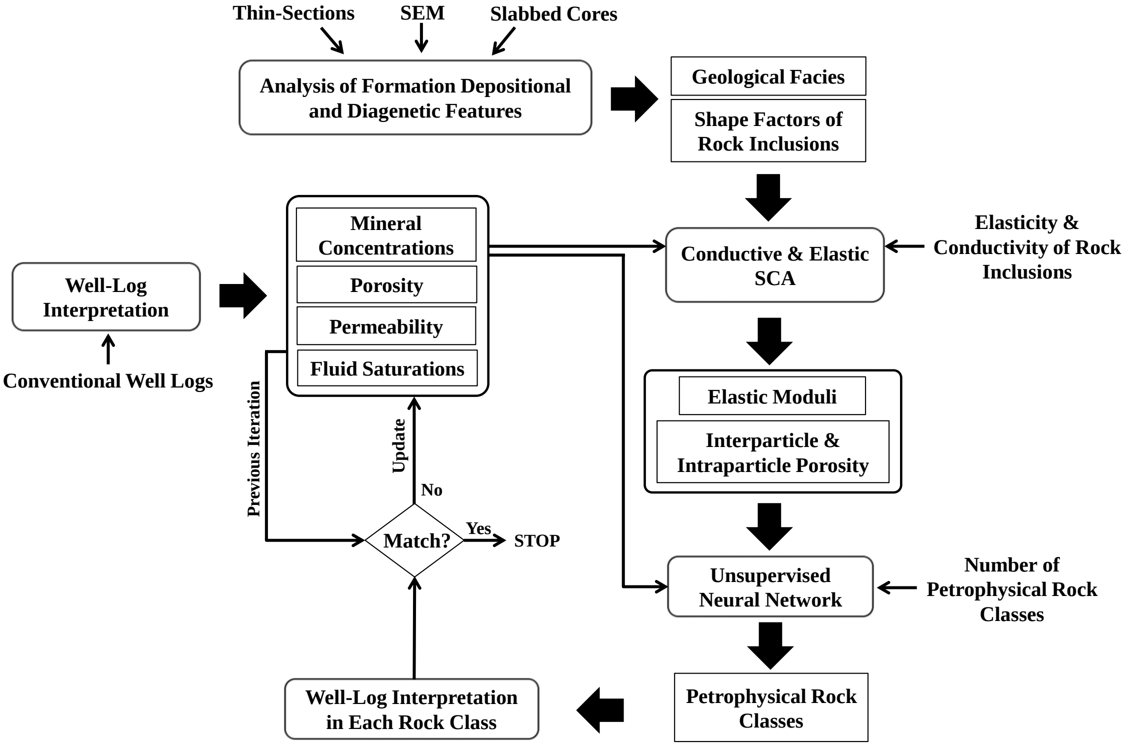

Fig. 2.3—A workflow illustrating the methods, including well-log interpretation, geological facies classification, assessment of elastic moduli and porosity, rock classification, and assessment of permeability and water saturation.

2.3.1 Classification of Geological Facies

Geological facies were defined based on an analysis of the depositional texture (i.e., skeletal grains, detrital component, pore system, and mineralogy) and diagenetic features using slabbed cores, thin-section petrography, and SEM images (Saneifar et al. 2015). Textural classification was conducted based on Dunham’s (1962) classification. Choquette and Pray’s (1970) pore typing scheme was used to classify pore size. Finally, geological facies were determined by incorporating the textural features and diagenetic observations. Digital measurements of pore sizes were based on thin-section images obtained using a petrographic microscope. The petrographic microscope was equipped with a high-resolution digital camera and software to capture the thin-section images and measure the diameter of the pores. The software converted each captured image from pixel scale to micrometer scale before measuring the pore diameter. The thin-section images were impregnated with blue dye to indicate pore spaces, and stained with Alizarin Red S to determine the relative abundance of calcite, quartz, and dolomite. As the thin-section and SEM images represented only a small two-dimensional section of the rock, slabbed cores were used in addition to the thin-section and SEM images to determine the geologic facies.

2.3.2 Initial Well-Log Interpretation

I conducted joint-interpretation of conventional well logs for the preliminary assessment of interconnected and total porosity, water saturation, permeability, and volumetric concentrations of clay and non-clay minerals (Fig. 2.3). The input well logs for multi-mineral analysis included gamma ray (GR), electrical resistivity, density, neutron porosity, Photoelectric Factor (PEF), and compressional-wave slowness. Mud logs, core descriptions, and field reports were used to determine the types of existing minerals. I initially applied Wyllie’s time-average equation (Wyllie et al. 1956) and Archie’s equation (Archie 1942) to estimate interconnected porosity and water saturation. I assumed that Archie’s equation is reliable in the clay-free matrix with interconnected pores (Archie 1942). Archie’s parameters were initially assumed to be 1, 2, and 2 for Archie’s Winsauer factor, *a*, Archie’s porosity exponent, *m*, and Archie’s saturation exponent, *n*, respectively. Preliminary estimates of permeability were obtained by applying core-derived porosity-permeability correlation for the entire depth interval of interest. The results of well-log interpretation, applied models, and Archie’s parameters were updated, after implementing the introduced approach, as described in the following sections.

2.3.3 Depth-by-Depth Assessment of Porosity and Elastic Moduli

I used an effective medium theory, called Self-Consistent Approximation (SCA), for the depth-by-depth assessment of elastic properties and concentration of different pore types (Berryman 1995). Effective medium theories enable analytical modeling of composite materials (e.g., rocks) for their effective properties such as electrical/thermal conductance and elasticity. The conductive and elastic SCA theories assume isotropic conductive and elastic medium of arbitrarily distributed ellipsoidal components with symmetric shapes. Shape factors and concentrations of all constituents are incorporated in the SCA theories. In addition, all components of the composite material are treated equally in the SCA theories, without considering one component as a host. The SCA is known to be an appropriate technique for modeling the electrical conductivity and the elastic properties in complex rocks (Kazatchenko et al. 2004; Gomez et al. 2009).

I applied the conductive and the elastic SCA theories (Berryman 1995) along with interpretation of other borehole geophysical measurements, to estimate depth-by-depth volumetric concentrations of interparticle and intraparticle pores, as well as elastic bulk and shear moduli in the formation.

Conductive SCA theory is given by

$$\sum_{i=1}^{N} x_i(\sigma_i - \sigma_{sc}^{*})R^{*i} = 0\,. \tag{2.1}$$

Elastic SCA model is described via

$$\sum_{i=1}^{N} x_i(K_i - K_{sc}^{*})P^{*i} = 0 \tag{2.2}$$

and

$$\sum_{i=1}^{N} x_i(\mu_i - \mu_{sc}^{*})Q^{*i} = 0\,, \tag{2.3}$$

where N is the total number of rock components, i refers to each rock component, x_i is volumetric concentration of the i-th rock component, σ_i, K_i and μ_i are electrical conductivity and bulk and shear moduli of the rock component i, and σ^{*sc}, K^{*sc}, and μ^{*sc} are the effective electrical conductivity and bulk and shear moduli of the rock, respectively (Berryman 1995). The factors R^{*i}, P^{*i}, and Q^{*i} are functions of the assigned aspect ratio of each rock component, which takes into account the shape of different inclusions in the rock. R^{*i}, P^{*i}, and Q^{*i} are given by

$$R_i^* = \frac{1}{9}\sum_{p=a,b,c}\frac{1}{L_p\sigma_i + (1-L_p)\sigma_{sc}^*}\,, \tag{2.4}$$

$$P_i^* = \frac{1}{3}T_{jjll}^{(i)}\,, \tag{2.5}$$

and

$$Q_i^* = \frac{1}{5}(T_{jljl}^{(i)} - P_i)\,, \tag{2.6}$$

where $T^{(i)}$ is Wu's tensor (Wu 1966) and L_p is the demagnetizing factor along the semi-axes of an ellipsoid. The demagnetizing factor can be obtained using simplified equations provided by Osborn (1945) for prolate and oblate ellipsoids. The assumptions for the aspect ratio of rock inclusions usually involve significant uncertainty. For reliable assessment of the aspect ratios of minerals and different pore types, I conducted an analysis of available thin-section and SEM images. I assumed that aspect ratios of individual inclusions are constant for each geological facies. This approach incorporated the geological attributes in the assessment of petrophysical and elastic rock properties and in the final rock classification.

I applied the conductive SCA theory for the depth-by-depth assessment of porosity by implementing Levenberg–Marquardt algorithm (Levenberg 1944; Marquardt 1963) to minimize the cost function, given by

$$f(x_{inter-por}\, x_{intra-por}) = \left\| \frac{R_{sim.}}{R_{measured}} - 1 \right\|_2^2\,, \tag{2.7}$$

where $x_{inter\text{-}por}$ and $x_{intra\text{-}por}$ are the volumetric concentrations of interparticle and intraparticle pores, respectively. $R_{sim.}$ and $R_{measured}$ are the simulated resistivity (i.e., inverse of conductivity) obtained using Conductive SCA theory and the shallow resistivity measurements, respectively. Aspect ratios of rock inclusions, as well as electrical conductivity of clay minerals, were adjusted in each geological facies, while remaining in a physically viable range (i.e., consistent with core thin-sections and SEM images), to minimize the difference between the modelled and measured resistivity. Estimates of porosity were applied as inputs to the elastic SCA theories for the depth-by-depth assessment of effective bulk and shear moduli. Finally, I estimated Young's modulus, *E*, by (Mavko et al. 2009)

$$E = \frac{9K_{sc}^{*}\mu_{sc}^{*}}{3K_{sc}^{*} + \mu_{sc}^{*}}. \tag{2.8}$$

2.3.4 Petrophysical Rock Classification

I applied an unsupervised artificial neural network to automatically determine different rock classes (Fig. 2.3). The inputs to the unsupervised artificial neural network included well-log-based estimates of petrophysical, compositional, and elastic properties, as well as the number of rock classes. The artificial neural network applies a Self-Organizing Map (SOM), also known as Kohonen map, to index different input parameters by fuzzy clustering (Kohonen 2001). The unsupervised network agglomerates clusters of input data by minimizing the intra-class variance and takes iterative steps to organize similar input data and to assign them to particular nodes on the

SOM map. Unlike the supervised artificial neural network, the unsupervised artificial neural network does not require training with pre-determined rock classes (Gottlib-Zehf 2000).

2.3.5 Iterative Assessment of Petrophysical Properties and Rock Classification

After petrophysical rock classification, I applied the improved estimates of interconnected porosity to assess permeability and water saturation in each rock class. I assumed that the interconnected porosity is equal to the effective porosity that contributes to the fluid flow. I applied core-based porosity-permeability correlations in each rock class for permeability assessment. I identified the Archie's porosity exponent, m, in each rock class based on core measurements of water saturation and interconnected porosity. Water saturation was estimated using Archie's equation, assuming that this relationship is reliable in clay-free carbonate formations with interconnected pore space. The updated porosity, permeability, and water saturation were used to enhance the outcomes of well-log interpretation and final rock classification (Fig. 2.3).

2.4 Results

I applied the introduced rock classification scheme to two wells in the Veterans oil field, WELL A and WELL B. WELL A produced at a high rate after a successful acid fracture stimulation, whereas WELL B experienced negligible production. In the following sections, I explain the possible reason for the failure in WELL B.

2.4.1 Facies Classification

Slabbed cores, thin-sections, and SEM images were analyzed for both wells in the Veterans oil field (Saneifar et al. 2015). WELL A is located close to the Eastern Shelf and WELL B is located deeper in the basin (Fig. 2.2). This analysis showed two main types of pore systems: (a) intraparticle pores that occur as isolated intrafossil pores, mostly in fusulinid grains and (b) interparticle pores that include interconnected pores between grains (Saneifar et al. 2015). Both pore systems were classified into two pore-size classes, micropores and mesopores, based on Choquette and Pray’s (1970) classification. Pores with pore-size diameter smaller than 62.5 µm were classified as micropores and pores having pore-size diameter of 62.5-4000 µm were identified as mesopores. Finally, the facies in the upper Leonardian succession were identified based on the depositional texture (i.e., skeletal grains, detrital component, pore system, and mineralogy) and diagenetic features. The facies include (a) facies 1: clast-supported polymict conglomerate, (b) facies 2: fusulinid wackestone, (c) facies 3: skeletal wackestone, (d) facies 4: fusulinid-crinoid packstone, and (e) facies 5: partially silicified skeletal wackestone (Saneifar et al. 2015). Calcite and dolomite are the main components in the succession with varying concentrations of silt and secondary quartz (chalcedony).

The clast-supported polymict conglomerate consists of clasts of skeletal wackestone to packstone, mudstone, and reef boundstone. This facies is characterized by solution-enhanced interparticle pores and intraparticle pores in skeletal grains in the clasts. The pore sizes vary from micropores to mesopores (< 2000 µm diameter). Poorly developed blocky fringing calcite cement, blocky calcite and dolomite rhombs commonly occur in the intraparticle pores, whereas blocky calcite and saddle dolomite commonly occur in the interparticle pores (**Fig. 2.4**).

The fusulinid wackestone is composed of fusulinid grains, brachiopod shell fragments, bryozoans, and crinoid fragments (**Fig. 2.5**). The matrix also contains a small concentration of silt-sized quartz grains. The intraparticle pore system is characterized by cement-reduced (blocky fringing calcite, blocky calcite, and saddle dolomite) intrafossil pores in the fusulinids, whereas the interparticle pore system is characterized by solution-enhanced intergranular pores. Dissolution of both matrix and skeletal grains occasionally results in channel pore spaces. Pore sizes range from micropores to mesopores (< 4000 µm diameter). Blocky calcite and lower concentration of saddle dolomite occur as pore-filling cements in both the intraparticle and interparticle pore spaces. A small amount of silica replacement also is common in the skeletal grains.

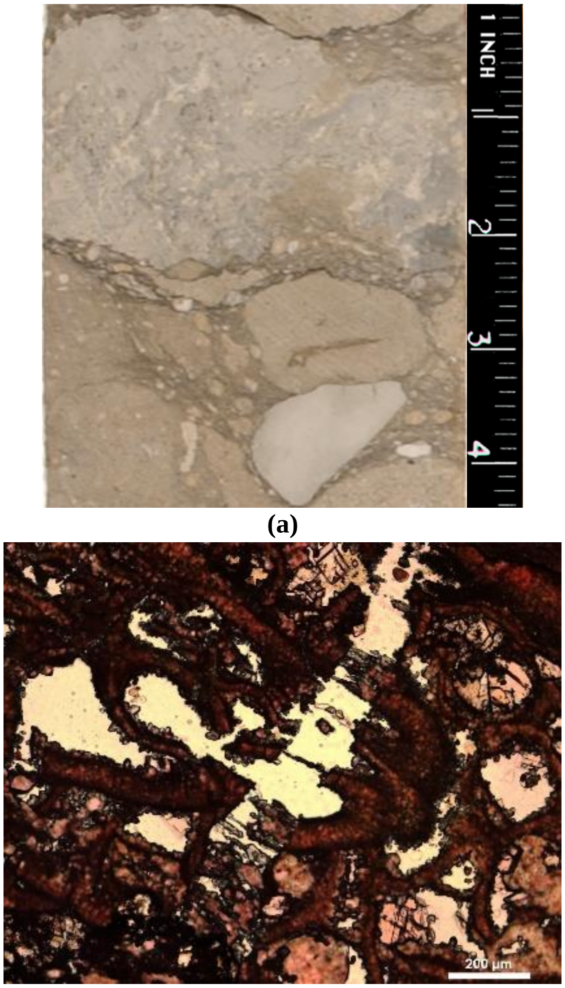

(a)

(b)

Fig. 2.4—Veterans Field Example: slabbed core and thin-section images of facies 1, clast-supported polymict conglomerate. (a) Slabbed core image shows skeletal wackestone to packstone, reef boundstone, and mudstone clasts; (b) The photomicrograph shows intraparticle pores, fusulinid grains, and dissolution (white represents open pores).

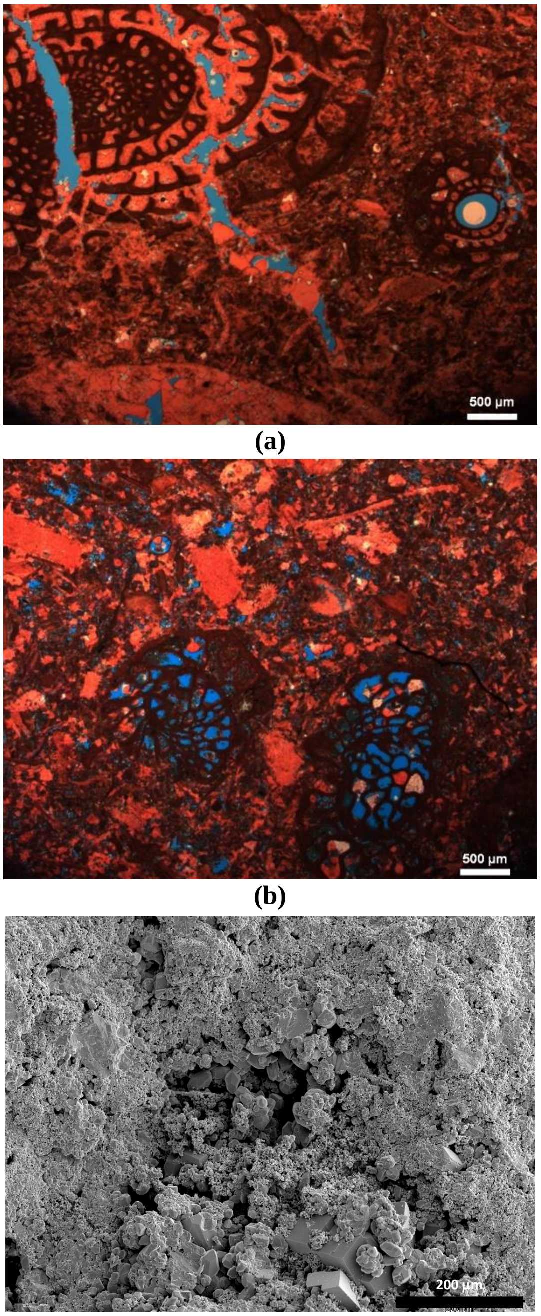

(c)

Fig. 2.5—Veterans Field Example: pore-scale images of facies 2, fusulinid wackestone, including (a) Photomicrograph showing secondary dissolution and cement reduced intraparticle pores (blue) in fusulinids, (b) Photomicrograph showing solution-enhanced intergranular pores (blue represents open pores), and (c) SEM image showing solution-enhanced interparticle pore space.

The skeletal wackestone consists of brachiopod shell fragments, crinoid fragments, occasional peloidal grains, and rare fusulinids with low concentrations of silt-sized quartz grains in the matrix (**Fig. 2.6**). This unit has interparticle pore spaces that are characterized by solution-enhanced intergranular pores. Blocky calcite and a low concentration of secondary dolomite occur as pore-filling cements. Silica replacement of skeletal grains is common. The pores range in size from micropores to mesopores that are less than 250 µm diameter, depending on the degree of dissolution.

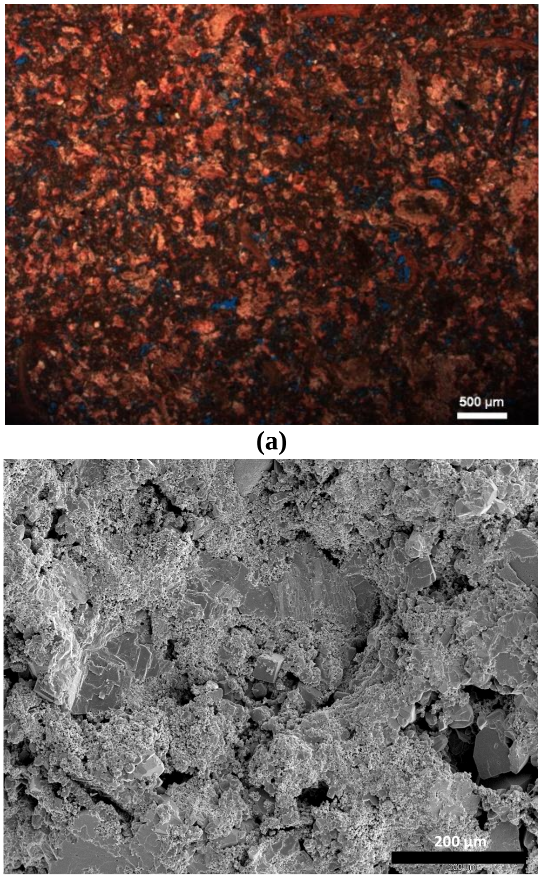

(a)

(b)

Fig. 2.6—Veterans Field Example: pore-scale images of facies 3, skeletal wackestone, including (a) Photomicrograph showing interparticle porosity enhancement by dissolution (blue represents open pores) and (b) SEM image showing porosity enhancement by dissolution, resulting in enlarged irregular pores.

The fusulinid-crinoid packstone facies consists primarily of fusulinid grains and crinoid fragments. It is characterized by intraparticle pores (< 1000 μm diameter) in fusulinid grains and interparticle pores, enhanced by partial dissolution of grains. Fusulinid pores commonly have small amount of calcite blocky fringing cement and dolomite, whereas calcite syntaxial overgrowth occurs in crinoid fragments (**Fig. 2.7**).

The partially silicified skeletal wackestone consists of brachiopod shell fragments, crinoid fragments, sponge spicules, and sparse fusulinids. A small concentration of silt-size quartz grains also occurs in the matrix. The facies occurs as a subfacies in the fusulinid wackestone. It is characterized by dissolution and partial to complete silicification of both grains and matrix. In the silicified part, the skeletal grains are replaced by secondary quartz (chalcedony), whereas the matrix is partially to completely dissolved. The pore system in this facies is complex and highly heterogeneous. The silicified part of the rock has high interparticle porosity ranging from micropores to mesopores (< 1000 μm diameter), whereas the unsilicified rock has low porosity (**Fig. 2.8**). However, the silicified section seems to be isolated from the rest of the pore network, resulting in an overall poor interconnected porosity (Saneifar et al. 2015).

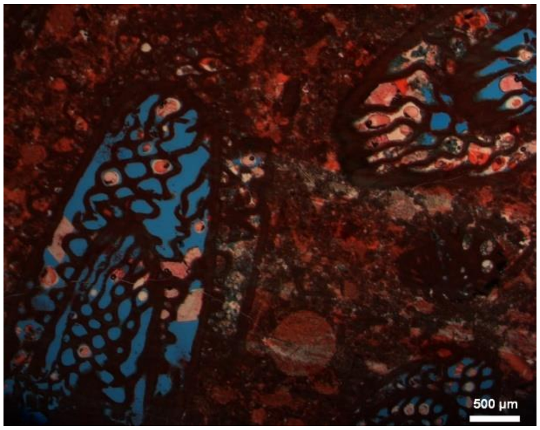

Fig. 2.7—Veterans Field Example: photomicrograph of facies 4, fusulinid-crinoid packstone. The Photomicrograph shows intraparticle pores in fusulinids, with dolomite (gray-white) filling the pore space (blue represents open pores).

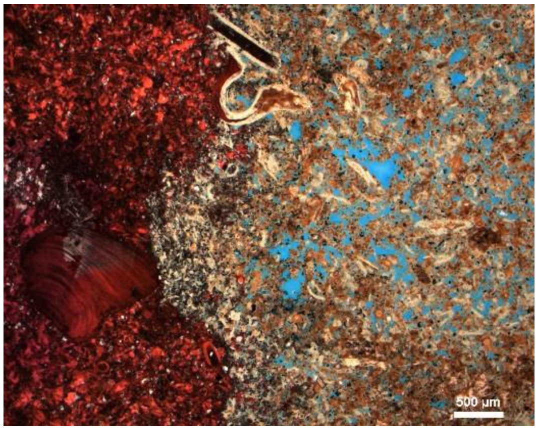

Fig. 2.8—Veterans Field Example: photomicrograph of facies 5, partially silicified skeletal wackestone. Silicified part of the rock (off-white/beige) shows intense secondary dissolution and interconnected pores (blue represents open pores), whereas the unsilicified part does not have significant porosity.

The diagenetic history in each of the facies appears to be relatively uniform. All five facies were compacted in the burial environment. The matrix in these facies is a mixture of mud and crushed skeletal grains, whereas most of the larger skeletal grains are either deformed or broken. Calcite is the most abundant cement occurring as poorly- to well-developed fringes in the intraparticle pores, syntaxial overgrowth in crinoids, and subhedral to anhedral blocky calcite in both intraparticle and interparticle pores. Saddle dolomite occurs in both the intraparticle and interparticle pores. Silica replacement in grains also is common (Saneifar et al. 2015). **Table 2.1** summarizes the pore types within the geological facies.

Facies	Pore Type
Clast-Supported Polymict Conglomerate	Solution-enhanced interparticle and intraparticle pores in skeletal grains in clasts (micropores and mesopores < 2000 µm diameter)
Fusulinid wackestone	Intraparticle and solution-enhanced interparticle pores (micropores and mesopores < 3000 µm diameter)
Skeletal Wackestone	Solution-enhanced interparticle pores, controlled by the intensity of dissolution (micropores and mesopores < 250 µm diameter)
Fusulinid-Crinoid Packstone	Intraparticle pores in fusulinid (mesopores < 1000 µm diameter) and interparticle pores enhanced by partial grain dissolution
Partially Silicified Skeletal Wackestone	Interparticle and intraparticle pores controlled by dissolution and silicification (micropores and mesopores < 1000 µm diameter)

Table 2.1—Veterans Field Example: pore types within the geological facies.

The clast-supported polymict conglomerate and the fusulinid wackestone have the best reservoir quality because both the intraparticle and interparticle pores are enhanced by solution enlargement. The skeletal wackestone also has good reservoir quality, as the interparticle pores also are enhanced by solution enlargement (Saneifar et al. 2015). **Fig. 2.9** (Track 12) and **Fig. 2.10** (Track 12) show geological facies classification, based on the facies identified from thin-section images, slabbed core samples, and SEM images, in WELL A and WELL B, respectively.

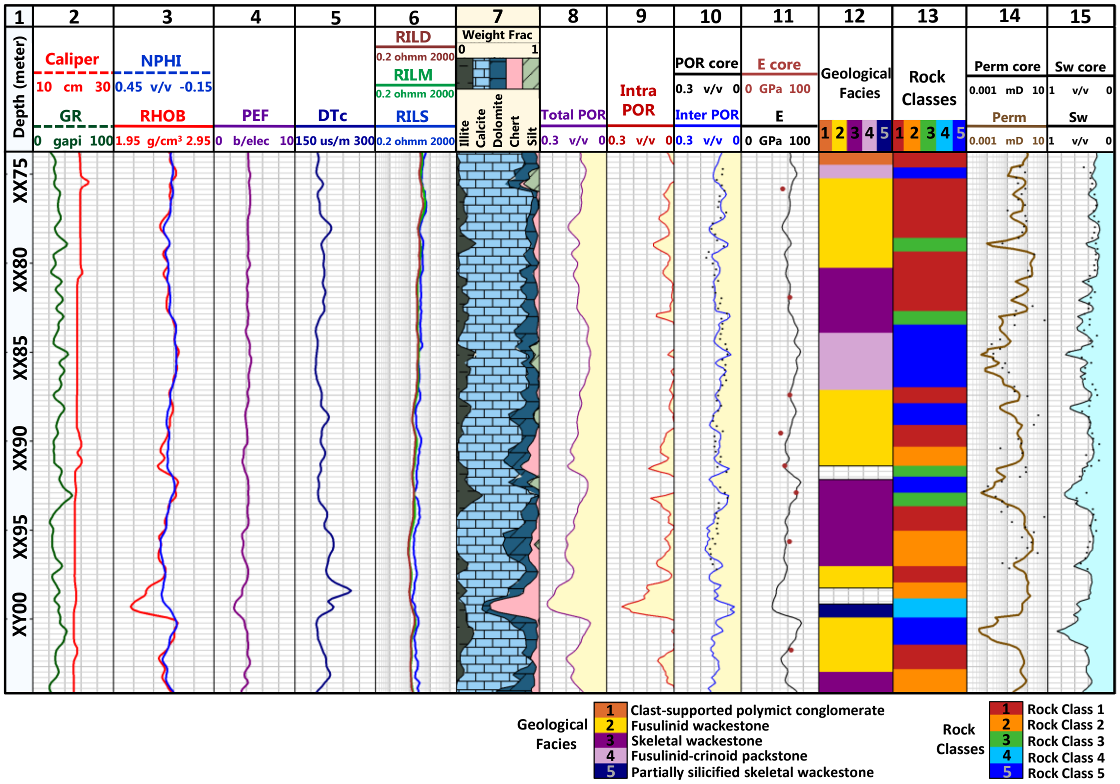

Fig. 2.9—Veterans Field Example–WELL A: conventional well logs and the estimates of petrophysical and compositional properties. Tracks from left to right include, Track 1: depth; Tracks 2-5: GR, caliper, neutron porosity (in water-filled limestone units), bulk density, PEF, compressional wave-slowness; Track 6: shallow, medium, and deep resistivity logs; Track 7: estimates of volumetric concentrations of dolomite, calcite, chert, silt, and illite; Track 8: estimates of total porosity; Track 9: estimates of intraparticle porosity; Track 10: estimates of interparticle porosity, compared to core measurements; Track 11: estimates of Young's modulus, compared to core measurements; Track 12: geological facies classification; Track 13: petrophysical rock classification; Track 14: estimates of permeability, compared to core measurements; Track 15: estimates of water saturation, compared to core measurements.

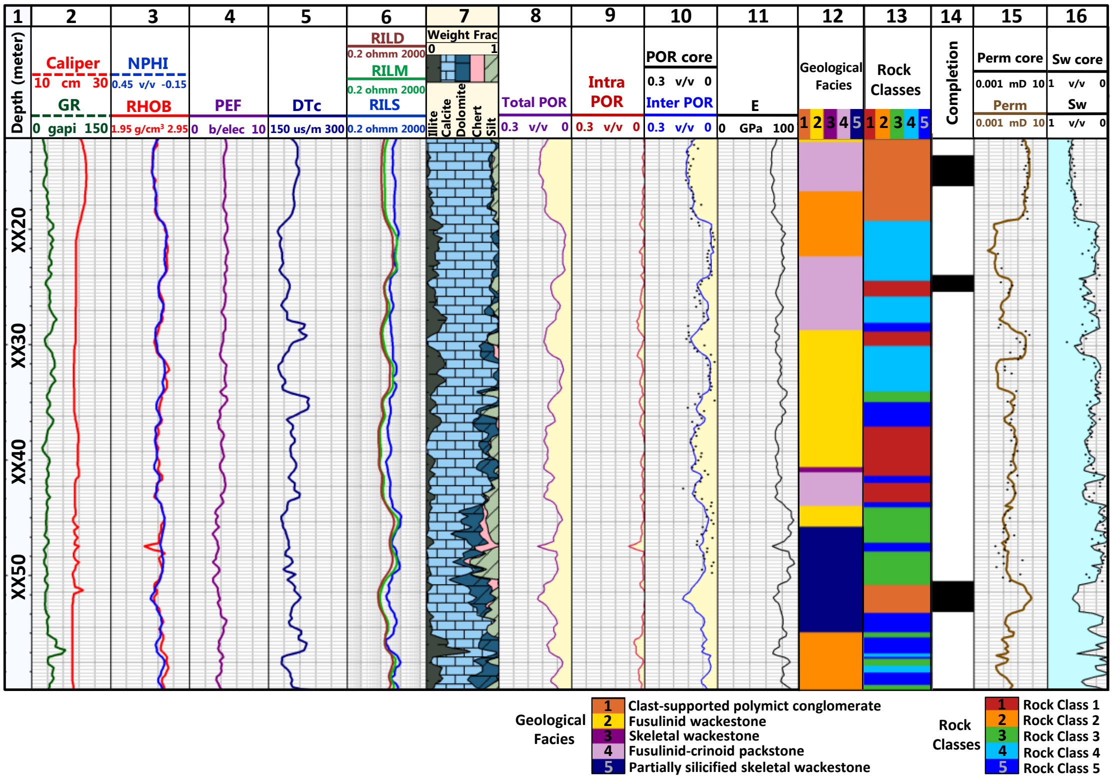

Fig. 2.10—Veterans Field Example–WELL B: conventional well logs and the estimates of petrophysical and compositional properties. Tracks from left to right include, Track 1: depth; Tracks 2-5: GR, caliper, neutron porosity (in water-filled limestone units), bulk density, PEF, compressional wave-slowness; Track 6: shallow, medium, and deep resistivity logs; Track 7: estimates of volumetric concentrations of dolomite, calcite, chert, silt, and illite; Track 8: estimates of total porosity; Track 9: estimates of intraparticle porosity; Track 10: estimates of interparticle porosity, compared to core measurements; Track 11: estimates of Young's modulus, compared to core measurements; Track 12: geological facies classification; Track 13: petrophysical rock classification; Track 14: completed depth intervals with fracture treatment, marked in black; Track 15: estimates of permeability, compared to core measurements; Track 16: estimates of water saturation, compared to core measurements.

2.4.2 Assessment of Petrophysical, Compositional, and Elastic Properties

I conducted joint-inversion of conventional well logs for WELL A and WELL B in the Veterans oil field to estimate total porosity and volumetric concentrations of minerals. The well logs available included GR, shallow, medium, and deep array induction electrical resistivity, bulk density, neutron porosity, PEF, and compressional-wave slowness.

The dominant clay type in this formation is illite. The non-clay matrix components in this formation are calcite, dolomite, silt, and chalcedony. Formation fluids include saline formation water and oil. The drilling mud is fresh water-based mud. **Tables 2.2** and **2.3** list the parameters assumed in the well-log interpretations of WELL A and WELL B.

Parameters	**Value**	**Unit**
Formation water resistivity @ 98 °F	0.04	ohmm
Formation water salt concentration	170,000	ppm
Mud-filtrate resistivity @ 98 °F	0.86	ohmm
Mud-filtrate salt concentration	51,470	ppm
Shale porosity	0.15	-

Table 2.2—Veterans Field Example– WELL A: input parameters for well-log interpretation.

Parameters	**Value**	**Unit**
Formation water resistivity @ 105 °F	0.03	ohmm
Formation water salt concentration	220,000	ppm
Mud-filtrate resistivity @ 105 °F	0.84	ohmm
Mud-filtrate salt concentration	4700	ppm
Shale porosity	0.15	-

Table 2.3—Veterans Field Example– WELL B: input parameters for well-log interpretation**.**

After initial well-log interpretation, I estimated porosity (i.e., interparticle and intraparticle) and elastic moduli using the conductive and the elastic SCA theories. The inputs to these processes included the depth-by-depth estimates of total porosity and volumetric concentrations of minerals from initial interpretation of well logs, as well as aspect ratios of different rock components. I categorized the pore network into interparticle and intraparticle porosity. From an analysis of the thin-section and the SEM images, I assumed that the interparticle pores are predominantly interconnected and the intraparticle pores are isolated vugs. The conductive SCA theory was applied to estimate the interparticle and intraparticle porosity using shallow resistivity measurements, with the assumption that the interconnected pores are fully saturated by drilling mud-filtrate in the near-wellbore region, and isolated pores are saturated by formation water at reservoir conditions. Clay minerals were assumed to be conductive due to the presence of clay-bound water. A prolate ellipsoidal model was used to determine Wu's tensor (Wu, 1966) and demagnetizing factors. I assumed interparticle porosity to have a small aspect ratio (≤ 0.1), characterized intraparticle porosity by stiff near-spherical shape using an aspect ratio of 0.3-0.5, and considered an elongated ellipsoidal shape with an aspect ratio of 0.01-0.05 for clay minerals. Non-clay matrix components are assumed to be near-spherical, with an aspect ratio of 0.5.

I obtained the depth-by-depth estimates of interparticle and intraparticle porosity by minimizing the difference between the modeled resistivity and the apparent shallow resistivity well log. Estimates of interparticle and intraparticle porosity were assumed to sum up to the total porosity (i.e., initially estimated using conventional well-log interpretation). The estimates of interparticle and intraparticle porosity were applied in the elastic SCA theory for the assessment of elastic moduli. The assumed elastic moduli of individual rock components are listed in **Table 2.4**.

Rock Component	**K_i (GPa)**	**μ_i (GPa)**
Calcite	76.80	32.00
Dolomite	94.90	45.00
Chert	37.00	44.00
Silt	37.00	44.00
Illite	52.30	31.70
Water	2.25	0.00

Table 2.4—Veterans Field Example: assumed input elastic moduli of individual rock components.

I cross-validated the well-log-based estimates of elastic properties using core measurements obtained from static mechanical experiments using a conventional triaxial rock testing system. I estimated elastic properties of the core samples under a constant pore pressure of 6.9 MPa and hydrostatic conditions. The confining pressure was increased from 10 MPa to 40 MPa, at a constant loading rate of 0.5 MPa/min.

Next, I conducted rock classification using an unsupervised artificial neural network. The inputs to the network included well-log-based depth-by-depth estimates of (a) volumetric concentrations of minerals, (b) interparticle and intraparticle porosity, and (c) bulk and shear moduli.

Fig. 2.9 (Track 13) and Fig. 2.10 (Track 13) show the outcome of the petrophysical rock classification in WELL A and WELL B, respectively. The identified rock types were in agreement with the description of the identified geological facies and were verified using thin-section images and core samples.

According to the daily reports, depth interval of XX50–XY25 in WELL A was completed by acid fracturing and Well B was fractured at the depth intervals illustrated in black on Fig. 2.10 (Track 14). Fracturing in WELL A was successfully completed, as indicated on the reports. However, production from WELL B was negligible. The results of rock classification in WELL B show that the fractures in this well were initiated in the rock classes with low values of Young's modulus. Poor elastic rock properties (e.g., Young's modulus) could be a possible reason for unsuccessful fracture treatment in this well and consequent negligible production. However, additional geomechanical data and information about formation anisotropy is required to confirm this observation.

Furthermore, the results of rock classification (Figs. 2.9 and 2.10, Track 13) were used to update Archie's parameters to improve estimates of water saturation. **Table 2.5** lists the Archie's porosity exponent, *m*, in the identified petrophysical rock classes. Constant values of 1 and 2 were used for Archie's Winsauer factor, *a*, and Archie's saturation exponent, *n*, respectively. The same table lists the petrophysical and elastic properties of the identified petrophysical rock classes. All the previously estimated petrophysical and compositional properties were finally updated based on the petrophysical rock classification.

Rock Class	Interparticle Porosity	Young's modulus (GPa)	*m*
1	0.24 ± 0.62	65.50 ± 7.10	2.09 ± 0.33
2	0.12 ± 0.02	62.31 ± 9.74	1.84 ± 0.22
3	0.06 ± 0.02	82.25 ± 11.3	2.00 ± 0.22
4	0.04 ± 0.03	75.74 ± 8.50	1.95 ± 0.20
5	0.10 ± 0.03	71.95 ± 4.30	2.03 ± 0.35

Table 2.5—Veterans Field Example: general properties of the identified petrophysical rock classes.

Figs. 2.9 and 2.10 (Tracks 7-11) show the final estimates of mineral composition, total porosity, interparticle and intraparticle porosity, as well as the estimates of Young's modulus, compared to the corresponding core measurements, in WELL A and WELL B, respectively. **Fig. 2.11** illustrates a cross-plot of the well-log-based estimates of Young's modulus compared to the core measurements in WELL A. I observed average relative error of about 8% in well-log-based estimates of Young's modulus compared to core measurements. The estimates of interparticle porosity involved a 14% average relative error, compared to the core measurements. The estimates of porosity also were qualitatively validated using thin-section analysis.

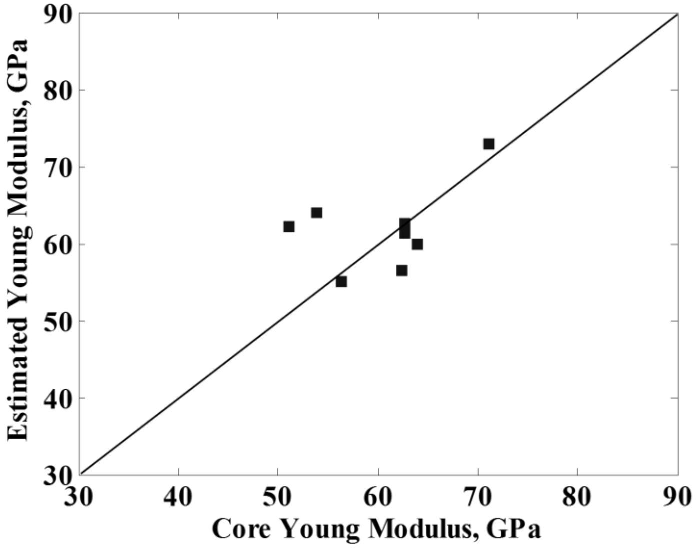

Fig. 2.11—Veterans Field Example: cross-plot of the estimates of Young's modulus compared against their core measurements. There is an average relative error of approximately 8% in the assessment of Young's modulus.

Fig. 2.12 compares the estimates of interparticle porosity obtained by Wyllie's time-average equation and the ones from SCA method, compared against core measurements of interconnected porosity in WELL A. The results show 40% improvement in porosity assessment using the SCA method.

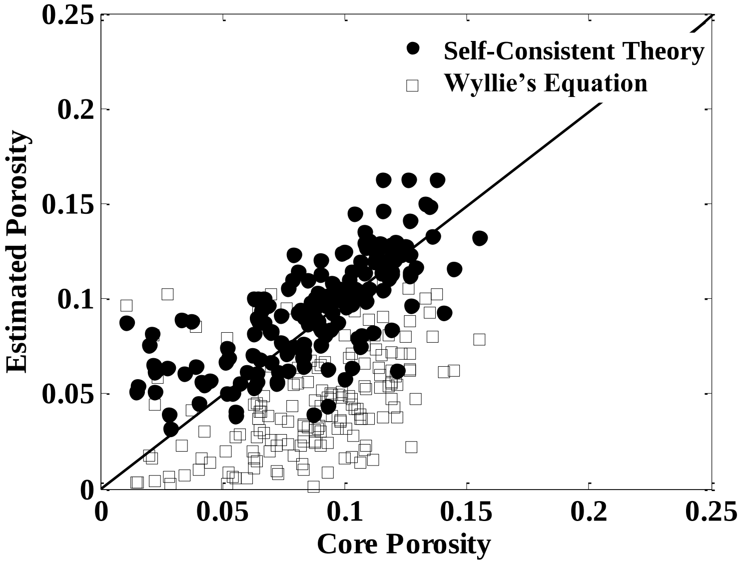

Fig. 2.12—Veterans Field Example: comparison of porosity estimated using Wyllie's method and SCA theory, against core measurements. Estimates of porosity obtained from Wyllie's method have 50% average relative error, while estimates of porosity obtained from SCA theory have only 10% average relative error.

Finally, I estimated permeability based on the core-derived porosity-permeability correlations in each rock type. Fig. 2.9 (Tracks 14 and 15) and Fig. 2.10 (Tracks 15 and 16) compare the estimates of permeability and water saturation against core measurements in WELL A and WELL B, respectively. **Fig. 2.13** shows a comparison of initial estimates of permeability obtained using the core-derived porosity-permeability correlation for the entire depth interval of interest and final estimates of permeability, acquired using the core-derived porosity-permeability correlation in each rock class, plotted against core measurements. Final estimates of permeability are improved by approximately 50%. Furthermore, a comparison of initial estimates of water saturation obtained using constant Archie's porosity exponent, *m*, and final water saturation calculated using a variable *m* in each rock class, against core measurements, showed that final estimates of water saturation are improved by approximately 20%.

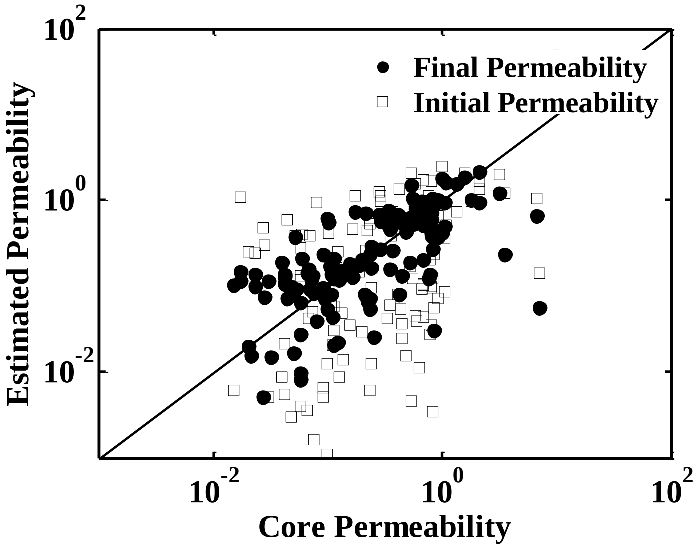

Fig. 2.13—Veterans Field Example: comparison of initial estimates of permeability obtained using core-derived porosity-permeability correlation for the entire depth interval of interest and final permeability, estimated using core-derived porosity-permeability correlation in each rock class, plotted against core measurements. Final estimates of permeability are improved by approximately 50%.

2.5 Sensitivity Analysis

I conducted a sensitivity analysis to investigate the impact of different pore types and shapes of matrix and pore inclusions on the effective electrical resistivity and elastic moduli. I built a synthetic case based on the formation properties of the Veterans field example. **Table 2.6** lists the assumed components of the synthetic matrix and their volumetric concentrations.

Rock Component	**Volumetric Concentration**
Calcite	0.40
Dolomite	0.15
Chert	0.01
Silt	0.02
Illite	0.07
Intraparticle Pores	0.05
Interparticle Pores	0.30

Table 2.6—Synthetic Case: rock components assumed for sensitivity analysis and their volumetric concentrations.

I assumed that the interparticle pores are fully saturated by fresh water-based mud-filtrate and intraparticle pores are saturated by saline fomation water. Table 2.4 lists the elastic moduli assumed for rock components and water. Table 2.2 lists the resistivity values assumed for formation water and drilling mud-filtrate.

Effective conductivity and elastic moduli are estimated using SCA method. **Fig. 2.14** shows the impact of interparticle and intraparticle porosity on the electrical resistivity and elastic properties of the rock. The results show that the intraparticle and interparticle porosity have a stronger impact on the electrical resistivity, compared to their impact on elastic moduli. An increase in interparticle porosity from 0.1 to 0.3, causes a decrease in electrical resistivity and bulk and shear moduli by approximately 50%, 42%, and 30%, respectively. Electrical resistivity and bulk and shear moduli decrease by approximately 60%, 27%, and 38%, respectively, with an increase in interparticle porosity from 0.1 to 0.3.

Next, I investigated the effect of aspect ratio of pores on electrical resistivity and elastic moduli using the SCA theories. **Fig. 2.15** shows that the shape of pore inclusions has a stronger influence on elastic moduli compared to its impact on electrical resistivity. On average, an increase in the aspect ratio of interparticle pores from 0.01 to 1, increases the electrical resistivity from 1 to 1.5 ohmm, whereas bulk and shear moduli are increased by approximately 3 and 7 times, respectively. I also investigated the impact of shape of calcite grains (i.e., the dominant mineral component in the Veterans field) on electrical resistivity and elastic moduli of the rock. The results showed that the shape of calcite inclusions has negligible impact on the electrical resistivity and elastic moduli, compared to the effect of pore shapes.

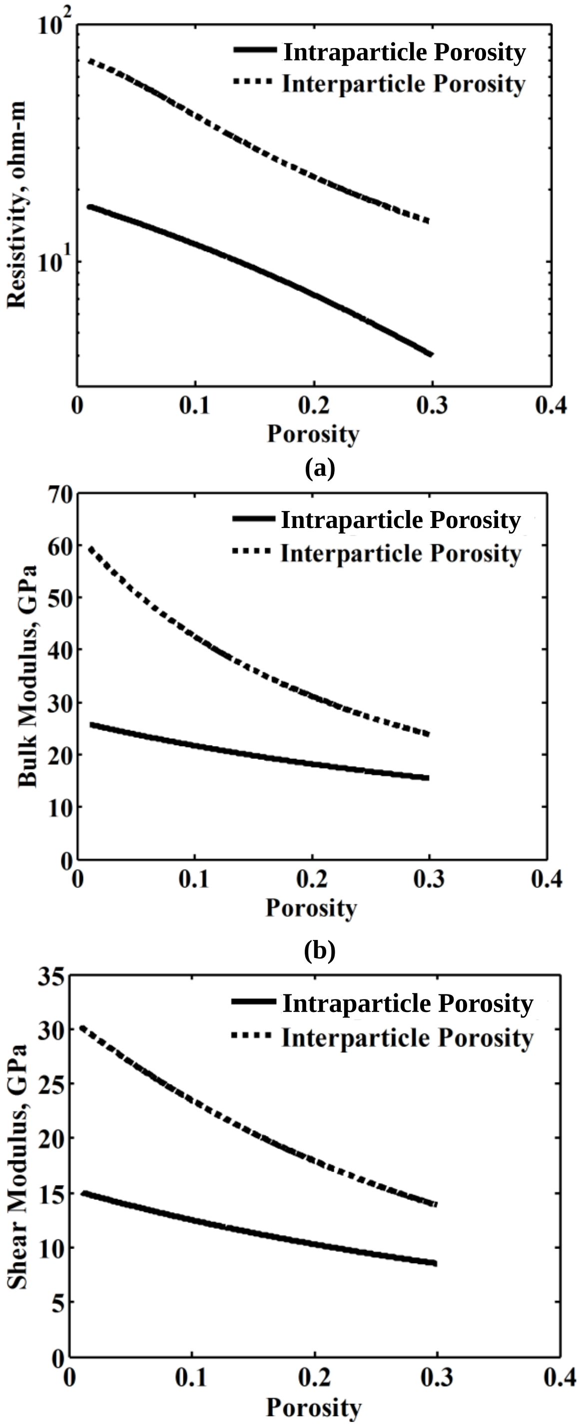

(a)

(b)

(c)

Fig. 2.14—Sensitivity analysis: impact of different pore types on (a) electrical resistivity, (b) bulk modulus, and (c) shear modulus of a synthetic case built based on formation properties of the Veterans field.

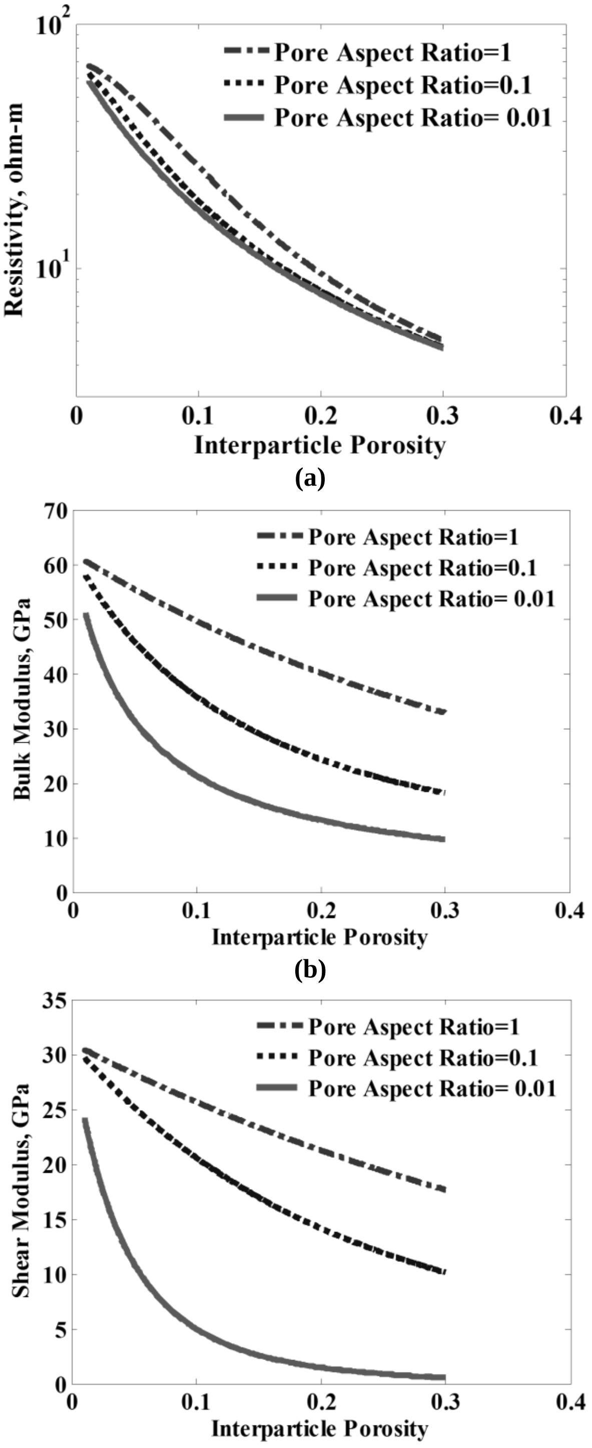

(a)

(b)

(c)

Fig. 2.15—Sensitivity analysis: impact of different shapes of pore inclusions on (a) electrical resistivity, (b) bulk modulus, and (c) shear modulus of a synthetic case built based on formation properties of the Veterans field.

2.6 Conclusions

An integrated rock classification technique was introduced to improve selection of fracture candidate zones in carbonate formations, by taking into account elastic properties, as well as petrophysical properties and mineralogy. First, geological facies classification was conducted based on depositional and diagenetic attributes in carbonate formations. Then, the conductive and the elastic Self-Consistent Approximation methods were implemented to estimate depth-by-depth elastic properties and porosity (i.e., interparticle and intraparticle) in each of the geological facies. The depth-by-depth well-log-based estimates of petrophysical, compositional, and elastic properties were applied to classify rock types.

This rock classification technique was successfully applied in the Veterans oil field, in west Texas. The estimates of interparticle porosity, as well as Young's modulus in WELL A and WELL B were in agreement with core measurements and thin-section images with 14% and 8% average relative error, respectively. The identified rock types were verified using thin-section images and core samples. A 40% improvement was observed in the assessment of interconnected porosity compared to the initial application of Wyllie's time-average equation. The estimates of permeability and water saturation in WELL A and WELL B were improved by approximately 50% and 20%, compared to those from conventional techniques. The results of rock classification in WELL B show that the low values of Young's modulus at fracture locations may be the reason for unsuccessful fracture treatment and negligible production from this well.

Furthermore, the petrophysical rock classification can improve selection of candidate zones for fracture treatment by taking into account petrophysical, compositional, and elastic rock properties. The rock classification in conjunction with reliable well-log-based assessment of permeability and water saturation can further improve the sweet-spot selection, while reducing the cost, by minimizing the number of perforations and fracture stages.

CHAPTER III

CHARACTERIZATION OF PORE STRUCTURE IN CARBONATE FORMATIONS USING A MULTI-MODAL GAUSSIAN FUNCTION FOR ANALYZING THE IMPACT OF PORE SYSTEMS ON ELECTRICAL RESISTIVITY

Carbonate formations are commonly characterized by complex pore networks that involve different pore systems with various shapes and interconnectivity. Petrophysical properties and flow characteristics are strongly controlled by the distribution of pore systems in the formation. Thus, a reliable characterization of pore structure in heterogeneous carbonate formations can enhance assessment of petrophysical properties. MICP measurements can be used for assessing the pore-throat radius modality and distribution. However, a large number of core samples are required for the assessment of heterogeneous distribution of pore systems in a carbonate formation.

In this chapter, I applied electrical resistivity logs and well-log-based estimates of porosity and permeability for prediction of pore types identified from MICP measurements. To minimize the discrepancy when predicting pore types at different measurement scales, I sequentially populated the identified pore types at the MICP domain to the core-plug and well-log scales. I first applied a multi-modal Gaussian function to characterize modality and distribution of pore-throat radius data obtained from MICP measurements. Then, I extrapolated the identified pore types at the well-log scale using well-log-based estimates of porosity and permeability and fluid-corrected resistivity logs. I investigated the impact of pore structure on electrical resistivity measurements by assessing the predictability of the formation pore types from electrical resistivity measurements.

3.1 Introduction

Successful development of heterogeneous carbonate reservoirs requires an accurate assessment of the flow units and corresponding petrophysical properties. Depositional and diagenetic modifications result in a complex pore structure of different shapes and interconnectivity in carbonate formations (Lucia 1995; Lucia 2007; Sok et al. 2010). Variable distributions of the pore systems can significantly impact petrophysical properties and flow characteristics of the formation. Reliable pore type identification can be performed using MICP measurements. MICP measurements can correspond to various attributes of pore systems, controlling flow in the reservoir, including pore volume, pore-throat size, pore connectivity, and pore-size homogeneity (Purcell 1949; Skalinski and Kenter 2014).

Several MICP-based pore typing techniques have been developed during recent decades. The Winland *R35* (Pittman 1992) utilized the pore-throat radius corresponding to 35% of mercury (non-wetting phase) saturation, derived from the MICP measurements, as an indicator of the effective flow properties. Marzouk et al. (1998)

defined three pore types (micropores, mesopores and macropores) in carbonate formations based on the pore-throat radius measured by MICP or air-water centrifuge. Furthermore, Clerke (2009) illustrated the use of Thomeer's hyperbolas (1960) for fitting MICP measurements to assess quantitatively the pore-size distribution in complex carbonate formations. In addition, Gaussian (or log-normal) density functions have been used for modeling pore-size and grain-size distributions (Spencer 1963; Nimmo 2004; Genty et al. 2007; Chicheng and Torres-Verdín 2013). In fact, the parameters associated with a Gaussian density function relate more directly to the pore modality and the attributes of the pore-size distribution, as compared to Thomeer's hyperbolas (Chicheng and Torres-Verdín 2013). Application of pore typing techniques based on MICP core measurements can improve understanding of flow mechanism in heterogeneous formations. However, a large number of core samples are required for a reliable assessment of heterogeneous distribution of pore systems in a carbonate formation. Alternatively, well logs can provide information about petrophysical properties of the formation at all depths along the wellbore.

Resistivity logs are sensitive to pore structure and fluid distribution in the formation (Archie 1942). Since the matrix of most carbonate rocks is a weak electrical conductor, the electrical current mainly flows through the fluid in the pore space. Thus, the size, shape, and connectivity of the pores and the pore throats influence the flow of electric charge. Although the impact of carbonate pore structure on electrical resistivity has been inferred, no quantitative evaluation of this effect exists (Brie et al. 1985). An approach for better understanding the effect of carbonate pore structure on resistivity measurements is to evaluate the predictability of core-based pore types from resistivity logs. In this chapter, I employed a multi-modal Gaussian function to identify pore types from quantitative characterization of the available MICP measurements in a carbonate formation. I evaluated the predictability of pore types from resistivity measurements at the well-log scale.

The main advantage of the introduced approach, as compared to conventional pore typing techniques, is simultaneous inclusion of pore system attributes corresponding to pore modality, pore volume, and pore connectivity, rather than incorporation of only one pore attribute or qualitative interpretation of MICP data. Application of the multi-modal Gaussian function yields the number of pore-throat radius modes in the formation. Thus, pore typing based on the Gaussian attributes is not restricted to a user-defined modality criteria.

3.2 Method

To minimize the discrepancy in prediction of pore types at different measurement scales, I determined pore types in each scale and sequentially extrapolated them from the smallest to the largest measurement scale. Thus, the first step in the method was pore typing based on the attributes of a multi-modal Gaussian function that characterizes pore-throat radius distribution in the porous medium. The identified pore types in the MICP domain were then extrapolated to the core-plug and well-log domains.

3.2.1 Pore Typing Based on MICP Data with a Multi-Modal Gaussian Function

Fig. 3.1 shows a typical plot of capillary pressure measurements, P_c, against saturation of the non-wetting fluid (i.e., mercury), S_{Hg}, in the porous medium.

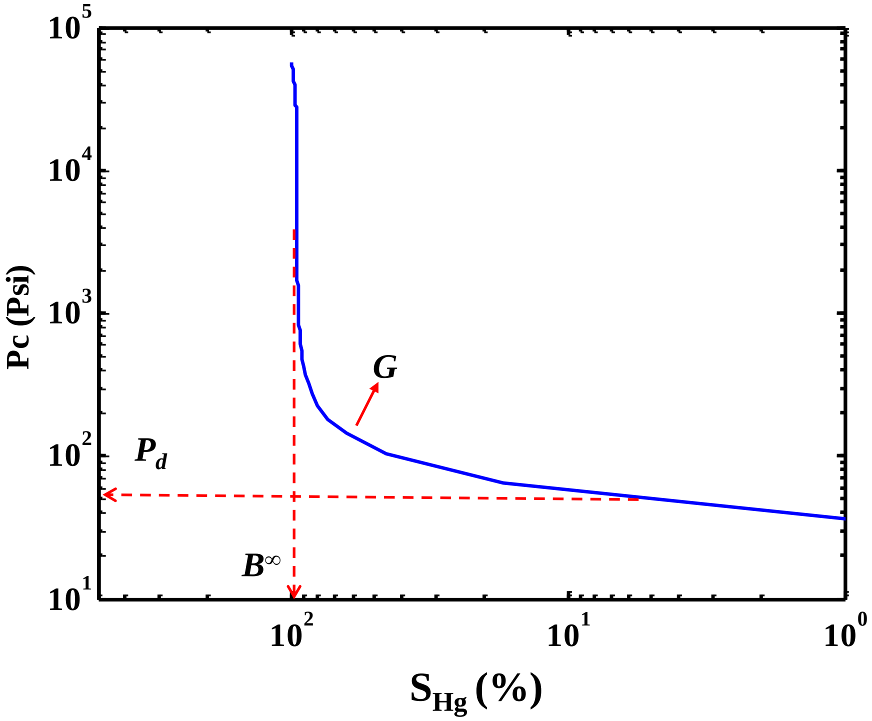

Fig. 3.1—Relationship between capillary pressure measurements and mercury saturation in the porous medium, represented by a hyperbolic function. P_d,is the displacement pressure, B^∞ is the bulk volume saturated by mercury at infinite pressure, and G is the geometric factor corresponding to the shape of the capillary pressure curve.

Three MICP curve parameters include the displacement pressure, P_d, the bulk volume saturated by mercury at infinite pressure, B^∞, and the geometric factor corresponding to the shape of the capillary pressure curve, G. These attributes can be identified using a hyperbolic function (Thomeer 1960; Lucia 1995) given by

$$S_{Hg} = B^{\infty} \exp\left(\frac{-G}{\log\left(\frac{P_c}{P_d} \right)} \right), \tag{3.1}$$

Moreover, for appropriate pore-size modality and distribution analysis, capillary pressure measurements are presented in terms of their corresponding throat-radius distribution by

$$P_c = \frac{2\Gamma \cos\theta}{r}, \tag{3.2}$$

where Γ is the interfacial tension, θ is the contact angle, and r is the pore-throat radius in μm. One approach to characterize the pore-throat radius distribution (in terms of incremental mercury saturation versus pore-throat radius) is to apply the derivative of Thomeer's hyperbola with respect to the pore-throat radius. However, it is often challenging to obtain a smooth pore-throat radius distribution from the differentiation method, as the result of limited and often noisy data points (Peters 2012; Chicheng and Torres-Verdín 2013). A more appropriate method is to apply a multi-modal Gaussian function for the best fit through the pore-throat radius measurements. Multi-modal Gaussian function is given by

$$\left(S_{Hg}\right)_{inc} = \sum_{i=1}^{T} a_i \exp\left[-\left(\frac{r-b_i}{c_i} \right)^2 \right], \tag{3.3}$$

where $(S_{Hg})_{inc}$ is the incremental mercury saturation, i corresponds to individual pore-throat radius modes, represented by individual Gaussian functions, T is the total number of the pore-throat radius modes, and a, b, and c are the fitting attributes of each Gaussian function. **Fig. 3.2** illustrates example of a bimodal Gaussian function with its corresponding fitting attributes to characterize the pore-throat radius distribution.

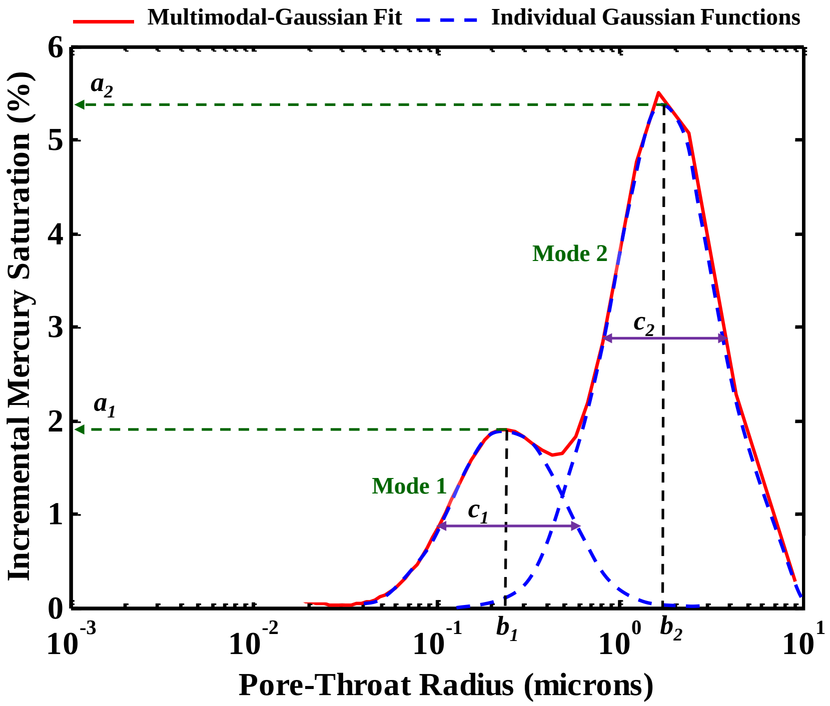

Fig. 3.2—A typical bimodal Gaussian function used for characterizing pore-throat radius distribution in the porous medium. *a* is the height of the peak of each pore-throat radius mode, corresponding to its fraction of pore volume saturated by mercury or flow capacity of the reservoir. *b* is the mean value of each mode's pore-throat radius. *c* is the width of each mode corresponding to the variability or standard deviation of each pore-throat radius mode.

Parameter *a* is the height of the peak of each pore-throat radius mode, corresponding to its fraction of pore volume saturated by mercury or flow capacity of the reservoir. Parameter *b* is the mean value of each mode's pore-throat radius. Larger values of *b* indicate higher hydraulic conductivity. Flow capacity or permeability is controlled by both parameters *a* and *b*. Furthermore, the width of each mode is represented by parameter *c*, designating the variability or standard deviation of each pore-throat radius mode. The maximum number of modes considered in this analysis were four, to maintain viable petrophysical bounds and to be consistent with the previous observations in carbonate formations. The number of the modes and fitting parameters was optimized by implementing the Levenberg–Marquardt algorithm (Levenberg 1944; Marquardt 1963) to minimize the cost function given by

$$f(N, \mathrm{a}_i, \mathrm{b}_i, \mathrm{c}_i) = \left\| \left(S_{Hg}\right)_{inc}^{\mathrm{mod}el} - \left(S_{Hg}\right)_{inc}^{\mathrm{meas}} \right\|_2^2, \tag{3.4}$$

where $\left(S_{Hg}\right)_{inc}^{\mathrm{mod}el}$ is the modeled incremental mercury saturation and $\left(S_{Hg}\right)_{inc}^{\mathrm{meas}}$ is the incremental mercury saturation obtained from MICP measurements. *K*-means clustering (MacQueen 1967; Lloyd 1982; Spath 1985) is then conducted using the fitting attributes of the multi-modal Gaussian function to determine pore types. The *K*-means technique partitions a dataset into a small number of clusters by minimizing the distance between each data point and the center of the cluster.

3.2.2 Pore Typing in the Core and Well-Log Domains

Fig. 3.3 shows the procedure for populating identified pore types based on the MICP measurements in the core and well-log domains.

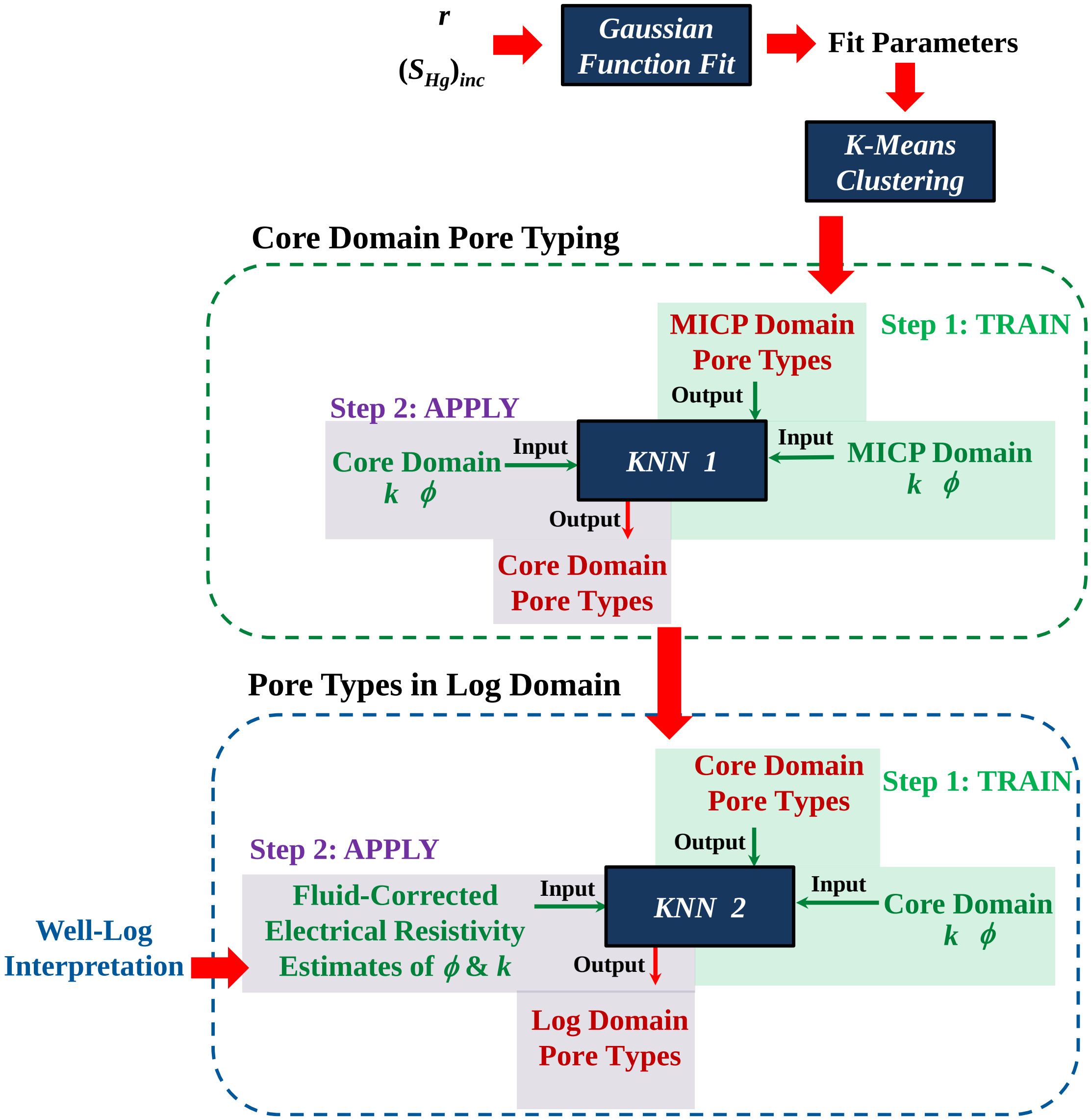

Fig. 3.3—A workflow for populating MICP-based pore types in the core and well-log domains.

First, I applied the *k*-Nearest Neighbors (*KNN*) algorithm (Cover and Hart 1967) to train a supervised model with an input of MICP porosity and permeability measurements and an output of the MICP-based pore types. I validated the model for predicting the MICP-based pore types using 20% of the training dataset. I then applied the supervised model to populate the identified pore types in the core domain using an input of core-plug porosity and permeability measurements. Next, I used another *KNN* model, trained using core-plug porosity and permeability measurements, and identified core-based pore types (after validation), to predict pore types in the well-log domain. The inputs to this model were electrical resistivity measurements and well-log-based estimates of porosity and permeability. The well-log-based estimates of porosity were obtained from a joint-interpretation of conventional well logs, using Wyllie's time-average equation (Wyllie et al. 1956) and Archie's equation (Archie 1942). The well logs used for this analysis included gamma ray (GR), electrical resistivity, density, neutron porosity, Photoelectric Factor (PEF), and compressional-wave slowness. Permeability estimates in the well-log domain were obtained by applying a supervised model based on *KNN* algorithm, with an input of core porosity and permeability measurements. The model was trained using 80% of the input dataset and tested on the remaining 20%. The predictability of core-based pore types from resistivity measurements was evaluated by quantifying the correlation between resistivity measurements and predicted pore types.

3.3 Field Example: The SACROC Unit, West Texas

I applied the proposed method to three wells at the SACROC (Scurry Area Canyon Reef Operators Committee) Unit located in the Midland basin, west Texas. The producing formation in this field is Canyon Reef, a Pennsylvanian limestone that has a heterogeneous distribution of petrophysical properties as well as lateral and vertical discontinuity of porosity and permeability, due to its formation in high-amplitude sea-level fluctuations during glaciation (Kane 1979; Brnak et al. 2006). Geological interpretations show that the SACROC Unit is composed of massive amounts of bedded bioclastic limestone and thin shale beds representing the Strawn, Canyon, and Cisco Groups of the Pennsylvanian. In particular, the Cisco and Canyon Groups are mostly composed of limestone with minor amounts of locally present shale (Han et al. 2010).

I used the multi-modal Gaussian functions to characterize pore-throat radius distributions, obtained from 24 MICP measurements in three understudied wells of the SACROC Unit. The MICP measurements were conducted using rock-chip samples (smaller in size compared to conventional core plugs). The Gaussian function analysis yielded the fitting attributes and the number of the required function modes to fit the data, corresponding to the number of the pore-throat radius modes, for each sample. **Fig. 3.4** shows an example of the Gaussian function fit to one of the sample measurements, exhibiting pore-size bimodality, and the corresponding attributes of the bimodal Gaussian function. I determined three pore types by implementing *KNN* clustering on all the attributes of the multi-modal Gaussian functions. **Fig. 3.5** illustrates pore-throat radius distribution for each of the identified pore types. The identified pore types are distinct with respect to pore-size modality, flow capacity (i.e., parameter *a*), and hydraulic conductivity (i.e., parameter *b*). Pore type 1 is predominantly monomodal and corresponds to the best pore type with the highest flow capacity and hydraulic conductivity. Pore type 2 and pore type 3 have a lower flow capacity compared to pore type 1. Pore type 2 exhibits pore-throat radius bimodality, while pore type 3 is primarily monomodal. One sample in pore type 3 (pointed out by the red arrow in Fig. 3.5c) corresponds to relatively low pore-throat radius. As this pore-throat radius size is not well represented by the available MICP data, I included this sample in the most similar category, pore type 3.

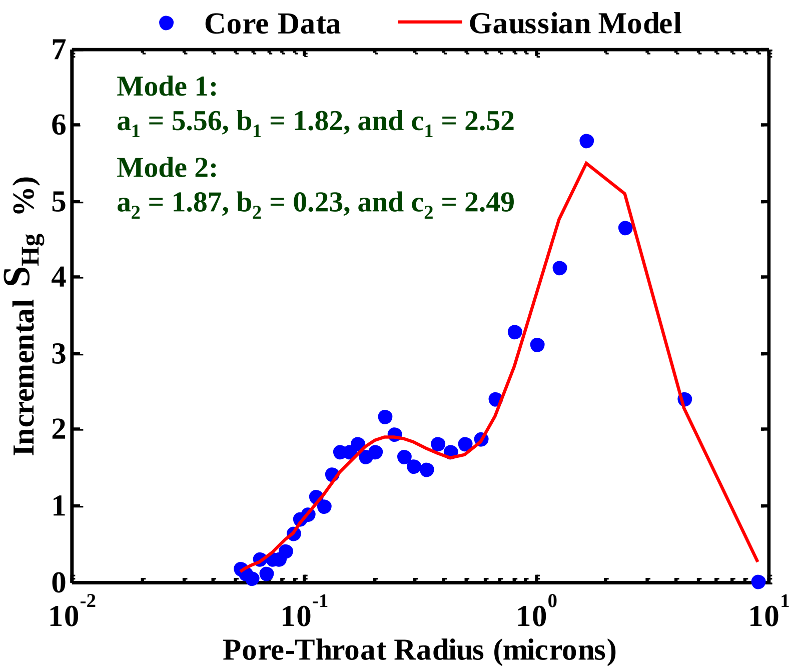

Fig. 3.4—SACROC Unit Field Example: an example of the multi-modal Gaussian function fit to pore-throat radius distribution, exhibiting pore-size modality, and the corresponding fit attributes.

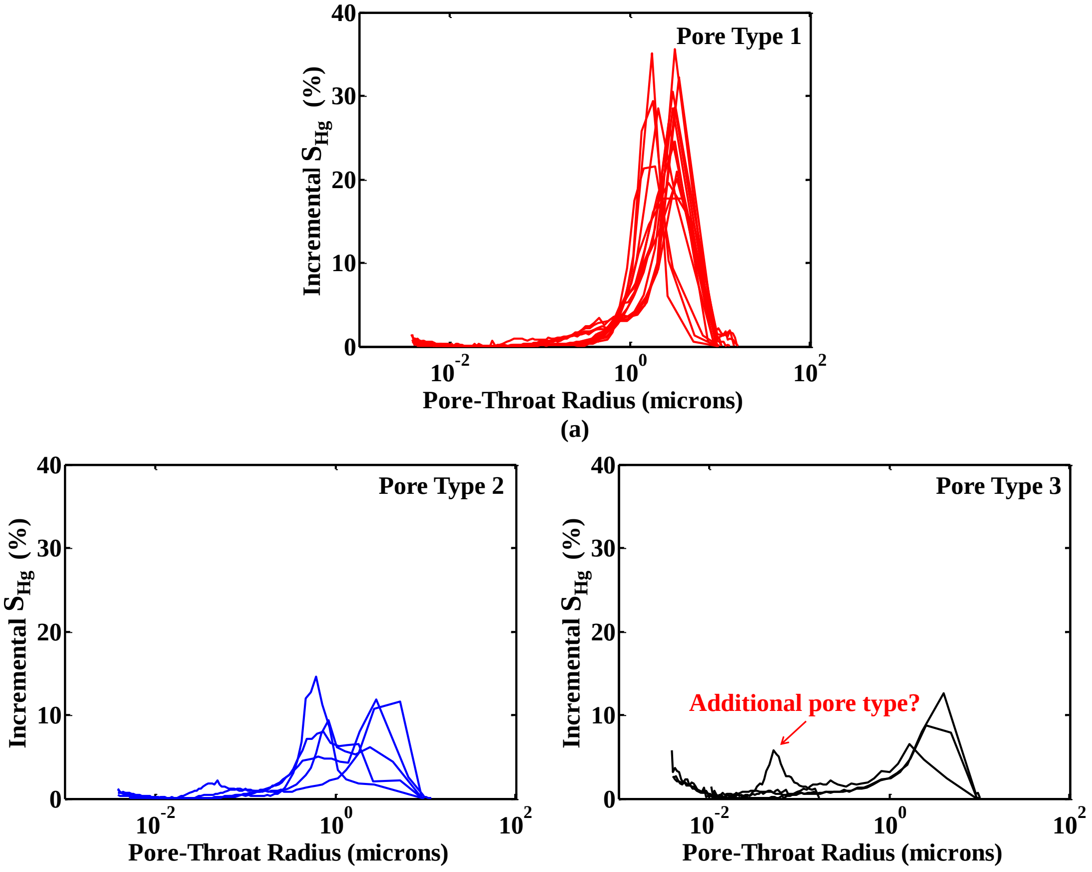

(a)

(b)

(c)

Fig. 3.5—SACROC Unit Field Example: pore-throat radius distributions of the identified pore types. Pore type 1 is predominantly monomodal and corresponds to the best pore type with the highest flow capacity (parameter *a*) and hydraulic conductivity (parameter *b*). Pore type 2 and pore type 1 have a lower flow capacity compared to pore type 1. Pore type 2 exhibits pore-throat radius bimodality, while pore type 3 is predominantly monomodal. One sample in pore type 1 (pointed out by the red arrow) corresponds to relatively low pore-throat radius. As this pore-throat radius size is not well represented by the available data, I included this sample in the pore type 1 category.

Fig. 3.6 shows all the identified pore types projected on (a) a plot of incremental mercury saturation and (b) a standard plot of capillary pressure measurements against mercury saturation. Furthermore, **Fig. 3.7a** indicates that the identified pore types correspond to unique ranges of porosity and permeability. This observation is consistent with the properties of the pore types in terms of their flow capacity and hydraulic conductivity.

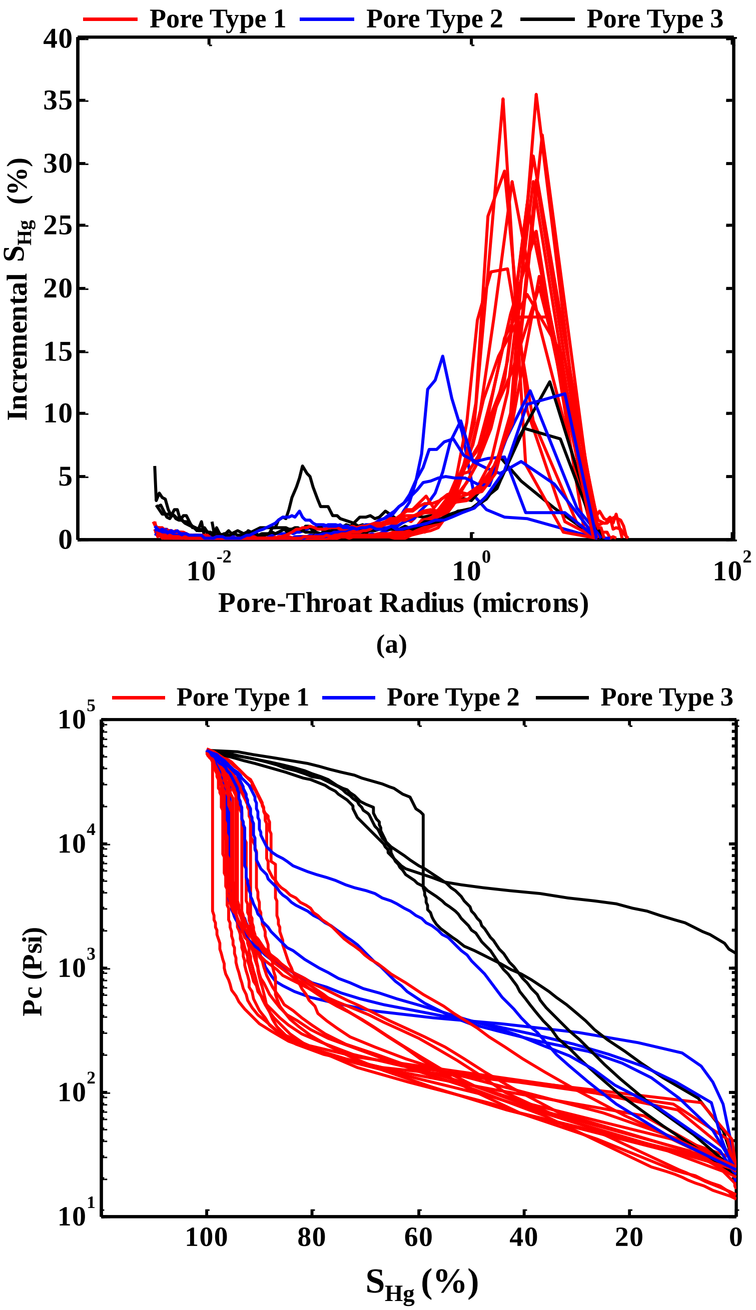

(a)

(b)

Fig. 3.6—SACROC Unit Field Example: identified pore types projected on (a) a plot of incremental mercury saturation versus pore-throat radius and (b) a plot of capillary pressure versus mercury saturation.

Next, I applied the *KNN* algorithm to populate the identified MICP-based pore types in the core-plug domain, using an input of core-plug porosity and permeability measurements. A relative average error of approximately 3% was associated with a blind test of the *KNN* model used to predict the MICP-based pore types in the core-plug domain. **Fig. 3.7b** shows the identified pore types in the core-plug domain projected on a plot of permeability versus porosity. A comparison of **Fig. 3.7b** with **Fig. 3.7a** illustrates that the pore types in the core-plug domain are consistent with the identified MICP-based pore types in terms of their corresponding porosity and permeability. Moreover, I conducted joint-interpretation of available conventional well logs to assess porosity and mineralogy in three understudied wells of the SACROC Unit. The productive interval of the Canyon Reef is mainly composed of limestone and minor concentrations of shale. Therefore, the types of minerals in the well-log interpretation were assumed to be calcite and clay. The outcome of the well-log interpretation was depth-by-depth estimates of porosity, volumetric concentrations of minerals, and water saturation.

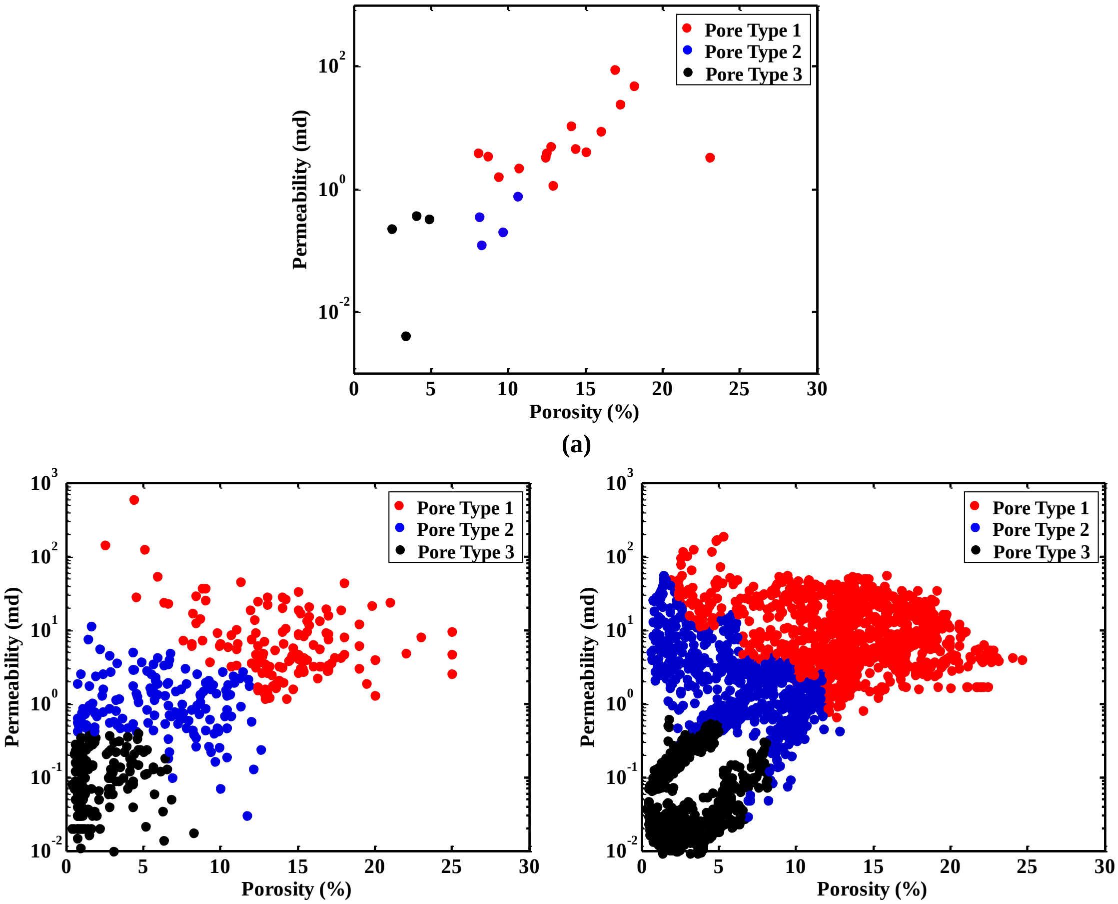

(a)

(b) (c)

Fig. 3.7—SACROC Unit Field Example: identified pore types projected on a plot of permeability versus porosity in (a) MICP domain, (b) core-plug domain, and (c) well-log domain. The identified pore types are consistent, with respect to their corresponding porosity and permeability distributions, in all three measurement scales.

Core descriptions served to verify the estimates of mineralogy. The estimates of porosity and permeability were validated using the available core measurements (**Fig. 3.8**). Assessment of water saturation, however, was not a focus of this work, as the SACROC Unit was put through extensive water flooding. Well-log-based estimates of permeability were obtained from a *KNN* model constructed using core porosity and permeability measurements. I used well-log-based estimates of permeability and porosity, as well as the fluid-corrected deep resistivity log measurements to extrapolate the core-plug-domain pore types in the well-log domain. The blind test showed an average relative error of approximately 5% in predicting core-plug-based pore types in the well-log domain. **Fig. 3.7c** illustrates the distribution of the well-log-based estimates of porosity and permeability in the identified pore types. **Table 3.1** further lists the properties of pore types in the well-log domain. The results show that the outcome of pore typing in the well-log domain is consistent with the pore types determined in the MICP-core and core-plug scales. A similar conclusion can be drawn from the comparison between pore types identified in the core-plug and well-log scales demonstrated in Fig. 3.8. In addition, the fluid-corrected resistivity well log exhibited a correlation coefficient of approximately 57% with the identified pore types and its application resulted in an accurate prediction of pore types in the well-log scale. This confirms that the resistivity measurements are significantly affected by the formation pore structure and can be used for assessing porosity inn carbonate formations.

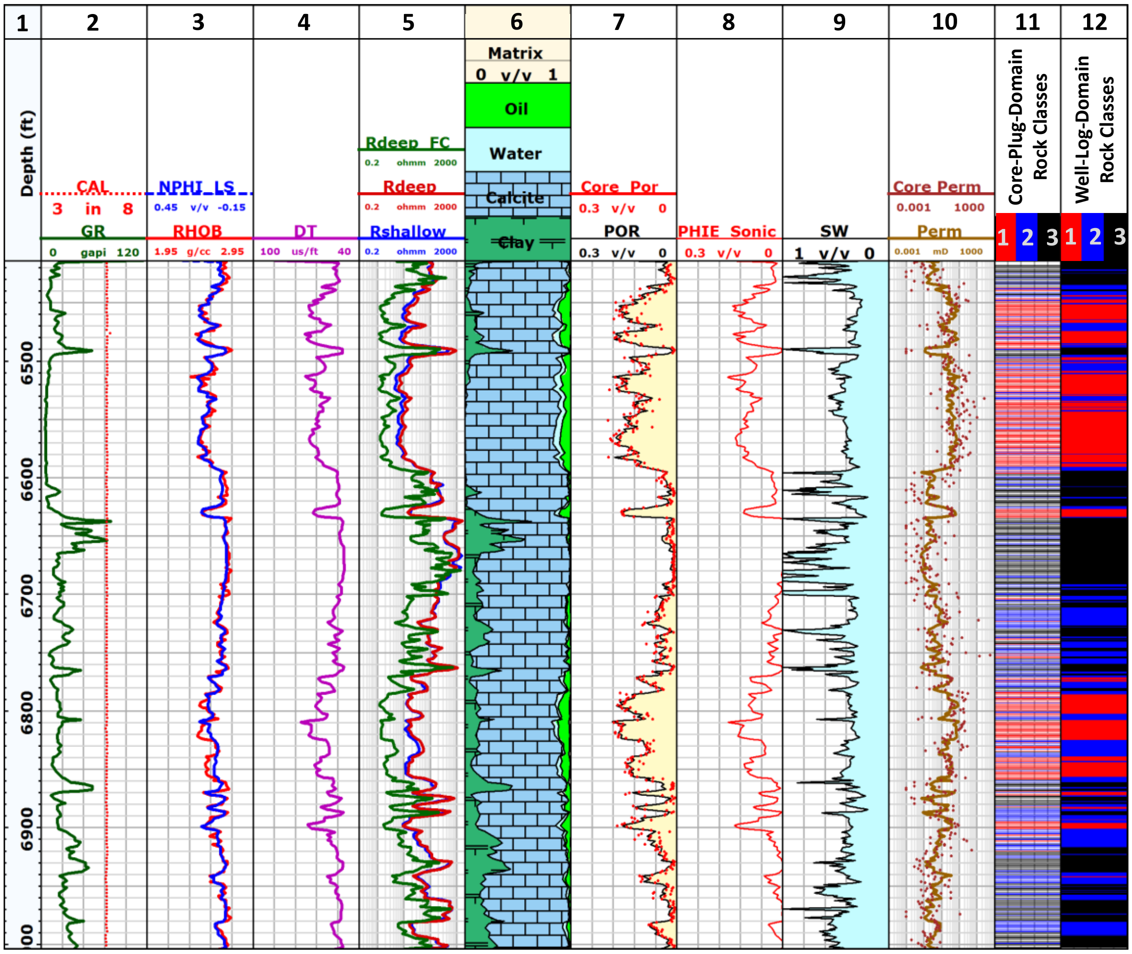

Fig. 3.8—SACROC Unit Field Example: conventional well logs and results of well-log interpretation, permeability assessment, and pore typing in a key well. Tracks from left to right include, Track 1: depth; Tracks 2-5: GR, caliper, neutron porosity (in water-filled limestone units), bulk density, compressional-wave slowness, and apparent resistivity logs (including the fluid-corrected deep resistivity log); Track 6: estimates of volumetric concentrations of calcite and clay; Track 7: estimates of total porosity, compared to core measurements (red dots); Track 8: estimates of effective porosity from acoustic measurements; Track 9: estimates of water saturation; Track 10: estimates of permeability, compared to core measurements; Track 11: outcome of pore typing in core-plug domain; Track 12: outcome of pore typing in well-log domain.

Rock Class	Porosity (%)	Permeability (md)	Deep Resistivity
1	13.6 ± 4.0	12.5 ± 3.8	3.5 ± 1.2
2	6.6 ± 3.2	3.5 ± 2.4	34.5 ± 10.7
3	3.1 ± 1.7	0.2 ± 0.1	134.6 ± 89.6

Table 3.1—SACROC Unit Field Example: properties of identified pore types in the well-log domain.

3.4 Conclusions

In this chapter, I conducted pore typing at three different measurement scales, including MICP-core, core-plug, and well-log scales, and investigated the predictability of the formation pore types from electrical resistivity measurements. I used a multi-modal Gaussian function to characterize pore-size modality and distribution obtained from MICP data in the SACROC Unit. Pore typing generated three distinct pore types in each measurement scale. The best pore type, pore type 1, was predominantly monomodal and corresponded to the highest flow capacity and hydraulic conductivity. Pore type 2 was characterized with pore-throat radius bimodality. Pore type 2 and pore type 3 had a lower flow capacity compared to pore type 1. Application of the deep resistivity log together with well-log-based estimates of porosity and permeability resulted in an accurate prediction of pore types in the well-log domain. The results further indicated a correlation coefficient of approximately 57% between the fluid-corrected resistivity measurements and the formation pore types. These results show that the pore structure has a strong influence on the electrical resistivity measurements. Thus, these measurements can be incorporated in the assessment of porosity in carbonate reservoirs.

CHAPTER IV

APPLICATION OF CONVENTIONAL WELL LOGS TO CHARACTERIZE SPATIAL HETEROGENEITY IN CARBONATE FORMATIONS REQUIRED FOR PREDICTION OF ACID FRACTURE CONDUCTIVITY*

Acid etching, as the consequence of heterogeneous distribution of petrophysical properties and mineralogy, results in the conductivity of acid fractures in carbonate reservoirs. Reliable characterization of small-scale formation spatial heterogeneity using geostatistical analysis (i.e., variogram analysis) can significantly improve prediction of acid fracture conductivity. Previous publications suggest that permeability correlation length can be used to assimilate spatial heterogeneity in prediction of acid fracture conductivity. Well logs are good candidates to provide information about petrophysical and compositional properties of the formation with the required resolution for prediction of acid fracture conductivity. However, the assessment of permeability and mineralogy from conventional well logs is challenging as the result of high spatial heterogeneity and complex pore structure. Rock typing has been suggested in the literature to improve permeability assessment in carbonates.

---

*Reprinted with permission from "Application of Conventional Well Logs to Characterize Spatial Heterogeneity in Carbonate Formations Required for Prediction of Acid-Fracture Conductivity" by Mehrnoosh Saneifar, Zoya Heidari, and A.D. Hill, 2014. *SPE Production and Operations Journal,* Pre-print, Copyright 2014 by the Society of Petroleum Engineers.

Most of the previously introduced rock typing methods are dependent on core measurements. However, core data are generally sparse and not available with the sampling rate required for prediction of acid fracture conductivity.

The main objective of this chapter is to quantify formation spatial heterogeneity using variogram analysis of well logs and well-log-based estimates of petrophysical and compositional properties in carbonate reservoirs. I introduce an iterative permeability assessment technique based on well logs, which takes into account characteristics of different rock classes in the reservoir. Furthermore, I propose three rock classification techniques based on conventional well logs which take into account static and dynamic petrophysical properties of the formation as well as mineral composition.

I successfully applied the proposed techniques in two carbonate formations, Happy Spraberry oil field and Hugoton gas field.

4.1 Introduction

Non-uniform dissolution of rock during acid fracturing, caused by heterogeneous distribution of petrophysical properties and mineralogy in carbonate formations, results in acid etching on fracture faces. Fractures remain conductive under closure stress, as the high points on the etched surface act as pillars to keep the fracture channel open. Characterization of small-scale formation spatial heterogeneity is necessary to accurately predict acid fracture conductivity. A recent acid fracture model utilizes a geostatistical parameter, correlation length, to include spatial variation of permeability for prediction of fracture conductivity (Mou et al. 2011; Deng et al. 2011; Oeth et al. 2013).

Previous studies applied permeability data from cores and outcrops to estimate the correlation length from variogram analysis (Goggin et al. 1992; Kittridge et al. 1990). Permeability measurements from outcrops may not be representative of the reservoir conditions. Recent studies showed improvement in the assessment of permeability based on MICP measurements (Buiting and Clerke 2013; Clerke et al. 2008; Clerke 2009). Numerous data points are required at small scales for a reliable variogram analysis. However, core measurements are typically sparse and can be inadequate in identifying the correlation length (Oeth et al. 2011). Well logs can be used for estimating correlation length, as they are recorded at small scales and are available at all depths along the wellbore. A high-resolution assessment of permeability distribution based on well logs can result in accurate estimation of geostatistical parameters and improved prediction of acid fracture conductivity.

Nevertheless, permeability assessment based on well logs in carbonate formations is challenging. The conventional porosity-permeability regression techniques are not reliable in carbonate formations as a result of complex pore structure and highly-variable petrophysical and compositional properties. Empirical permeability correlations developed mainly based on sandstone core measurements are not reliable in carbonate formations (Wyllie and Rose 1950; Timur 1968; Katz and Thompson 1986; Coates and Denoo 1981). Several studies developed a correlation of permeability with different well logs using statistical multiple regression techniques (Yao and Holditch 1993; Saner et al. 1997; Mohaghegh et al. 1997; Xue et al. 1997; Mathisen et al. 2003). The limitation of this approach is the complicated nature of the relationship between petrophysical parameters and well-log attributes. In addition, each correlation is unique for the specific formation it is developed in and cannot be generalized for permeability assessment in other formations (Babadagli and Al-Salimi 2002).

Unconventional well logs such as neutron capture spectroscopy and NMR can be used along with conventional well logs to improve the assessment of lithology and static/dynamic petrophysical properties (Clerke et al. 2014). However, these advanced tools are not available in all the wells. Therefore, assessment of permeability and lithology using conventional well logs remains a challenge for petrophysicists in carbonate formations.

Previous publications suggest that a reliable petrophysical rock classification can significantly improve permeability assessment in reservoirs with extensive rock features (Lucia 1995; Jennings and Lucia 2003; Lucia 2007). Methods such as Leverett's *J*-function (Leverett 1941) and Winland's *R35* (Pittman, 1992) classify rock classes based on pore throat size obtained from saturation-dependent capillary pressure. Other methods such as rock fabrics number (RFN) (Lucia 1995) are based on correlations among permeability, porosity, and particle size/rock fabric. Most of the common rock typing techniques are strongly dependent on core data. However, core measurements are usually limited and not available at high sampling rates required for capturing the heterogeneous distribution of lithology and permeability of carbonate formations. Therefore, the conventional rock typing methods can fail in detecting all rock variations in heterogeneous carbonate reservoirs. Furthermore, it is necessary to take into account dynamic petrophysical properties such as saturation-dependent capillary pressure and relative permeability in carbonate rock typing (Al-Farisi et al. 2009). These measurements are not available real-time and are usually limited to core data.

Recent publications investigated the effect of rock classes on mud-filtrate invasion and its consequent impact on well logs. These publications used numerical simulations of mud-filtrate invasion in homogeneous pore structures (Xu and Torres-Verdín 2012; Xu et al. 2012; Gandhi et al. 2010; Heidari et al. 2011). Similar methods were proposed to incorporate numerical simulations of mud-filtrate invasion for assessment of permeability, saturation-dependent capillary pressure, and relative permeability (Salazar et al. 2006; Heidari and Torres-Verdín 2012; Gandhi et al. 2010; Heidari et al. 2011; George et al. 2003; Miranda et al. 2009). However, in the case of carbonate formations, the complex pore structure significantly affects the process of mud-filtrate invasion. Consequently, it is challenging to quantify the impact of rock classes on spatial distribution of fluids in near wellbore region (i.e., due to mud-filtrate invasion) in carbonate formations.

Moreover, previous studies introduced analytical rock quality factors based on real-time well logs for petrophysical rock classification in siliciclastic formations (Gandhi et al. 2010; Heidari et al. 2011). These factors qualitatively take into account the impact of rock classes on mud-filtrate invasion to include dynamic petrophysical properties for reliable rock classification.

Other approaches for rock classification based on well logs include application of classical statistical methods such as clustering (Ye et al. 1998) and discriminant analysis (Silva et al. 2002; Lee and Datta-Gupta 2002). However, these approaches cannot reliably identify distinct groups in data with no multivariate-normal distribution, such as well logs. Artificial neural network techniques are more suitable approaches for rock classification based on well logs as they do not assume multivariate-normal distribution (Skalinski et al. 2005).

I proposed an iterative process to improve permeability assessment using conventional well logs. This method uses well-log-derived rock classes for the assessment of depth-by-depth permeability. I introduced three rock classification approaches that employ conventional well logs to classify rock classes in carbonate formations. The first rock typing approach applies a new real-time analytical factor based on conventional well logs and include (a) separation of shallow and deep electrical resistivity logs as a result of mud-filtrate invasion that is controlled by static and dynamic petrophysical properties, (b) porosity, (c) volumetric concentration of shale, and (d) original fluid saturations (i.e., in the case of rock-fluid quality index) (Saneifar et al. 2014b).

The second and the third approaches include application of a supervised and an unsupervised artificial neural network. I detected different patterns induced as a result of the cumulative effect of static/dynamic petrophysical properties as well as the effect of interconnected porosity, variation of fluid saturations, and mineralogy on well logs. The supervised artificial neural network was trained with well logs and well-log-based estimates of petrophysical properties for depths with predicted lithofacies/rock classes. The trained network was employed to implement rock typing throughout the desired depth interval. This technique is highly dependent on core measurements in the field. However, after training the network for a specific field, the network can be applied in any well drilled in the same formation to provide rock classes and permeability estimates independent from core measurements. The unsupervised artificial neural network used in this study was based on the Hierarchical clustering algorithm. This technique is not dependent on core measurements for rock classification (Saneifar et al. 2014b).

The contribution of the proposed rock classification techniques compared to the previously introduced methods are (a) minimal dependence on core measurements for rock classification, (b) qualitatively honoring cumulative effect of static and dynamic petrophysical properties on well logs, and (c) taking into account the effect of fluid saturations and mineralogy on well logs for improved rock classification and permeability assessment. I finally conduct variogram analysis of conventional well logs and well-log-based estimates of petrophysical properties and mineralogy to quantify formation spatial heterogeneity in carbonate reservoirs.

The following sections describe the introduced methods for permeability assessment and rock classification as well as their application in two carbonate formations including (a) Hugoton gas field in Kansas and (b) Happy Spraberry oil field in Texas.

4.2 Method

Fig. 4.1 shows a flowchart summarizing the proposed approach in this chapter. Basic well-log interpretation was the first step for rock classification and permeability assessment. I conducted multi-mineral analysis by joint inversion of conventional well logs. The input to multi-mineral analysis included (a) well logs such as GR (gamma ray), electrical resistivity, bulk density, neutron porosity, PEF (Photoelectric Factor), and compressional-wave slowness (if available) logs and (b) the response of well logs to pure minerals (Schlumberger 1989). As a preliminary requirement for well-log interpretation, I checked the well logs and core data for any required depth-shifting. The outcome of multi-mineral analysis were simultaneous estimates of porosity, fluid saturations, and volumetric concentration of minerals. I then classified petrophysical rock classes based on well logs and estimate depth-by-depth permeability in each rock class. Geostatistical analysis was conducted using well logs, well-log-based petrophysical and compositional properties to characterize formation spatial heterogeneity (Saneifar et al. 2014b). The following sections explain the introduced methods for permeability assessment, rock classification, and geostatistical analysis.

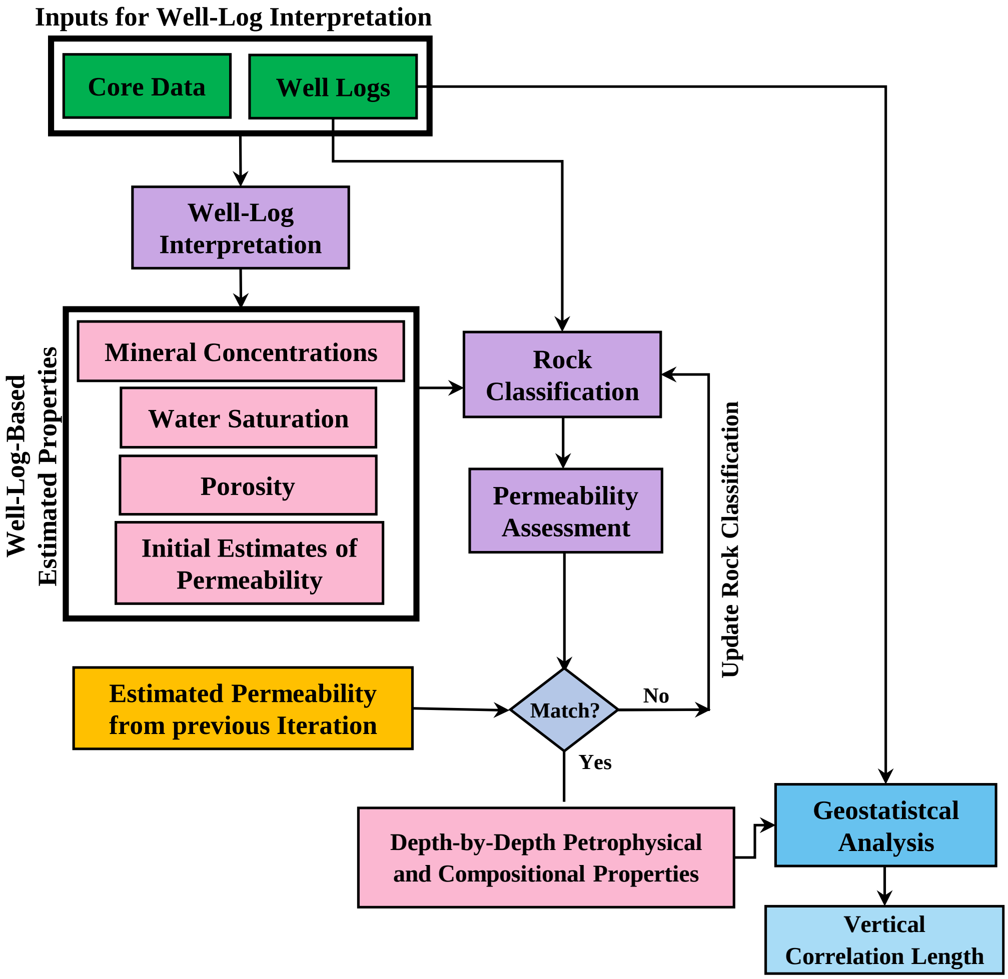

Fig. 4.1—Flowchart of the proposed method for permeability assessment, rock classification, and geostatistical analysis.

4.2.1 Iterative Approach to Enhance Permeability Assessment

I applied an iterative technique for simultaneous assessment of rock classes and permeability. The iterative process started with an initial rock classification based on two approaches: (a) analytical rock quality index and (b) artificial neural network, explained further in the following sections. I then estimated permeability using the estimates of porosity by applying the core-derived porosity-permeability correlation in each rock class. The updated permeability estimates supported by well-log-based rock classification can then be applied as the input for any desired well-log-based rock classification technique. The new rock classes can be used to update permeability estimates until a convergence criterion is met. Incorporation of permeability estimates from other production data, such as well tests, inflow performance, production logs, where available, can also further enhance the outcome of the applied rock classification techniques (Saneifar et al. 2014b).

4.2.2 Rock Classification Using Analytical Rock Quality Index

I introduced rock quality index (*RQI)* and rock-fluid quality index (*RFQI)*, which can be calculated real-time and depth-by-depth using well logs. The dimensionless indices correspond to a combined impact of porosity, clay content, and separation of shallow and deep resistivity well logs on the formation quality. The separation of shallow and deep resistivity occurs as the result of cumulative mud-filtrate invasion and is affected by the static and the dynamic petrophysical properties, such as permeability saturation-dependent relative permeability and capillary pressure (Gandhi et al. 2010; Heidari et al. 2011). *RQI* is given by

$$RQI = I_{RS} \times I_{clay} \times \phi\,, \tag{4.1}$$

where ϕ is the estimated porosity. I can either use total or interconnected porosity in this equation. However, interconnected porosity is preferred to be used in carbonate formations. I_{clay} and I_{RS} in **Eq. 4.1** are given by

$$I_{clay} = \frac{1}{1 + C_{clay}} \tag{4.2}$$

and

$$I_{RS} = \log\left(R_{Deep}\right) - \log\left(R_{Shallow}\right), \tag{4.3}$$

where C_{clay} is the volumetric concentration of clay, R_{Deep} is deep resistivity, $R_{Shallow}$ is shallow resistivity, I_{RS} is resistivity separation index, and I_{clay} is clay concentration index. For I_{RS} assessment, I first corrected the deep resistivity measurements for the effect of initial fluids in the formation by fluid substitution using Archie's equation. The shallow resistivity was assumed to be completely affected by water based mud-filtrate invaded the near-wellbore region. To correct the deep resistivity, I applied Archie's equation to the entire depth interval and substituted hydrocarbon with water in the calculated resistivity. I used the well-log-based estimates of porosity and the assumed electrical properties listed in **Table 4.1** to calculate the corrected deep resistivity. This approach is an approximation to account for fluid substitution and is valid only if the impact of mud-filtrate invasion on the deep resistivity log is negligible.

Parameters	Value
Archie's Winsauer factor, *a*	1
Archie's porosity exponent, *m*	1.96
Archie's saturation exponent, *n*	1.83
Formation water resistivity @ 96 ^{o}F (ohm-m)	0.04
Formation water salt concentration (ppm)	170,000
Mud-filtrate resistivity @ 96 ^{o}F (ohm-m)	0.84
Mud-filtrate salt concentration (ppm)	5147
Shale porosity	0.10

Table 4.1—Hugoton field example: the assumed formation properties used in well-log interpretation.

Furthermore, *RFQI* takes into account the impact of initial fluids in the formation which can be used for completion/production planning. *RFQI* is given by

$$RFQI = I_{RS} \times I_{clay} \times \phi \times \log\left(R_{Deep}\right), \tag{4.4}$$

In the cases of oil-based and fresh water-based mud-filtrate invasion in hydrocarbon-bearing zones, where there is no measureable separation between resistivity logs with multiple radial lengths of investigation, I_{RS} index is not applicable for identifying different rock classes. The introduced analytical factors work the best in the presence of saline water-based mud. I assumed that invasion parameters including time of mud-filtrate invasion remained constant for all the considered depth intervals in this study. This assumption was appropriate for the field examples, as the reservoir depth interval is relatively small. If invasion parameters vary at different depths, numerical simulation of mud-filtrate invasion based on daily reports would be required for reliable quantification of the impact of static and dynamic petrophysical properties on well logs. Consequently, the two indices introduced in this chapter are only reliable if (a) the impact of mud-filtrate invasion is measureable on electrical resistivity logs with different radial lengths of investigation and (b) invasion parameters including overbalance pressure, mud properties, and time of invasion are not considerably variable at different depths.

4.2.3 Rock Classification Using Artificial Neural Network

I applied both supervised and unsupervised artificial neural network algorithms for rock classification (Saneifar et al. 2014b). The supervised artificial neural network (NN) was first trained with an available input dataset representative of the formation's petrophysical characteristics and corresponding pre-defined output rock classes. The rock classes were determined based on the lithofacies description and the core-based Leverett *J*-function rock (Leverett 1941) typing technique in the core domain. The input training set included conventional well logs such as acoustic, PEF, GR, shallow and deep electrical resistivity, bulk density, and neutron porosity logs, as well as mineralogy, core permeability, and core porosity measurements. I used Levenberg-Marquardt, a back-propagation function, to establish the relations between input data and pre-defined rock classes (Levenberg 1944). I calibrated the supervised artificial network to minimize the error in rock classification, by conducting blind tests on the training dataset. I then applied the supervised neural network to identify rock classes in the uncored depth intervals.

The unsupervised neural network used for rock classification was based on the Ward's Hierarchical clustering algorithm (Ward 1963; Guha et al. 1998). Inputs to the unsupervised neural network included well logs and/or well-log-based estimates of petrophysical properties, as well as the total number of classes desired. The classification was represented by the Self-Organizing Map (SOM), also known as Kohonen map (Kohonen 2001). The network agglomerates clusters of input data by minimizing the intra-class variance and takes iterative steps to organize similar input data and assigning them to particular nodes on the SOM map. Unlike the supervised artificial neural network, the unsupervised network does not require training with pre-determined rock classes (Gottlib-Zeh 2000). Geostatistical analysis is then performed to extract the underlying formation heterogeneity.

4.2.4 Geostatistical Analysis

Quantifying formation spatial heterogeneity significantly enhances reservoir characterization and attributes that have important control on acid fracture conductivity. Variogram analysis is commonly applied for spatial heterogeneity assessment of the formation petrophysical properties, as well as lithofacies variation (Gringarten and Deutsch 1999). The main purpose of a variogram analysis is determination of the correlation length of a variable. Correlation length corresponds to the spatial self-similarity of a variable (e.g., permeability) in a certain direction

(Isaaks and Srivastava 1989). I conducted variogram analysis using estimated petrophysical, compositional properties, and well logs to determine the correlation length of these variables along the wellbore. **Fig. 4.2** shows a typical variogram plot used to identify correlation length, designated by λ.

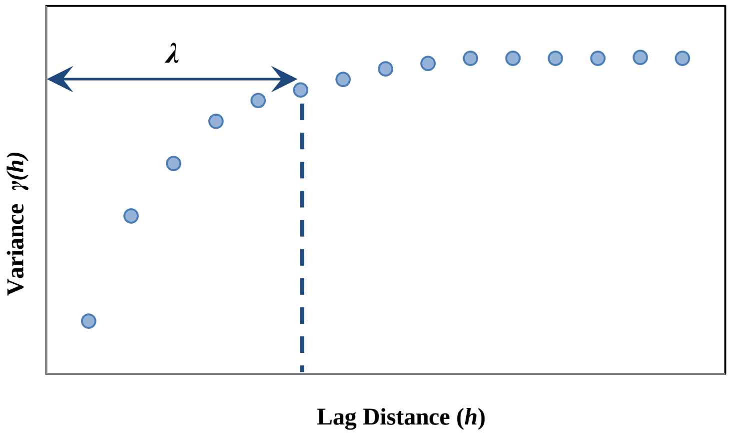

Fig. 4.2—A typical variogram plot, used to identify the correlation length of a variable (λ). Correlation length corresponds to the spatial self-similarity of a variable (e.g., permeability) in a certain direction.

Variance is calculated for the data pairs separated at a given lag distance by

$$\gamma(h) = \frac{1}{2N}\sum_{i=1}^{N}(z_i - z_{i+h})^2 , \tag{4.5}$$

where $\gamma(h)$ is the estimated variance of variable z, h is the lag distance at which variance is calculated for evenly-spaced data points, N is the number of data pairs separated by a distance h, z_i and z_{i+h} are individual data points, separated a distance h from each other. Variograms of petrophysical properties typically express a geometric anisotropy behavior, which corresponds to an increase in the variance with the lag distance. The distance at which the variance levels off and no longer varies with the increase in distance is known as the correlation length. In this work, I used Stanford Geostatistical Modeling Software (SGeMS) to plot and analyze the variograms (Remy et al. 2008).

4.2.5 Principle Component Analysis

An alternative to the application of well-log-based permeability estimates for characterization of formation spatial heterogeneity is direct application of well logs. I applied Principle Component Analysis (PCA) to assimilate different well logs and well-log-based estimated properties without significant loss of variability in the dataset. I then used the first Principle Component (PC1) that contains most of the variability of the dataset for variogram analysis (Guide to Statistics 2000). I normalized well logs by subtracting the mean from each well-log reading and then dividing by the standard deviation. Well logs were transformed to Principle Components (PC) using the eigenvectors of the covariance matrix. Covariance of a matrix with two variables, *x* and *y*, is defined as

$$C = \operatorname{cov}(x, y) = \frac{\sum_{i=1}^{N}(x_i - \bar{x})(\mathrm{y}_i - \bar{y})}{\left[\sum_{i=1}^{N}(x_i - \bar{x})^2 \sum_{i=1}^{N}(y_i - \bar{y})^2\right]^{\frac{1}{2}}}, \qquad (4.6)$$

where C is the covariance matrix, x_i and y_i are depth-by-depth measurements/estimated properties from well logs, $\bar{x}$ and $\bar{y}$ are the mean values of x and y variables, respectively. I applied spectral decomposition to identify the eigenvalues and eigenvectors of the covariance matrix such that

$$C = V^T V \Lambda \, , \tag{4.7}$$

where Λ is the matrix of eigenvalues, V is the eigenvector matrix, and V^T indicates the transpose of eigenvector matrix. The eigenvector with the highest eigenvalue provides the PC with the highest contribution to the total variability in the dataset. PCs are ranked in the order of their contribution to the variability in the dataset.

4.2.6 Quantifying the Impact of Formation Spatial Heterogeneity on Acid Fracture Conductivity

I applied a newly developed acid fracture conductivity correlation (Deng et al. 2012) to investigate the impact of formation spatial heterogeneity on the overall acid fracture conductivity under closure stress. The correlation relates the overall acid fracture conductivity to the horizontal and the vertical correlation lengths of permeability, which are assumed to be representatives of the formation spatial heterogeneity. This correlation was developed on the basis of numerical experiments conducted using a previously-developed acid-fracture simulator (Deng et al. 2012). The correlation of conductivity at zero closure stress, in the case that permeability distribution has a dominant impact on fracture conductivity, is given by

$$\left(wk_f\right)_0 = 4.48\times10^9\,\bar{w}^3\left[1+\left(a_1 erf\left(a_2\left(\lambda_{D,x}-a_3\right)\right)-a_4 erf\left(a_5\left(\lambda_{D,z}-a_6\right)\right)\right)\sqrt{\left(e^{\sigma_D}-1\right)}\right],$$

$a_1 = 1.82 \quad a_2 = 3.25 \quad a_3 = 0.12$ (4.8)

$a_4 = 1.31 \quad a_5 = 6.71 \quad a_6 = 0.03$

where $(wk_f)_0$ is the conductivity at zero closure stress in md-ft, $\bar{w}$ is the average fracture width at zero closure stress, $\lambda_{D,x}$ and $\lambda_{D,z}$ are the dimensionless correlation lengths along the horizontal calculation domain length, L, and the vertical calculation domain length, H, (calculation domain size is 10 ft ×10 ft) respectively, and σ_D is the dimensionless standard deviation of permeability. $\lambda_{D,x}$ and $\lambda_{D,z}$ are given by

$$\lambda_{D,x} = \frac{\lambda_x}{L} \tag{4.9}$$

and

$$\lambda_{D,z} = \frac{\lambda_z}{H}\,. \tag{4.10}$$

$\bar{w}$ can be estimated via

$$\bar{w} = 0.56 erf\left(0.8\sigma_D\right) w_i^{0.83}, \tag{4.11}$$

where w_i is the ideal fracture width in inches, defined as dissolved rock volume divided by fracture surface area. Furthermore, σ_D can be obtained via

$$\sigma_D = \frac{\sigma\left(\ln\left(k\right)\right)}{\ln\left(\bar{k}\right)}, \tag{4.12}$$

where $\bar{k}$ is the average permeability.

Finally, the overall acid fracture conductivity at closure stress, σ_c, is obtained via

$$wk_f = \alpha \exp\left[-\beta \sigma_c\right], \tag{4.13}$$

where

$$\alpha = \left(wk_f\right)_0 \left[0.22\left(\lambda_{D,x}\sigma_D\right)^{2.8} + 0.01\left(\left(1-\lambda_{D,z}\right)\sigma_D\right)^{0.4}\right]^{0.52} \tag{4.14}$$

and

$$\beta = \left[15.6 - 4.5\ln\left(\sigma_D\right) - 7.8\ln\left(E\right)\right]\times 10^{-4} \tag{4.15}$$

4.3 Sensitivity Analysis: Impact of Vertical Correlation Length on Acid Fracture Conductivity

I used three synthetic cases with different vertical correlation lengths of permeability to conduct a sensitivity analysis on the impact of vertical correlation length of permeability on the overall acid fracture conductivity at variable closure stress using the correlation described in **Eqs. 4.8–4.15**. **Table 4.2** lists the parameters used for these three synthetic cases. I used low, medium, and high values of vertical correlation length for synthetic cases 1, 2, 3, respectively, and kept all the other parameters constant in the three synthetic cases. **Fig. 4.3** shows the overall calculated fracture conductivities at closure stresses of 0 – 6000 psi for the three examples. A reduction in the vertical correlation length of permeability, corresponding to a more heterogeneous distribution of permeability in the vertical direction, results in higher fracture conductivity. The calculated fracture conductivity increases by approximately 26% and 45%, when the dimensionless vertical correlation length is decreased from 0.7 to 0.12 and from 0.7 to 0.0156, respectively. This significant increase in the fracture conductivity confirms the importance of determining and incorporating the vertical correlation length in the prediction of acid fracture conductivity. The upcoming sections include the application of the introduced well-log-based method for reliable assessment of vertical heterogeneity of formation properties.

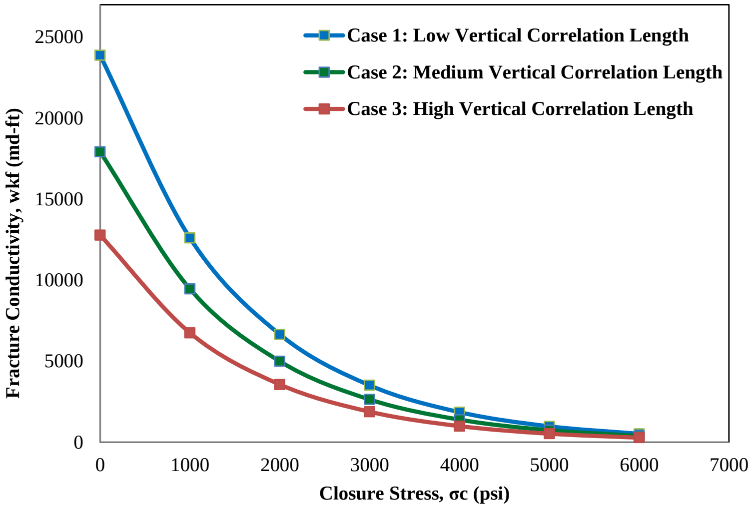

Fig. 4.3—Sensitivity Analysis: calculated fracture conductivity for three synthetic case studies with different vertical correlation lengths of permeability, at closure stresses of 0 – 6000 psi. A reduction in the vertical correlation length of permeability, corresponding to a more heterogeneous distribution of permeability in the vertical direction, results in higher fracture conductivity. The calculated fracture conductivity increases by approximately 26% and 45%, when the dimensionless vertical correlation length is decreased from 0.7 (Case 3) to 0.12 (Case 2) and from 0.7 (Case 3) to 0.0156 (Case 1), respectively.

Parameters	Synthetic Case 1	Synthetic Case	Synthetic Case 3
w_i (in)	0.04	0.04	0.04
$f_{calcite}$ (%)	35	35	35
$\lambda_{D,x}$	0.7	0.7	0.7
$\lambda_{D,z}$	0.0156	0.12	0.7
σ_D	0.7	0.7	0.7
E (Mpsi)	4	4	4

Table 4.2—Sensitivity Analysis: parameters used to investigate the impact of formation spatial heterogeneity on fracture conductivity.

4.4 Field Example No. 1: Hugoton Gas Field

The 70-year old Hugoton field, the largest gas field in North America, is located in southwestern Kansas. This field has yielded over 23 TCF gas production from the lower Permian, upper Wolfcampian Chase group (Olson et al. 1997). The Chase Group is approximately 350 ft thick and includes carbonate, sandstone, and siliciclastic mudstone units (Dubois et al. 2006). Porosity in this reservoir ranges from 10 to 30%; permeability varies from less than 0.1 millidarcy (md) to over 800 md (Olson 1998). Kansas Geological Survey (KGS) identified 11 lithofacies in the Hugoton field, from a study on depositional sequences, rock texture and principal pore size (Dubois et al. 2006). In this field example, limited data are available to identify the shapes of different rock components in each geological facies for the assessment of elastic properties and interparticle and intraparticle porosity using SCA theories. However, the clear trend of mud-filtrate invasion on resistivity well logs can be used for qualitative incorporation of dynamic petrophysical properties in rock classification. Furthermore, extensive core data are available for core-based rock classification. Based on this data scenario, I applied the following rock classification techniques in a well in the Hugoton gas field: (a) conventional core-based Leverett *J*-function (Leverett 1941), (b) analytical rock quality and rock-fluid quality indices, (c) supervised artificial neural network, and (d) unsupervised artificial neural network. I then estimated permeability in each rock class, separately.

I first interpreted conventional well logs to estimate porosity, water saturation, and volumetric concentrations of minerals. There was no required depth-shifting for well logs or core data in this well. Table 4.1 lists the parameters used for the well-log interpretation. Clay type is assumed to be illite. Dominant non-clay minerals in this formation consist of calcite, dolomite, and quartz. Formation fluids include saline formation water and gas. The formation was invaded by fresh water-based mud.

After initial well-log interpretation, I estimated permeability using the conventional core-based porosity-permeability correlation for the entire depth interval shown in **Fig. 4.4**. I identified five rock classes based on lithofacies description and the core-based Leverett *J*-function rock typing technique. Fig. 4.4 illustrates (a) the conventional well logs used in well-log interpretation including GR, PEF, electrical resistivity, bulk density, and neutron porosity, (b) the estimated petrophysical/compositional properties, and (c) the rock classes identified using the core-based Leverett *J*-function rock typing technique and lithofacies description. Estimated petrophysical/compositional properties include volumetric concentrations of minerals, porosity, permeability, and water saturation. Porosity is over-estimated in rock class 2. That can be as the result of an additional mineral present at that depth interval, which is not included in multi-mineral analysis. Mineralogy from core measurements can further improve the model and estimates for petrophysical properties. However, the results show that rock classification based on the well-log-based estimated properties (e.g., porosity) is consistent with the outcome of the core-based rock typing and is not affected by the error associated with the estimates of porosity in rock class 2. Furthermore, the estimates of water saturation do not agree with core measurements of water saturation. This difference is mainly associated with the significant uncertainty in the core measurements of water saturation as water-based drilling mud has invaded the near-wellbore region in this formation. The estimates of permeability using the conventional core porosity-permeability correlation are subjected to a significant error compared to core permeability measurements. These results further emphasize the need for a reliable method to improve permeability assessment. The identified rock classes using the core-based Leverett *J*-function method, shown in Fig. 4.4, are in agreement with the description of the lithofacies documented by Dubois et al. (2006). Rock class 1 corresponds to the worst rock class or silty mudstone and rock class 5 corresponds to the best rock class. These rock classes which are based on core measurements as well as lithofacies descriptions were used as the ground truth for cross-validation of the proposed rock classification techniques.

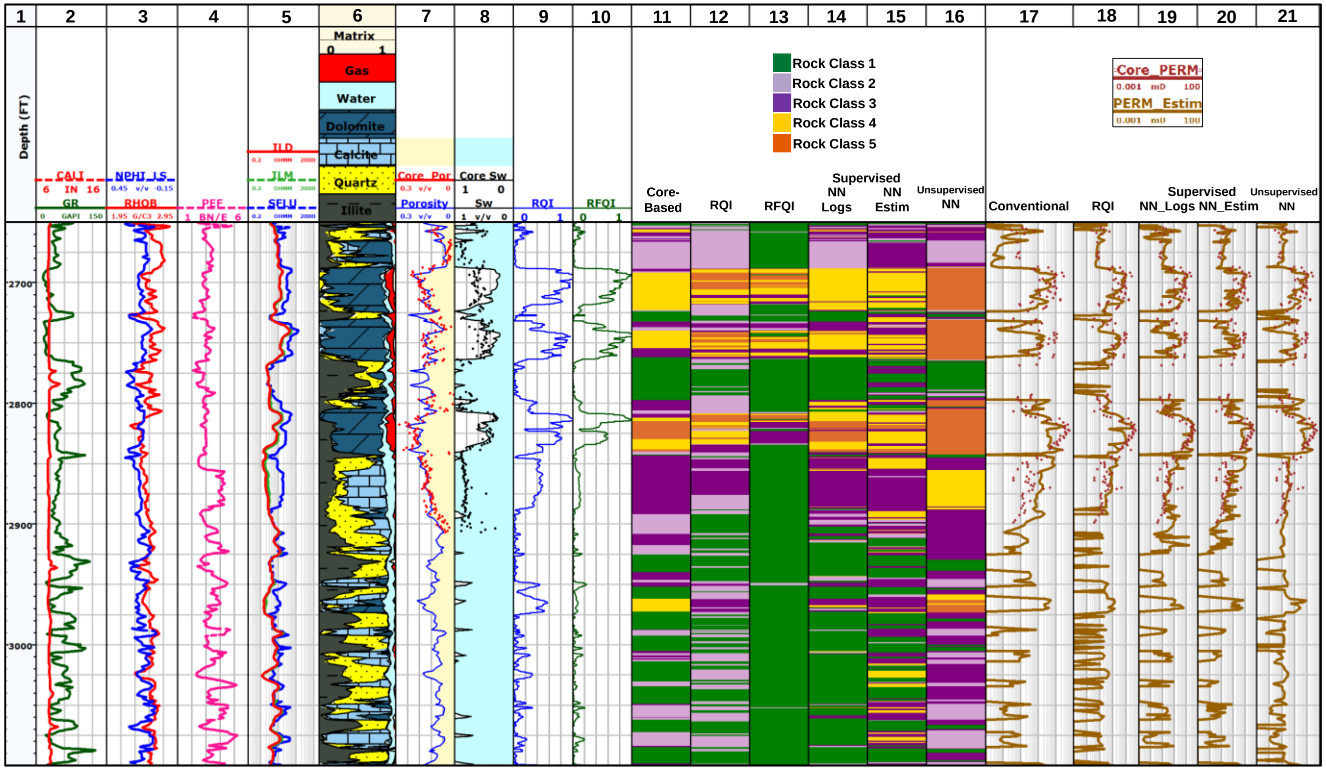

Fig. 4.4—Field Example No. 1, Hugoton Gas Field: conventional well logs and the estimated petrophysical/compositional properties. Tracks from left to right include, Track 1: depth; Tracks 2-5: GR, caliper, neutron porosity (in water-filled limestone units), bulk density, PEF, and apparent resistivity logs; Track 6: estimates of volumetric concentrations of dolomite, calcite, quartz and illite (clay); Tracks 7-8: total porosity and water saturation overlaid with the corresponding core measurements; Tracks 9-10: normalized *RQI* log and normalized *RFQI* log; Tracks 11-13: core-derived rock classes, *RQI*-based rock classes, and *RFQI*-based rock classes; Tracks 14-15: rock classes obtained using two cases of supervised neural network, with well logs and with estimated properties; Track 16: rock classes obtained from unsupervised neural network; (Tracks 11-16: green represents mudstone or the worst rock class and orange corresponds to the best rock class) Track 17: estimated permeability from core porosity-permeability correlation, overlaid with core measurements of permeability; Track 18: permeability estimates using *RQI*-based rock classification, overlaid with core measurements of permeability; Tracks 19-20: permeability estimates from rock classification using two cases of supervised neural network, with well-logs and estimated properties, overlaid with core measurements of permeability; Track 21: permeability estimates from rock typing using unsupervised neural network, overlaid with core measurements of permeability.

Next, I used *RQI* to identify rock classes. The separation of shallow and corrected deep resistivity was applied for *RQI* assessment. *RQI* log was used to classify rocks into five rock classes (Fig. 4.4). I also calculated *RFQI* which takes into account the type and the saturation of desired fluids in the reservoir. This index can be directly used for selecting candidates for acid fracturing as it takes into account reservoir fluids as well as static and dynamic rock properties.

I then identified rock classes using supervised artificial neural network following two approaches. The first approach adopted only well logs as inputs to the network. The input well logs included I_{RS}, GR, bulk density, neutron porosity, and PEF. The network was trained by more than 1000 iterations, where core measurements and lithofacies description were available. The output of the network was rock classes.

The training and input datasets in the second approach included estimates of petrophysical/compositional properties obtained from well logs including porosity, permeability, and volumetric concentrations of calcite, dolomite, quartz, and clay. The training dataset also contained core measurements of porosity and permeability. First iteration of permeability estimates for the rock typing techniques was obtained using core-derived porosity-permeability correlation. These permeability estimates were updated in every iteration.

Next, I identified rock classes in this field example using an unsupervised artificial neural network. This approach was not dependent on any core measurements or pre-defined rock classes. The inputs to the unsupervised rock classification approach included I_{RS}, volumetric concentrations of calcite, dolomite, quartz, clay, and estimated porosity. Fig. 4.4 shows the results for rock typing using supervised and unsupervised artificial neural networks.

Finally, I estimated depth-by-depth permeability in each rock class. Fig. 4.4 compares estimated permeability values based on different rock typing techniques against core measurements and **Fig. 4.5** shows cross-plots of permeability estimates and core permeability measurements for all the techniques employed in this study and the corresponding relative errors in permeability estimates. The rock classification based on supervised artificial neural network provides the most accurate rock classification and permeability assessment among all the applied methods when compared against core measurements. In the case of supervised artificial neural network approach, inputting well logs to the network provides a more accurate rock classification and permeability assessment compared to the application of petrophysical/compositional estimated properties as input parameters. Among the methods with minimal dependence on core measurements (i.e., *RQI* and unsupervised artificial neural network) the rock classification using *RQI* provides the most reliable rock classes. Fig. 4.5 shows that the analytical rock classification (*RQI*) provides an improvement of approximately 50% in permeability assessment. Although the difference in errors of permeability assessment from *RQI* and supervised artificial neural network using an input of well logs is small, supervised artificial neural network requires training and calibration using core measurements, whereas *RQI* can be obtained real-time.

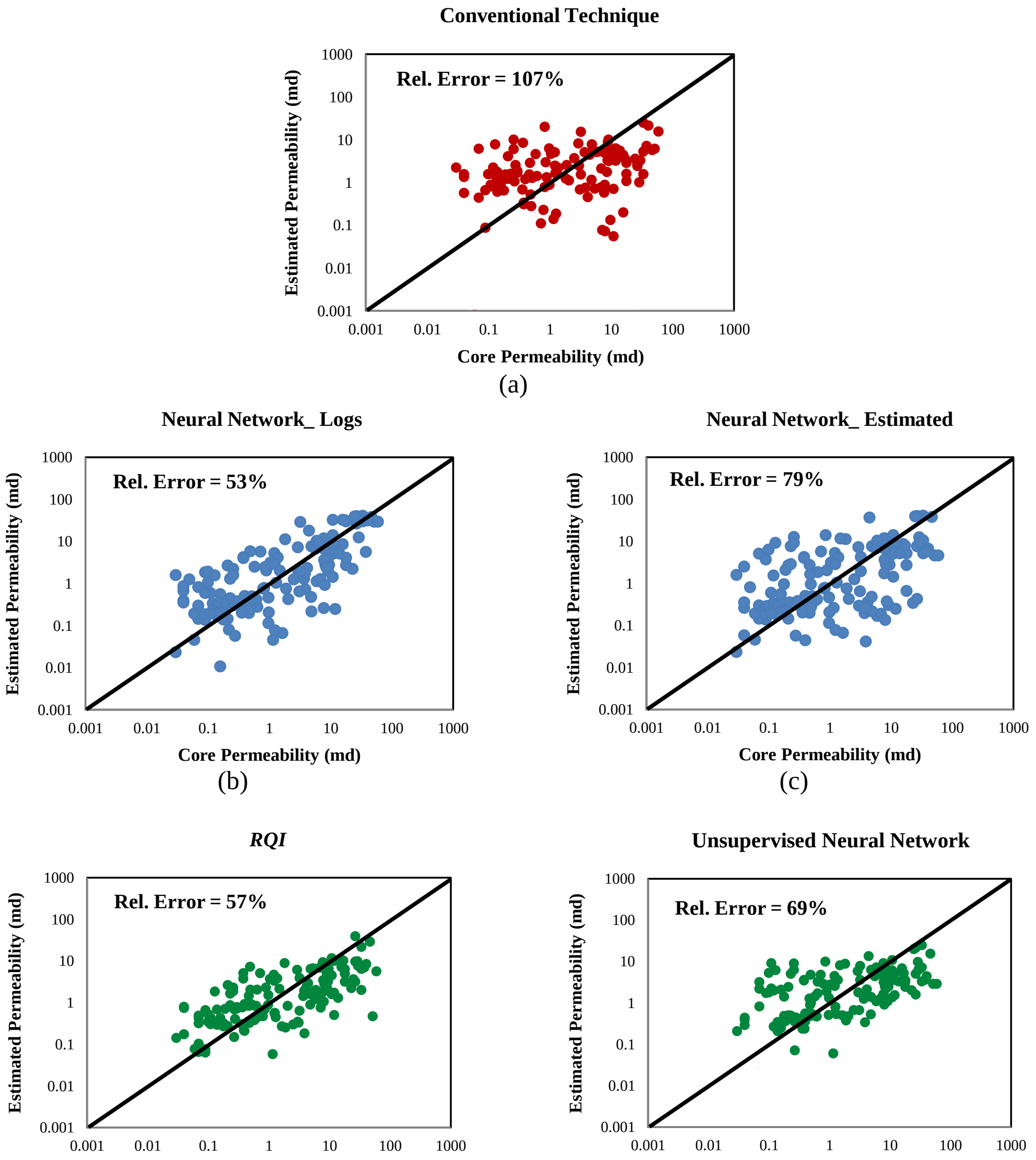

(a)

(b)

(c)

(d)

(e)

Fig. 4.5—Field Example No. 1, Hugoton Gas Field: cross-plots of core permeability measurements and well-log-based permeability estimates obtained from (a) conventional permeability assessment technique, (b) supervised neural network with well logs as inputs to the network, and (c) supervised neural network with well-log-based estimated petrophysical.

Furthermore, the presence of I_{RS} has a significant impact on reliable rock classification in both supervised and unsupervised artificial neural network approaches. The presence of core measurements can, however, further improve assessment of rock classification in all the aforementioned techniques.

4.4.1 Characterization of Formation Spatial Heterogeneity Used for Prediction of Acid Fracture Conductivity

Previous publications (Mou et al. 2011; Deng et al. 2011; Oeth et al. 2013) documented a recently developed acid fracture model that applies permeability correlation length to take into account formation spatial heterogeneity in prediction of fracture conductivity. Permeability correlation length is assigned to each calculation domain of size 10 ft by 10 ft, in horizontal and vertical directions. In this section, I first show an example to illustrate the significance of the application of well-log-based permeability estimates for variogram analysis. I then present variogram analysis to obtain the vertical correlation length in a hydrocarbon-bearing zone, with the best rock quality, using (a) well-log-based permeability estimates, (b) well logs and their first Principle Component, and (c) estimated petrophysical/compositional properties and their first Principle Component.

Fig. 4.6 shows variograms constructed using (a) core permeability measurements and (b) the best well-log-based estimates of permeability, in the Hugoton field example, in the depth interval of 2692–2705 ft. I observe that minimum variance of core permeability measurements starts at a value larger than zero variance. This local discontinuity is known as the "nugget effect".

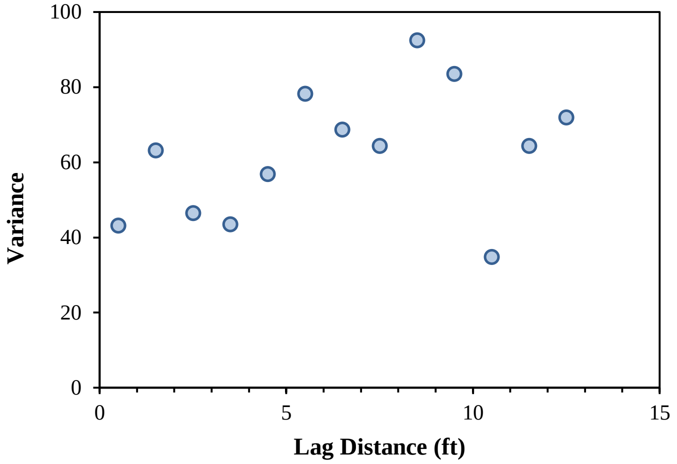

(a)

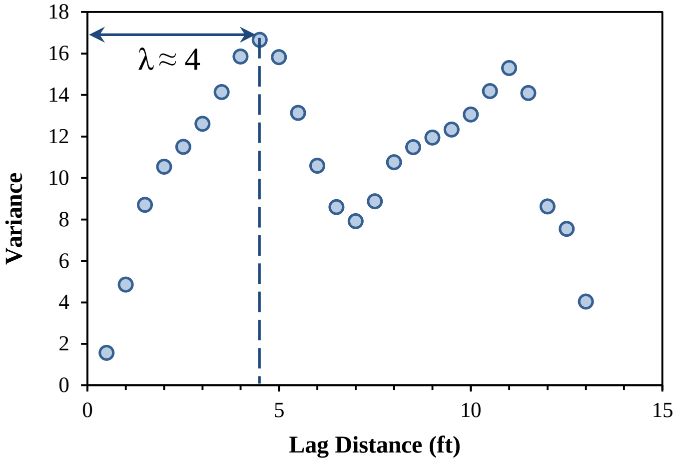

(b)

Fig. 4.6—Field Example No. 1, Hugoton Gas Field: comparison of permeability variograms for (a) core permeability measurements and (b) well-log-based permeability estimates in the depth interval of 2692–2705 ft. The significant nugget effect observed in the variogram of core permeability measurements corresponds to the possible measurement error, as well as data sampling at a relatively large scale.

The significant nugget effect observed in the variogram of core permeability measurements corresponds to the possible measurement error, as well as data sampling at a relatively large scale (Fig. 4.6). The results confirm that the variogram of core permeability measurements is not reliable for identifying the correlation length of permeability, as the core data are limited (Fig. 4.6). On the other hand, variogram of well-log-based permeability estimates has a negligible nugget effect and can reliably provide the correlation length (approximately 4 ft). Therefore, well-log-based estimates of permeability that are validated using core measurements can be applied to characterize formation spatial heterogeneity.

To further investigate the application of well logs for characterizing formation spatial heterogeneity, I selected the hydrocarbon-bearing depth interval of 2692–2723 ft, corresponding to the best rock class and conducted variogram analysis. **Fig. 4.7** shows the variogram obtained using well-log-based permeability estimates. I applied the spherical variogram model and estimated correlation length of approximately 4 ft (Fig. 4.7). The first structure displayed on the variogram plot was used to determine the correlation length, as the first few variogram points are known to be more reliable for model-fitting and determination of the correlation length (Beatty 2010).

Next, I investigated the direct application of well logs, as an alternative to well-log-based permeability estimates for characterizing the spatial heterogeneity. Direct application of well logs can be an appropriate substitute for the application of well-log-based permeability estimates in variogram analysis, where (a) there is not enough core data available for calibration purposes and (b) the correlation between core-derived porosity and permeability is poor. Additionally, application of core-base porosity-permeability correlation for the assessment of permeability in each rock class results in diminished resolution, as the consequence of smoothing the available data. Direct application of well logs in lieu of permeability estimates can prevent the additional smoothing involved in permeability assessment.

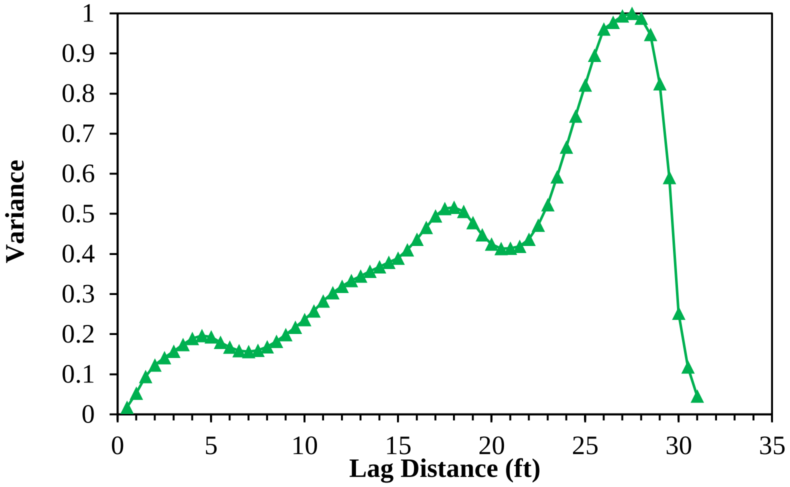

Fig. 4.7—Field Example No. 1, Hugoton Gas Field: variogram analysis using well-log-based estimates of permeability in depth interval of 2692–2723 ft. The correlation length is estimated to be approximately 4 ft.

I used GR, neutron porosity, bulk density, PEF, and I_{RS} in the variogram analysis. GR and PEF logs correspond to volumetric concentration of clay and lithology in the formation, respectively. Bulk density and neutron porosity provide information about formation porosity and lithology. I_{RS} which corresponds to the separation of the resistivity well logs, as the result of fluid invasion into the formation, can be used as a representative of the formation static/dynamic petrophysical properties such as permeability. **Fig. 4.8a** shows the variogram of individual well logs for the selected depth interval. Among the well logs used, GR and I_{RS} are not good representatives of the formation spatial heterogeneity in the selected zone. Their variograms correspond to a larger correlation length compared to the correlation length identified using permeability estimates (Fig. 4.8a). This behavior is expected, as GR only corresponds to the shale content in the formation and apparent resistivity logs have a relatively poor vertical resolution. However, variograms of well logs such as bulk density and PEF provide correlation lengths, similar to that of permeability estimates. As individual well logs might not be indicative of spatial heterogeneity, I used PCA to assimilate all the well logs with no significant loss of variability in the dataset. Principle Component is an alternative form of presenting the data, while retaining the main structure of the dataset. **Fig. 4.8b** shows the variogram constructed using PC1 for the zone under study. The correlation length identified from this variogram is approximately 3 ft, which is smaller than the one obtained from the permeability variogram (Fig. 4.8b).

In addition to the direct application of well logs, I applied estimated porosity and volumetric concentration of minerals to conduct variogram analysis in the zone of interest (i.e., depth interval of 2692–2723 ft). **Fig. 4.9a** shows the variogram of the estimated properties, corresponding to a similar correlation length compared to the correlation length of permeability estimates. I conducted PCA using the estimates of porosity and volumetric concentration of present minerals and analyzed the variogram of

PC1. **Fig. 4.9b** illustrates the variogram constructed using PC1 of the estimated properties. Based on this variogram, the correlation length is estimated to be 3 ft.

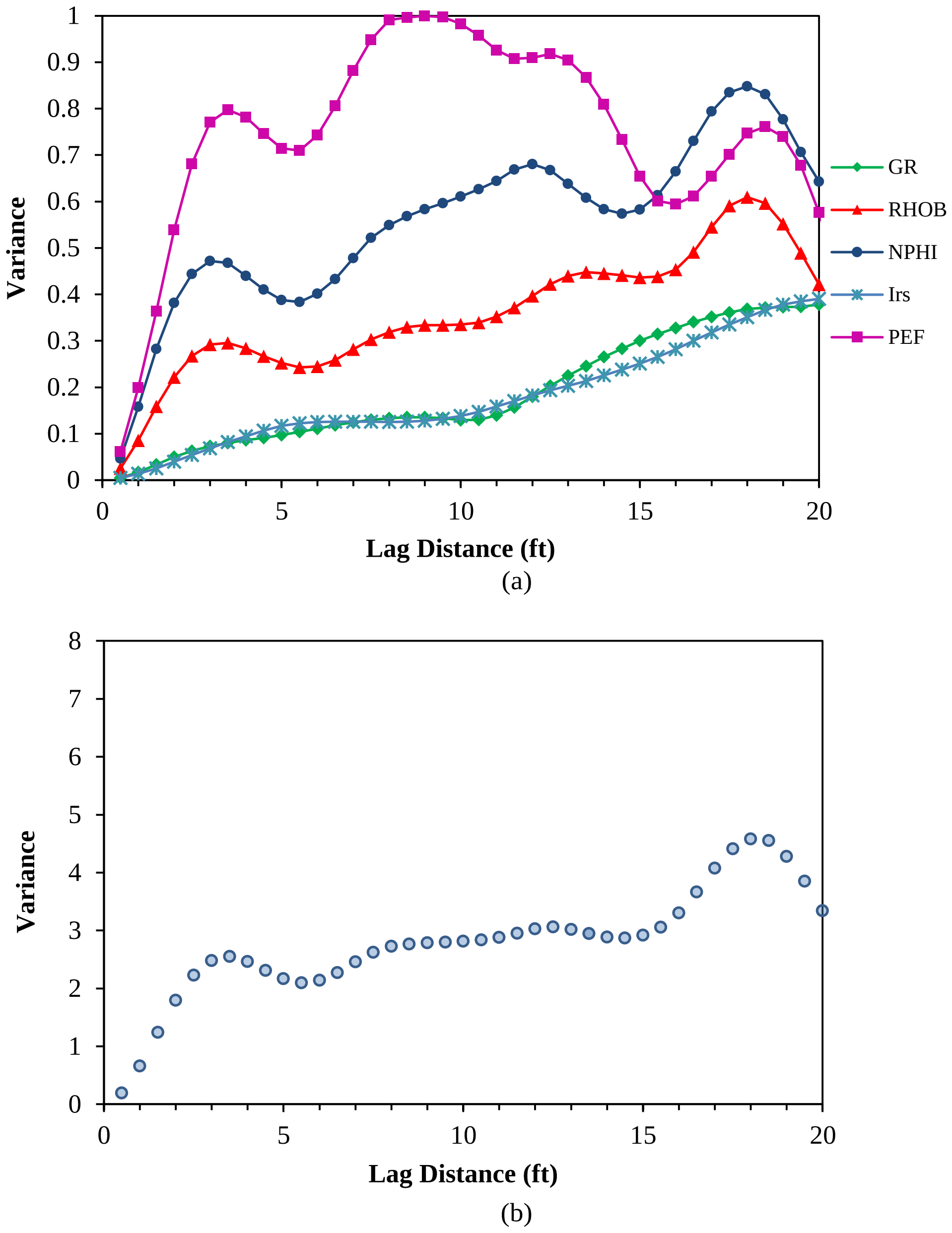

Fig. 4.8—Field Example No. 1, Hugoton Gas Field: variogram analysis for (a) well logs and (b) the first Principle Component of well logs, in the depth interval of 2692–2723 ft. The correlation lengths estimated from the variograms of PEF, neutron porosity, and bulk density measurements, as well as the first Principle Component of the well logs are approximately 3 ft. However, GR and I_{RS} are not indicative of the formation spatial heterogeneity.

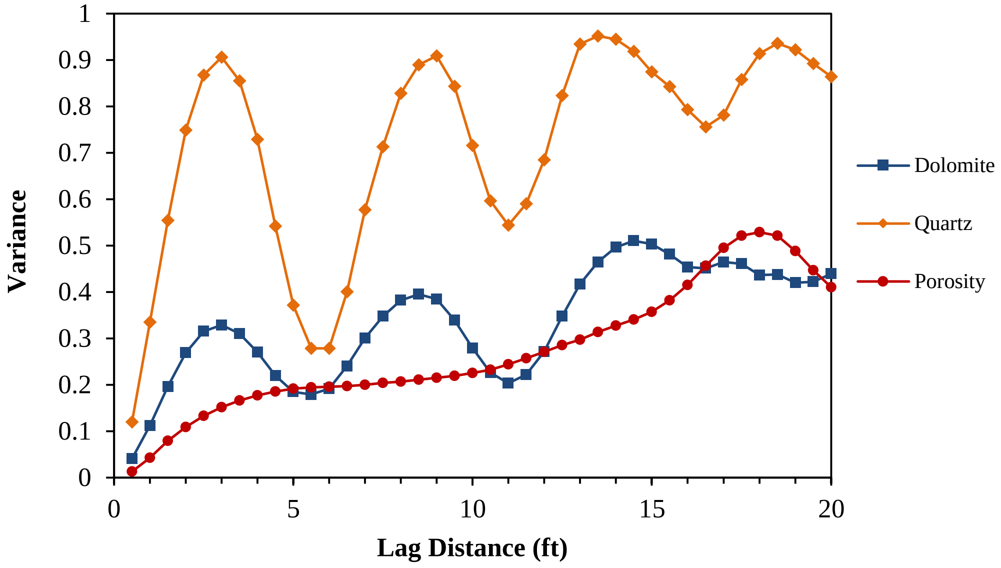

(a)

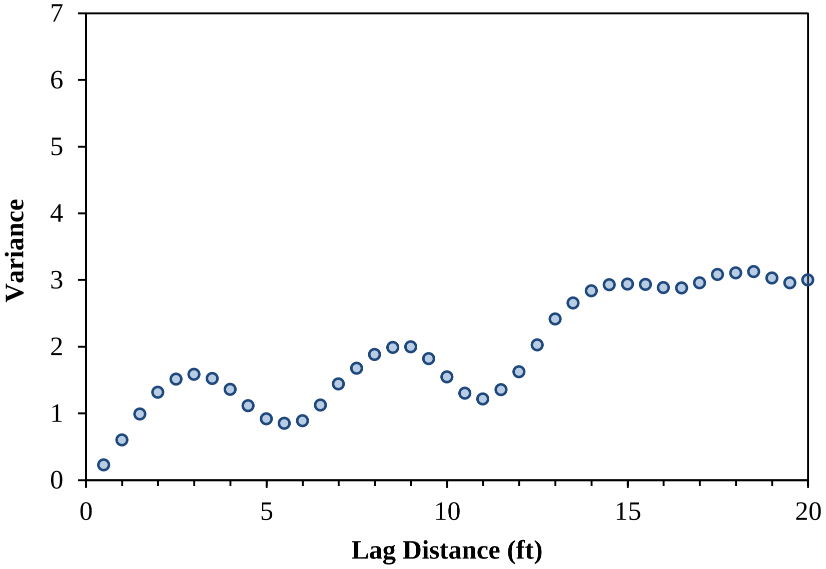

(b)

Fig. 4.9—Field Example No. 1, Hugoton Gas Field: variogram analysis for (a) estimates of volumetric concentrations of minerals and porosity and (b) the first Principle Component calculated for the estimates of volumetric concentrations of minerals and porosity, in the depth interval of 2692–2723 ft. The correlation lengths obtained from the variograms of the estimated volumetric concentrations of minerals and porosity, as well as the first Principle Component are approximately 3 ft.

Variograms constructed based on PC1 of well logs and PC1 of estimated porosity and volumetric concentration of minerals correspond to relatively smaller correlation length, compared to the correlation length estimated from permeability estimates. This is as the result of improved characterization of formation heterogeneity, since there is less data smoothing involved in well logs, estimated porosity, and estimated mineral concentrations, compared to the well-log-based permeability estimates. The results confirm that the PC1 of the well logs and the estimated petrophysical/composition properties can be used to characterize formation spatial heterogeneity, in near wellbore region.

4.5 Field Example No. 2: Happy Spraberry Oil Field

Happy Spraberry field is located on the western edge of the eastern shelf of Permian (Midland) Basin in Garza County, Texas. The 100 ft thick carbonate zone is located in the Lower Clear Fork formation (Gentry 2003). It contains four typical lithofacies that are identified based on constituent composition, depositional texture and sedimentary structures (Hammel 1996; Roy 1998; Layman 2002). Reservoir lithofacies consist of oolitic skeletal grainstone/packstone and skeletal rudstone. Non-reservoir facies include floatstone and shaly siltstone. Oolitic grainstone facies are the highest reservoir quality lithofacies contributing the most to the Happy Spraberry production (Hammel 1996; Roy 1998; Layman 2002).

I first conducted a joint inversion of conventional well logs to estimate interconnected and total porosity, water saturation, and volumetric concentration of minerals. I applied a depth shifting of +1 ft on core measurements. **Table 4.3** lists the parameters used in well-log interpretation, based on previous field studies (Mazingue-Desailly 2004). Formation fluids include saline formation water and oil.

Parameters	Value
Archie's Winsauer factor, *a*	1
Archie's porosity exponent, *m*	2
Archie's saturation exponent, *n*	2
Formation water resistivity @ 110 ºF	0.038
Formation water salt concentration (ppm)	148,500
Mud-filtrate resistivity @ 110 ºF (ohm-m)	0.11
Mud-filtrate salt concentration (ppm)	40,600
Shale porosity	0.08

Table 4.3—Happy Spraberry field example: the assumed formation properties used in well-log interpretation.

Fig. 4.10 shows the conventional well logs used for well-log interpretation and the estimates of porosity, water saturation, and volumetric concentrations of minerals. Interconnected non-shale porosity is estimated by joint-interpretation of well logs, including compressional-wave slowness log. The compressional-wave slowness was corrected for clay and non-clay minerals using the well-log-based estimates of volumetric concentrations of minerals (Backus 1962).

In Field Example No. 2, I could not use either supervised neural network approach or *RQI* method, because (a) core measurements are limited and (b) the impact of mud-filtrate invasion on electrical resistivity logs is not significant outside of the highest permeability zone (X930-X990 ft). Thus, I used the unsupervised neural network technique.

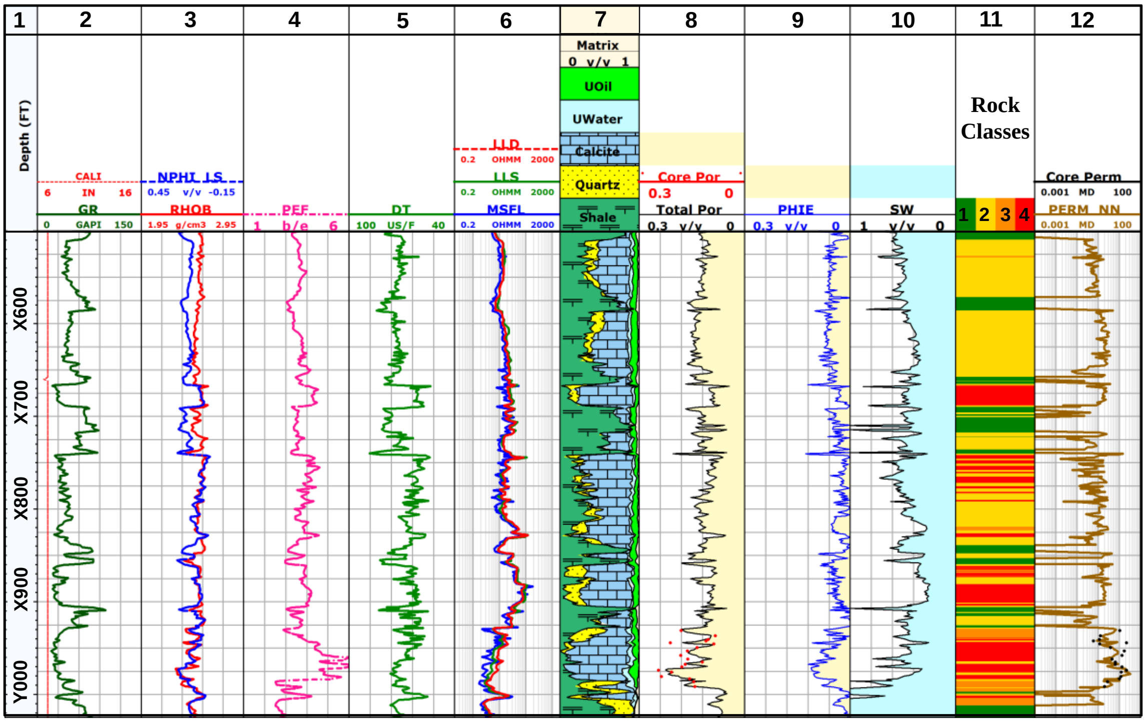

Fig. 4.10—Field Example No. 2, Happy Spraberry Oil Field: conventional well logs and the estimated petrophysical/compositional properties. Tracks from left to right include, Track 1: depth; Tracks 2-6: GR, caliper, neutron porosity (in water-filled limestone units), bulk density, PEF, compressional-wave slowness, and apparent resistivity logs; Track 7: estimates of volumetric concentrations of calcite, quartz and shale; Tracks 8-10: total porosity, interconnected porosity, and water saturation estimates overlaid with the corresponding core measurements; Track 11: rock classes identified using unsupervised artificial neural network (rock class 1 is the worst rock type and rock class 4 is the best); Track 12: final permeability assessment compared to core permeability measurements.

The initial inputs to the unsupervised artificial neural network include well-log-based estimates of interconnected porosity and volumetric concentrations of shale, quartz and calcite. Permeability is then estimated using core porosity-permeability correlations in different rock classes, observed in the field. In the second iteration, estimated permeability is also added to input logs for rock classification process.

The identified rock classes are in agreement with the described lithofacies in the field (Layman 2002). Fig. 4.10 shows the identified rock classes and permeability estimates. Rock class 1 corresponds to the worst rock type class or silty mudstone and rock class 4 is the best rock type. Permeability estimates are consistent with core measurements in the depth interval of X900-Y000 ft. However, more core measurements are required to cross-validate the permeability estimates from well logs.

Next, I conducted variogram analysis to characterize formation spatial heterogeneity in the depth interval of X950-X980 ft, corresponding to the best rock class. I applied (a) well-log-based permeability estimates, (b) well logs: GR, neutron porosity, bulk density, PEF, compressional-wave slowness, (c) PC1 of well logs, and (d) PC1 of the well-log-based estimates of porosity and volumetric concentration of minerals as inputs to the variogram analysis. **Fig. 4.11** shows the variogram constructed using permeability estimates. Based on this variogram, the correlation length is 4 ft. Then, I used well logs to conduct PCA. **Figs. 4.12a** and **4.12b** illustrate the variograms obtained from well logs and PC1 of well logs, respectively. The correlation length of PC1 variogram is estimated to be 4 ft, the same as the correlation length identified using permeability estimates. **Figs. 4.13a** and **4.13b** show the variograms of the estimated properties and PC1 of the estimated properties, respectively. The correlation length from variogram of PC1 is estimated to be 3 ft, which is smaller than the identified permeability correlation length. This is as the result of less smoothing involved in the input data, compared to the well-log-based estimates of permeability. The results show that the PC1 of the well logs and the estimated petrophysical/composition properties can be used to characterize formation spatial heterogeneity.

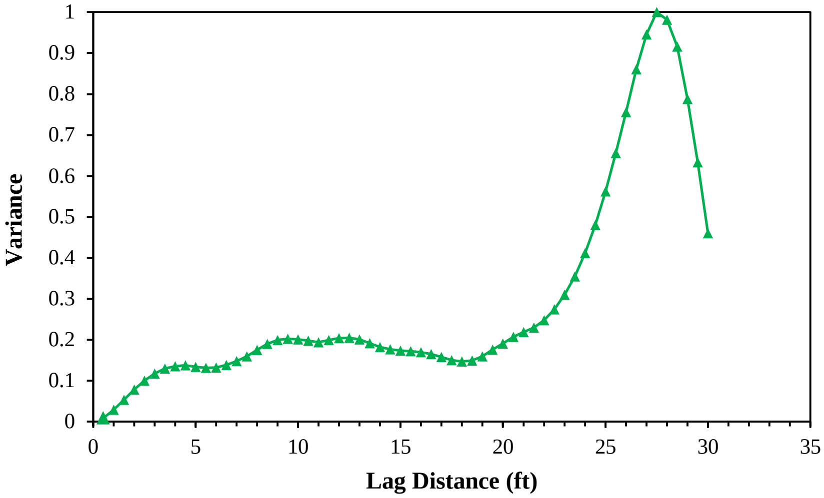

Fig. 4.11—Field Example No. 2, Happy Spraberry Oil Field: variogram analysis using well-log-based permeability estimates, depth interval of X950-X980 ft. The correlation length is estimated to be 4 ft.

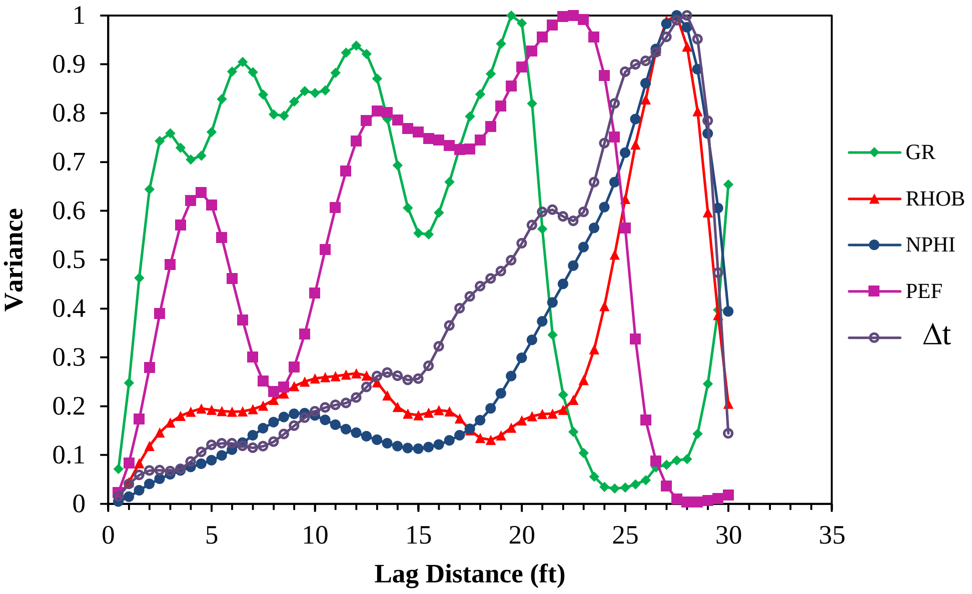

(a)

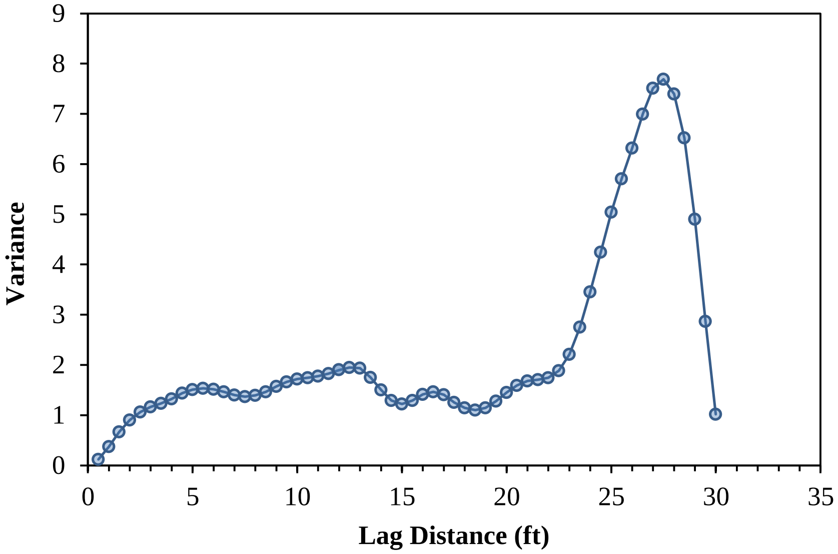

(b)

Fig. 4.12—Field Example No. 2, Happy Spraberry Oil Field: variogram analysis for (a) well logs and (b) first Principle Component of well logs, depth interval of X950-X980 ft. The correlation length estimated from the variogram of the first Principle Component of well logs is estimated to be 4 ft, which is the same as the correlation length obtained using permeability estimates.

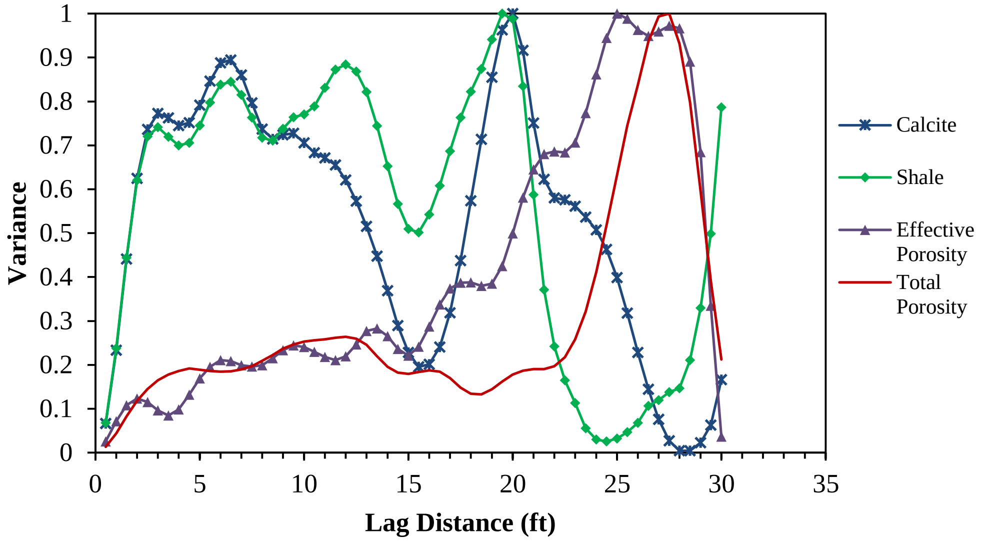

(a)

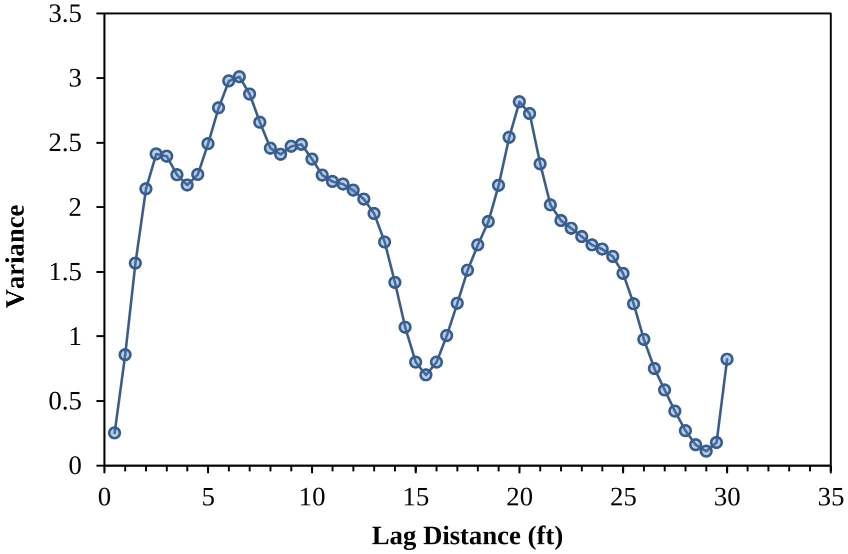

(b)

Fig. 4.13—Field Example No. 2, Happy Spraberry Oil Field: variogram analysis for (a) estimated mineral volumetric concentration and porosity and (b) first Principle Component of estimated mineral volumetric concentration and porosity, depth interval of X950-X980 ft. The correlation length obtained using the variogram of the first Principle Component of the estimated volumetric concentration of minerals and porosity is estimated to be 3 ft, which is smaller than the correlation length obtained using permeability estimates.

4.6 Conclusions

In this chapter, I conducted variogram analysis of conventional well logs and well-log-based estimates of petrophysical and compositional properties to quantify formation spatial heterogeneity in carbonate reservoirs. I proposed a new method which iteratively updates depth-by-depth permeability and rock class assessments using well logs. Permeability is estimated within different rock classes separately in each iteration. For well-log-based rock classification, I introduced three rock classification techniques including (a) a real-time well-log-derived analytical factor, (b) unsupervised artificial neural network, and (c) supervised artificial neural network. The first two techniques are independent of core measurements for rock classification. However, the supervised artificial neural network is highly dependent on the core measurements in the field. This technique involves training using core measurements and quality check of the network, whereas the analytical factor (*RQI*) can be obtained real-time and requires relatively less time for preparation of the input data. All the methods take into account static/dynamic petrophysical properties as well as compositional properties in rock classification. To qualitatively include the impact of dynamic petrophysical properties, I used the separation of the resistivity well logs, corresponding to the water-based mud-filtrate invasion in the hydrocarbon zones. I assumed that invasion parameters including time and rate of mud-filtrate invasion remain constant for all the considered depth intervals in this study. This assumption might cause uncertainty in the rock classification results in larger depth intervals. In such situation drilling reports should be used for interval-by-interval quantification of invasion properties combined with near wellbore fluid-flow simulation.

I successfully applied the introduced techniques for rock classification and permeability assessment in two carbonate field examples including Hugoton gas field and Happy Spraberry oil field. The results obtained for Hugoton gas field suggest that supervised neural network provides the most reliable estimates for rock classification and permeability assessment among all the introduced methods, with 54% improvement in permeability assessment. Direct application of well logs provides a more reliable rock classification compared to the application of estimated petrophysical/compositional properties using well logs.

In the cases with limited core measurements, however, I recommend the application of the introduced analytical rock quality index or unsupervised artificial neural network for rock classification. In the Hugoton gas field, I observed 50% and 38% relative improvements in permeability assessment using analytical rock quality index and unsupervised artificial neural network for rock classification, respectively.

Furthermore, I showed that well-log-based permeability estimates are more reliable compared to core measurements to characterize formation spatial heterogeneity for prediction of acid fracture conductivity. I also conducted a sensitivity analysis to study the impact of vertical correlation length of permeability on the overall acid fracture conductivity at variable closure stress. The calculated fracture conductivity increased by approximately 26% and 45%, when the dimensionless vertical correlation length was decreased from 0.7 to 0.12 and from 0.7 to 0.0156, respectively. The variogram analysis in both field examples showed that well logs as well as well-log-based estimates of petrophysical/compositional properties can be applied in variogram analysis in lieu of well-log-based permeability estimates, in the lack of enough core data for calibration. This work can be further improved by incorporating the accurate volumes of investigation of different logging tools based on their geometrical configuration in the variogram analysis.

CHAPTER V

AN INVESTIGATION ON THE IMPACT OF HETEROGENEITY IN CARBONATE FORMATIONS ON FLUID INJECTIVITY LOSS DURING WATER-ALTERNATING-GAS INJECTION

In this chapter, I investigated and quantified the impact of spatial heterogeneity in a carbonate formation on injectivity loss during Water-Alternating-Gas (WAG) injection. WAG technique is commonly used to improve sweep efficiency of gas injections in depleted oil fields. However, heterogeneous distribution of porosity and permeability in carbonate formations can cause injectivity abnormalities during WAG cycles. These anomalies reduce the effective fluid mobility in all rock types, irrespective of their porosity and permeability. Thus, a larger fraction of gas flows into the layers of higher porosity and permeability, compared to layers with poor petrophysical properties. This can lead to reduced injectivity in the well and loss of WAG operation effectiveness (Rogers and Grigg 2001).

I first conducted automatic rock classification based on conventional well logs, using an unsupervised neural network, to characterize the heterogeneous distribution of petrophysical properties and mineralogy in a carbonate formation. I then applied a new heterogeneity coefficient to quantify the spatial distribution of rock classes. The viability of the introduced heterogeneity coefficient was confirmed using Principle Component and variogram analyses.

The aforementioned technique was applied to ten wells of the SACROC Unit, located in west Texas, in which WAG injection was implemented. Five of the selected wells in this field exhibited no injectivity abnormality, while the other five wells experienced unexpected low gas injectivity during CO_2 injection and an apparent reduction in water injectivity during the follow-up brine injection. I quantified and compared the magnitude of the spatial heterogeneity in the distribution of rock classes for all ten wells.

5.1 Introduction

Water-Alternating-Gas (WAG) injection has been commonly implemented as an enhanced oil recovery (EOR) technique, aiming at improving the sweep efficiency of gas injections. This EOR procedure, first proposed by Caudle and Dyes (1958) includes alternating slugs of water in the gas injection to control the higher mobility of gas as compared to that of the reservoir fluids. The WAG technique integrates the microscopic displacement of the oil by gas, which is normally better than by water, and the improved macroscopic sweep by water injection for enhanced oil displacement (Christensen et al. 2001). Despite the higher sweep efficiency by alternating the gas and water injection in one operation, as opposed to injecting gas and water separately, loss of injectivity during WAG cycles has been an industry concern since the first field tests (Gorell 1990; Rogers and Grigg 2001).

Injectivity abnormalities can result in significant pressure drop in the reservoir, resulting in a lower oil recovery that could unfavorably affect the economic viability of a WAG project. Key factors affecting the injectivity during WAG operations include WAG ratio, injection rate, rock wettability, relative permeability, and formation spatial heterogeneity (Schneider and Owens 1976; Jackson et al. 1985; Huang and Holm 1986; Potter 1987; Roper et al. 1992; Surguchev et al. 1992; Rogers and Grigg 2001). The latter is of particular importance in carbonate formations with lateral and vertical variability of petrophysical properties (e.g., permeability). WAG injection reduces the effective fluid mobility not only in the layers with high permeability, but also in the adjacent layers with lower permeability. Consequently, the higher permeability layers receive a larger fraction of gas, which leads to reduction of frontal advancement in the lower permeability layer and loss of injection (Rogers and Grigg 2001).

Well logs can be used for depth-by-depth assessment of petrophysical and compositional properties and characterization of formation spatial heterogeneity. However, interpretation of well logs in complex carbonate formations is challenging. Rock classification can be applied to improve the well-log-based estimates of petrophysical and compositional properties in heterogeneous carbonate formations and to optimize selection of candidate wells for WAG injection. Although there are several rock-fluid properties that can strongly affect injectivity during WAG operations, this chapter focuses on quantifying the impact of formation spatial heterogeneity on WAG injectivity abnormalities.

I conducted petrophysical rock classification using conventional well logs in ten wells in the SACROC (Scurry Area Canyon Reef Operators Committee) Unit, west Texas, subjected to WAG injection. Five of the selected wells in this field showed no injectivity abnormality, while the other five experienced unexpected low CO_2 injectivity during gas injection, as well as an apparent reduction in water injectivity during the follow-up brine injection. I applied geostatistical analysis to investigate and to quantify the impact of formation spatial heterogeneity on injectivity loss during WAG injection. I introduced a heterogeneity coefficient for characterizing the heterogeneous distribution of the identified petrophysical rock classes. Application of the new heterogeneity coefficient was validated by comparing it against the other common geostatistical approaches for the assessment of spatial heterogeneity.

To the best of my knowledge, there has been no previous research conducted on quantifying the impact of formation spatial heterogeneity on WAG injectivity loss. As formation heterogeneity is among the most influential factors affecting the WAG injectivity, it is important to understand its impact on the injectivity during WAG operations (Schneider and Owens 1976; Jackson et al. 1985; Huang and Holm 1986; Potter 1987; Roper et al. 1992; Surguchev et al. 1992; Rogers and Grigg 2001). The proposed technique can predict the likelihood of success or failure of WAG injection in oil wells prior to investment, thus minimizing the possible economic risk and associated costs.

5.2 WAG Injection in the SACROC Unit

The SACROC Unit, located in Scurry County, west Texas, was discovered in 1948 as the Kelly Snyder field (Brnak et al. 2006). Extending on the northeastern fringe of the Permian Basin, the SACROC Unit is among the largest oil fields onshore in North America, with 2.8 billion barrels of oil in place (Brnak et al. 2006). Early depletion in the Kelly Snyder field, with solution-gas drive as the primary producing mechanism, indicated the necessity of a pressure maintenance program to alleviate extreme loss of reserves (Kane 1979). In 1952, the operators and royalty owners decided to unitize the Kelly Snyder and the Diamond M fields into the SACROC Unit to improve the secondary and tertiary recovery of oil. Water flood was initiated in 1954, followed by the first WAG injection project in 1972 (**Fig. 5.1**). After a peak in production, the unit went on a rapid decline. Several projects were executed to recover from the decline, but there was no considerable success. In 1995, a WAG flood pilot consisting of five-spot patterns was developed for utilizing large injection volumes of CO_2 at miscible conditions. Consequently, the decline in the production was halted. WAG projects in the SACROC Unit have continued to expand, and production subsequently increased to 31 billion barrels (Langston et al. 1988; Brnak et al. 2006).

Despite the enhanced oil recovery, injectivity loss has continued to be a major limiting factor in some WAG operations in the SACROC Unit. Sudden loss of injectivity during CO_2 injection, followed by reduction in water injectivity during brine injection, has led to unsuccessful WAG operations in the SACROC wells. Efforts to mitigate loss of injectivity in the field have been mostly unsuccessful (Schneider and Owens 1976; Harvey et al. 1977; Potter 1987).

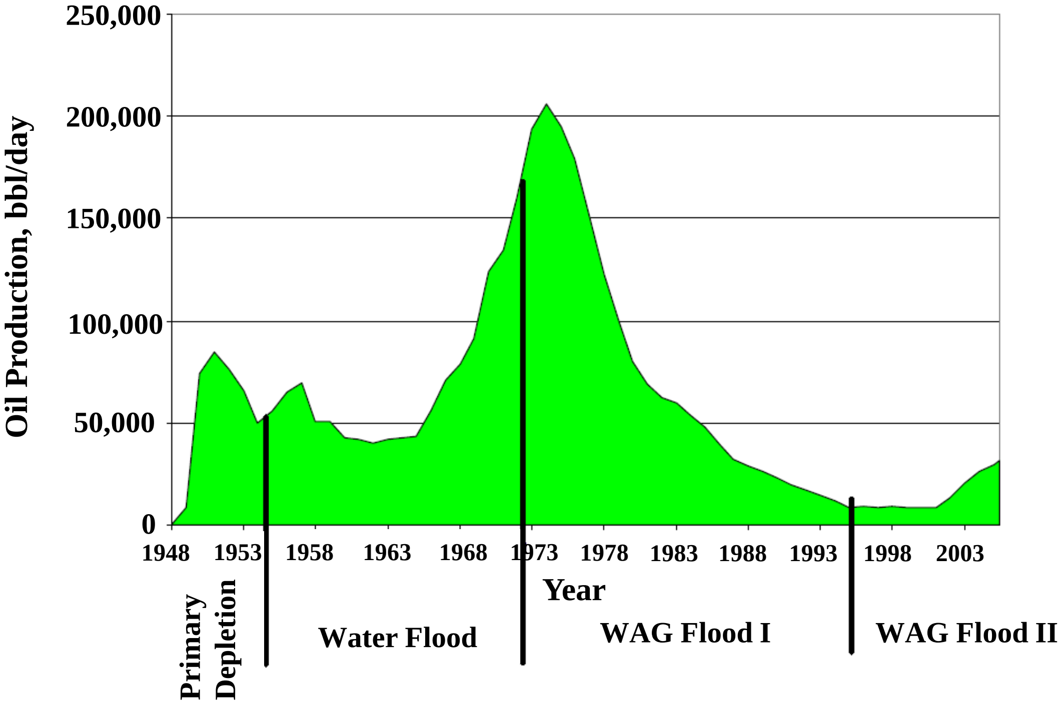

Fig. 5.1—SACROC Unit: historical oil production and EOR operations (Brnak et al. 2006).

Furthermore, heterogeneous distribution of the petrophysical properties is an evident attribute of Canyon Reef, the main producing formation in the SCAROC Unit. Canyon Reef is a Pennsylvanian age limestone carbonate that was exposed to high-amplitude sea-level fluctuations, resulting the rapid vertical growth of the reef. As a result, Canyon Reef formation is characterized by increased heterogeneity and lateral and vertical discontinuity of porosity and permeability (Kane 1979; Brnak et al. 2006). WAG injection is intended to provide effective profile control in reservoirs with communicating layers of variable petrophysical properties, in which the injected fluids have a tendency to flow to high permeability layers and bypass layers with low permeability (Gorell 1990). However, in formations with poor vertical communication, such as the Canyon Reef, this mechanism might not be as effective. In these reservoirs, the vertical distribution of the injected fluids is dominated by permeability contrasts, and, unlike reservoirs with communicating layers, it is almost independent of the WAG ratio. Fluid flow into each layer is proportional to its fraction of the overall flow capacity, kh, where k is the permeability in millidarcy (md) and h is the height of layer in ft. Consequently, the most permeable layer receives a higher fraction of the injected fluids, compared to the neighboring low-permeability layers. This disparity causes reorientation of pressure profiles when alternating the injected fluids, thus reducing injectivity.

5.3 Method

Petrophysical rock classification based on conventional well logs was applied to characterize distribution of petrophysical properties and mineralogy. The inputs to the rock classification were depth-by-depth estimates of porosity and permeability and mineralogy, obtained from the joint-interpretation of conventional well logs. A new heterogeneity coefficient was used to quantify spatial variation of rock classes in the formation. A comparison of the heterogeneity coefficient in the wells with and without anomalous injectivity abnormality during WAG operations can provide insight into the impact of formation spatial heterogeneity on injectivity abnormalities. Furthermore, variogram analysis was conducted to validate the new heterogeneity coefficient and its application for real-time decision making on selection of the best WAG injectors. The following sections provide a detailed description of the method.

5.3.1 Well-Log Interpretation

I conducted multi-mineral analysis by joint inversion of conventional well logs to estimate petrophysical and compositional properties. The input well logs included gamma ray (GR), electrical resistivity, density, neutron porosity, Photoelectric Factor (PEF), and compressional-wave slowness. The types of minerals in the formation were determined using the available core descriptions and field reports. I estimated porosity and water saturation using Wyllie’s time-average equation (Wyllie et al. 1956) and Archie’s equation (Archie 1942), respectively.

Furthermore, I constructed a supervised model based on *k*-Nearest Neighbors (*KNN*) algorithm (Cover and Hart 1967), with an input of core porosity and permeability measurements, to estimate permeability in the well-log domain. The model was trained using 80% of the input dataset and tested on the remaining 20%.

5.3.2 Petrophysical Rock Classification

An unsupervised artificial neural network was constructed for automatic rock classification in the formation using the Kohonen algorithm (Kohonen 2001). The inputs for rock classification included depth-by-depth estimates of porosity, permeability, and volumetric concentrations of minerals, obtained from well-log interpretation, MICP-based pore types (determined in Chapter III), and the number of rock classes. I determined the latter based on the properties of pre-defined lithofacies, as well as the observed variability in the input data. The outcome of the rock classification was the rock classes of similar distribution in porosity, permeability, and mineralogy. The artificial neural network iteratively classifies the input data into individual groups by minimizing their intra-class variance using the Ward's Hierarchical clustering method (Ward 1963; Guha et al. 1998). The input data are iteratively organized and assigned to particular nodes on the Self-Organizing Map (SOM), also known as the Kohonen map (Kohonen 2001). I conducted geostatistical analysis on the distribution of identified rock classes to quantify the spatial heterogeneity, in terms of agglomerated petrophysical properties and mineralogy, represented by each rock class.

5.3.3 Geostatistical Analysis

Commonly used measures of formation heterogeneity in the petroleum industry are the Dykstra-Parsons (Dykstra and Parsons 1950) and the Lorenz (Schmalz and Rahme 1950) coefficients. These heterogeneity coefficients provide quantitative measures of permeability variations in the formation. However, they do not account for the spatial discontinuity in permeability, which is a common feature in complex reservoirs. In addition to permeability, distribution of porosity and mineralogy should be incorporated for a reliable heterogeneity analysis. Alternatively, heterogeneity analysis can be conducted on the distribution of rock classes that are identified based on the variation of porosity, permeability, and mineralogy. For this purpose, I introduced a spatial heterogeneity coefficient, given by

$$C_H = \frac{c}{N}, \tag{5.1}$$

where C_H is the spatial heterogeneity coefficient, c is the count of the differences in the adjacent data pairs (i.e., rock classes), and N is the total number of data points. The term c is represented by

$$c = \sum_{i=1}^{N} [P_i], \tag{5.2}$$

where

$$P_i = |z_i - z_{i+1}| \neq 0. \tag{5.3}$$

z_{i+1} and z_i are the adjacent data points (i.e., rock classes) separated by the sampling distance and […] are the Iverson brackets (Iverson 1962). $[P_i]$ is defined to be 1 if P_i is true, and 0 if it is false. C_H of 0 corresponds to a homogenous formation, whereas C_H of 1 corresponds to a reservoir that is spatially heterogeneous.

I performed variogram analysis on the porosity, permeability, and mineralogy, assimilated using Principle Component Analysis (PCA), to validate application of the introduced heterogeneity coefficient. Variogram analysis is commonly applied for characterization of the spatial heterogeneity in formation petrophysical properties (Gringarten and Deutsch 1999). The main purpose of a variogram analysis is to assess the correlation length of a variable, which represents the spatial discontinuity of a variable (e.g., permeability) (Isaaks and Srivastava 1989).

I applied PCA to assimilate estimates of porosity, permeability, and mineralogy without significant loss of variability in the dataset. The first Principle Component (PC1) which contains most of the variability in the input dataset is used for variogram analysis (Guide to Statistics 2000). Input data are transformed to PCs using the eigenvectors of the covariance matrix. Covariance of a matrix with two variables, x and y, is defined as

$$C = \operatorname{cov}(x, y) = \frac{\sum_{i=1}^{N}(x_i - \bar{x})(\mathrm{y}_i - \bar{y})}{\left[\sum_{i=1}^{N}(x_i - \bar{x})^2 \sum_{i=1}^{N}(y_i - \bar{y})^2\right]^{\frac{1}{2}}}, \tag{5.4}$$

where C is the covariance matrix, x_i and y_i are depth-by-depth estimates of the first and the second variable, respectively, and $\bar{x}$ and $\bar{y}$ are the mean values of the x and y variables, respectively. I applied spectral decomposition to identify the eigenvalues and eigenvectors of the covariance matrix such that

$$C = V^T V \Lambda, \tag{5.5}$$

where Λ is the matrix of eigenvalues, V is the eigenvector matrix, and V^T indicates the transpose of eigenvector matrix. The eigenvector with the highest eigenvalue provided the Principle Component (PC) with the highest contribution to the total variability in the dataset. PCs were ranked in the order of their contribution to the variability in the dataset.

5.4 Results

I applied the described technique to ten wells in the SACROC Unit. Five of the wells under study experienced WAG sensitivity (i.e., injectivity abnormality) and are denoted by Well-S-# in this chapter. The other five wells were WAG-insensitive (with no injectivity abnormality) and are labeled as Well-I-#. Core porosity and permeability measurements were available in eight wells. I conducted multi-mineral analysis using the available conventional well logs to assess porosity, permeability, and mineralogy in all wells. As the productive interval of the Canyon Reef is mainly composed of limestone and minor amounts of shale, the types of minerals in the multi-mineral analysis were assumed to be calcite and clay. The outcome of the multi-mineral analysis was depth-by-depth estimates of porosity, volumetric concentrations of minerals, and water saturation. The estimates of porosity were validated using the available core measurements of porosity. **Fig. 5.2** shows the estimates of porosity, with an approximate average relative error of 20%, compared to core measurements of porosity. Core descriptions were used to verify the estimates of mineralogy. Assessment of water saturation is not a focus of this work, as the SACROC Unit has undergone extensive water flooding.

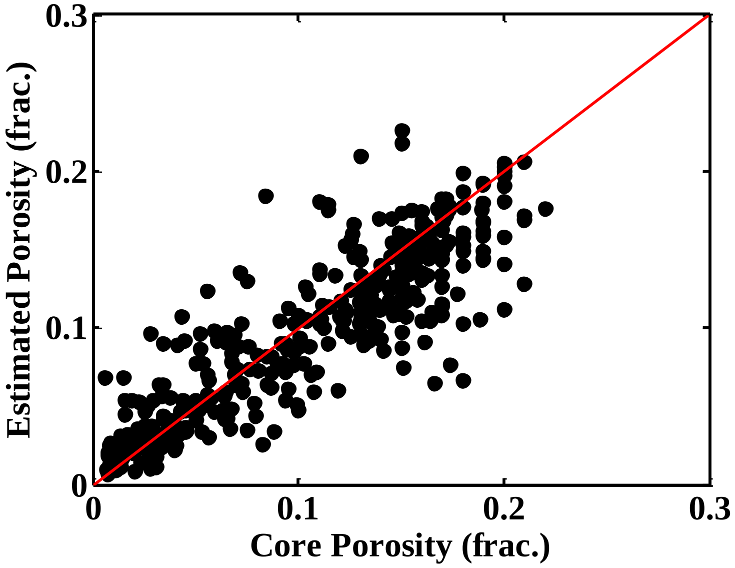

Fig. 5.2—SACROC Unit: comparison of porosity estimated from multi-mineral analysis, against core measurements. Estimates of porosity have an approximate average relative error of 20%.

Furthermore, I estimated permeability by constructing a supervised *KNN*-based model using core porosity and permeability measurements. The model was trained by an input of core porosity and an output of core permeability in six wells and then was tested on the other two cored wells for quality control. **Fig. 5.3** shows the estimates of permeability against core measurements of permeability in the two tested wells. The average relative error associated with the estimates of permeability in the tested dataset was approximately 34%.

I then performed rock classification using the depth-by-depth estimates of porosity, permeability, and volumetric concentrations of clay and calcite, and MICP-based pore types (refer to Chapter III) in all ten wells. Three rock classes were identified on account of the variability in porosity, permeability, and mineralogy. **Table 5.1** lists the properties of the identified rock classes.

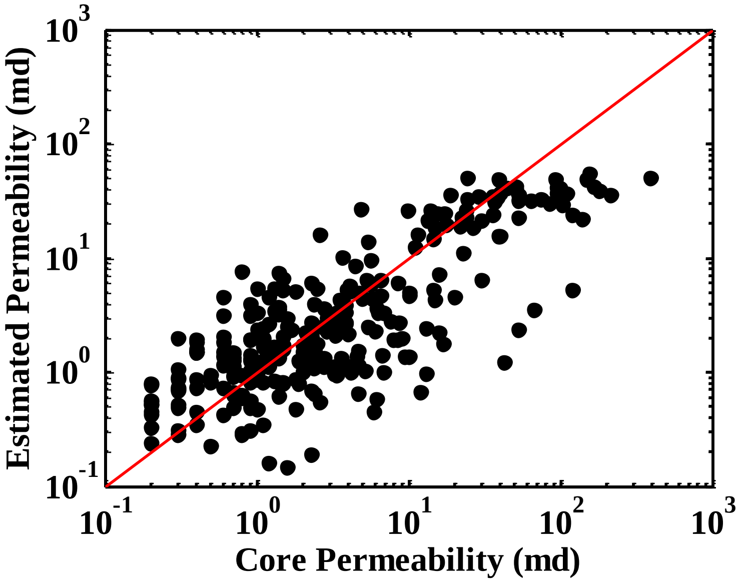

Fig. 5.3—SACROC Unit: comparison of permeability estimated by *KNN*-based supervised model, against core measurements. Estimates of permeability have an approximate average relative error of 34%.

Rock Class	Porosity	Permeability	Volumetric Concentration of
1	0.16 ± 0.02	133.30 ± 4.30	0.06 ± 0.01
2	0.10 ± 0.00	126.60 ± 9.74	0.07 ± 0.00
3	0.04 ± 0.01	92.30 ± 10.50	0.21 ± 0.02

Table 5.1—SACROC Unit: general properties of the identified petrophysical rock classes.

Rock class 1 is best rock class, characterized by the highest porosity and permeability, and the lowest volumetric concentration of clays. Rock class 3, on the other hand, is the worst rock class with the lowest porosity and permeability, and the highest clay content.

Moreover, **Figs. 5.4** and **5.5** illustrate conventional well logs and results of multi-mineral analysis, permeability assessment, and rock classification in a WAG-sensitive well and a WAG-insensitive well, respectively.

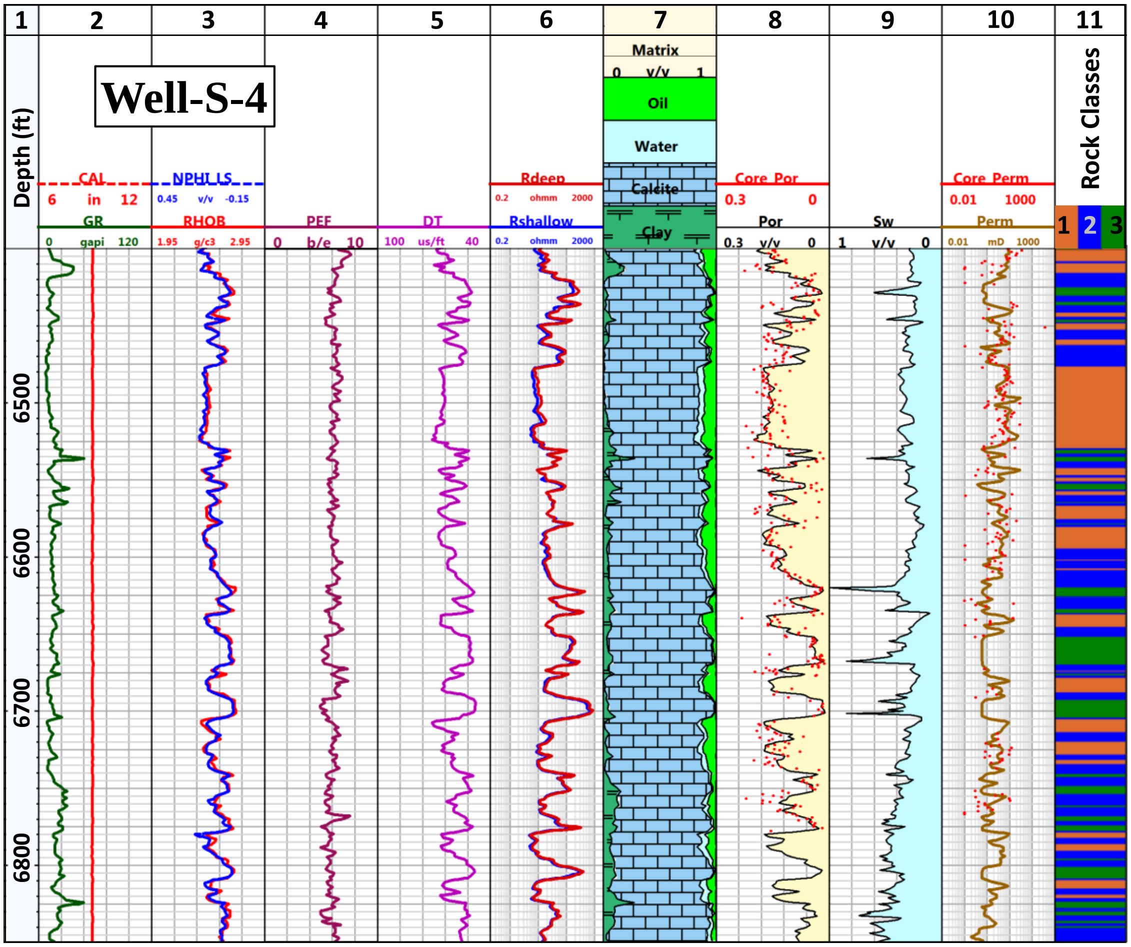

Fig. 5.4—SACROC Unit: conventional well logs and results of multi-mineral analysis, permeability assessment, and rock classification in Well-S-4 (WAG sensitive). Tracks from left to right include, Track 1: depth; Tracks 2-6: GR, caliper, neutron porosity (in water-filled limestone units), bulk density, PEF, compressional-wave slowness, and apparent resistivity logs; Track 7: estimates of volumetric concentrations of calcite and clay; Track 8: estimates of total porosity, compared to core measurements (red dots); Track 9: estimates of water saturation; Track 10: estimates of permeability, compared to core measurements; Track 11: petrophysical rock classes.

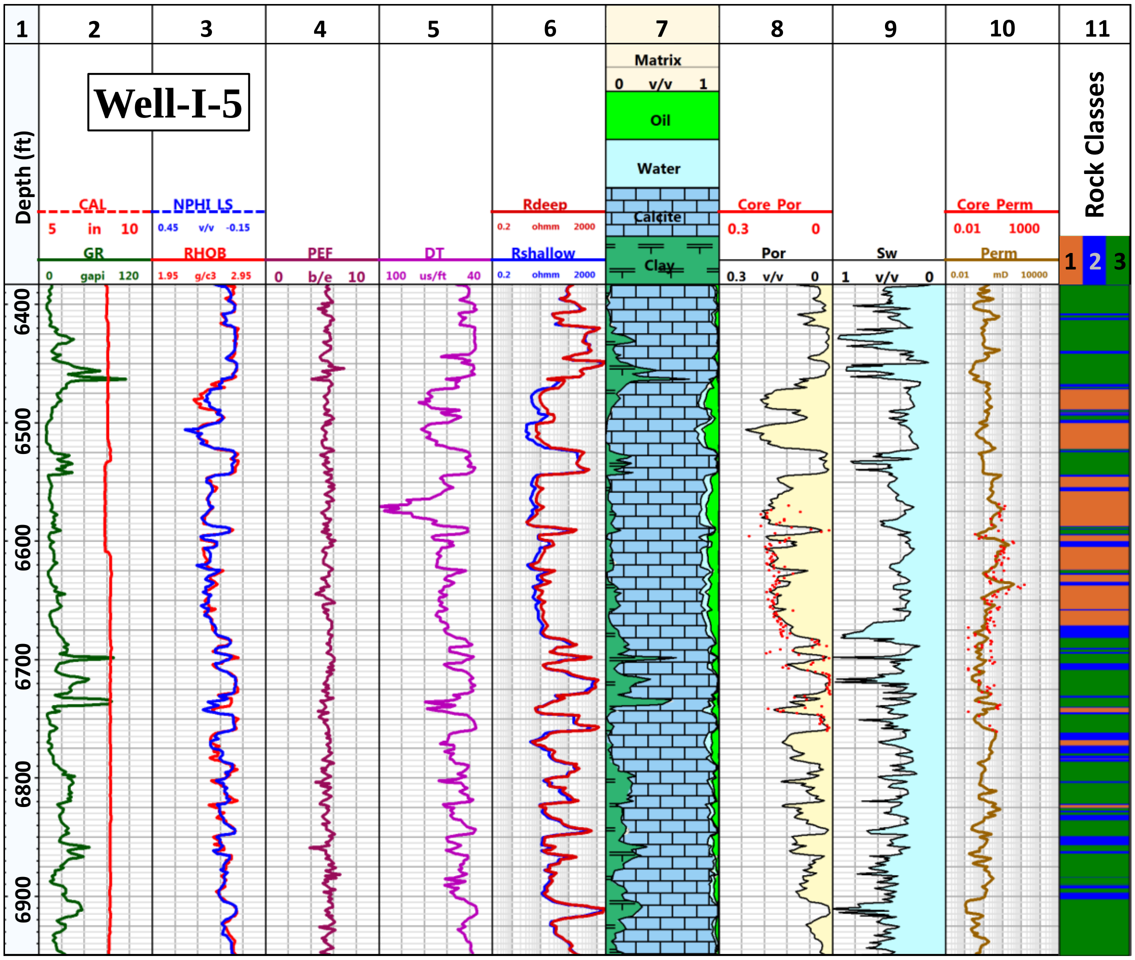

Fig. 5.5—SACROC Unit: conventional well logs and results of multi-mineral analysis, permeability assessment, and rock classification in Well-I-5 (WAG insensitive). Tracks from left to right include, Track 1: depth; Tracks 2-6: GR, caliper, neutron porosity (in water-filled limestone units), bulk density, PEF, compressional-wave slowness, and apparent resistivity logs; Track 7: estimates of volumetric concentrations of calcite and clay; Track 8: estimates of total porosity, compared to core measurements (red dots); Track 9: estimates of water saturation; Track 10: estimates of permeability, compared to core measurements; Track 11: petrophysical rock classes.

Fig. 5.6 shows a side-by-side comparison of the outcome of rock classification in all ten wells. The distribution of rock classes appears to be more heterogeneous in the WAG-sensitive wells, compared to the distribution of rock classes in the WAG-insensitive wells. This observation was confirmed by the new spatial heterogeneity coefficient that quantified the distribution of rock classes in all the wells.

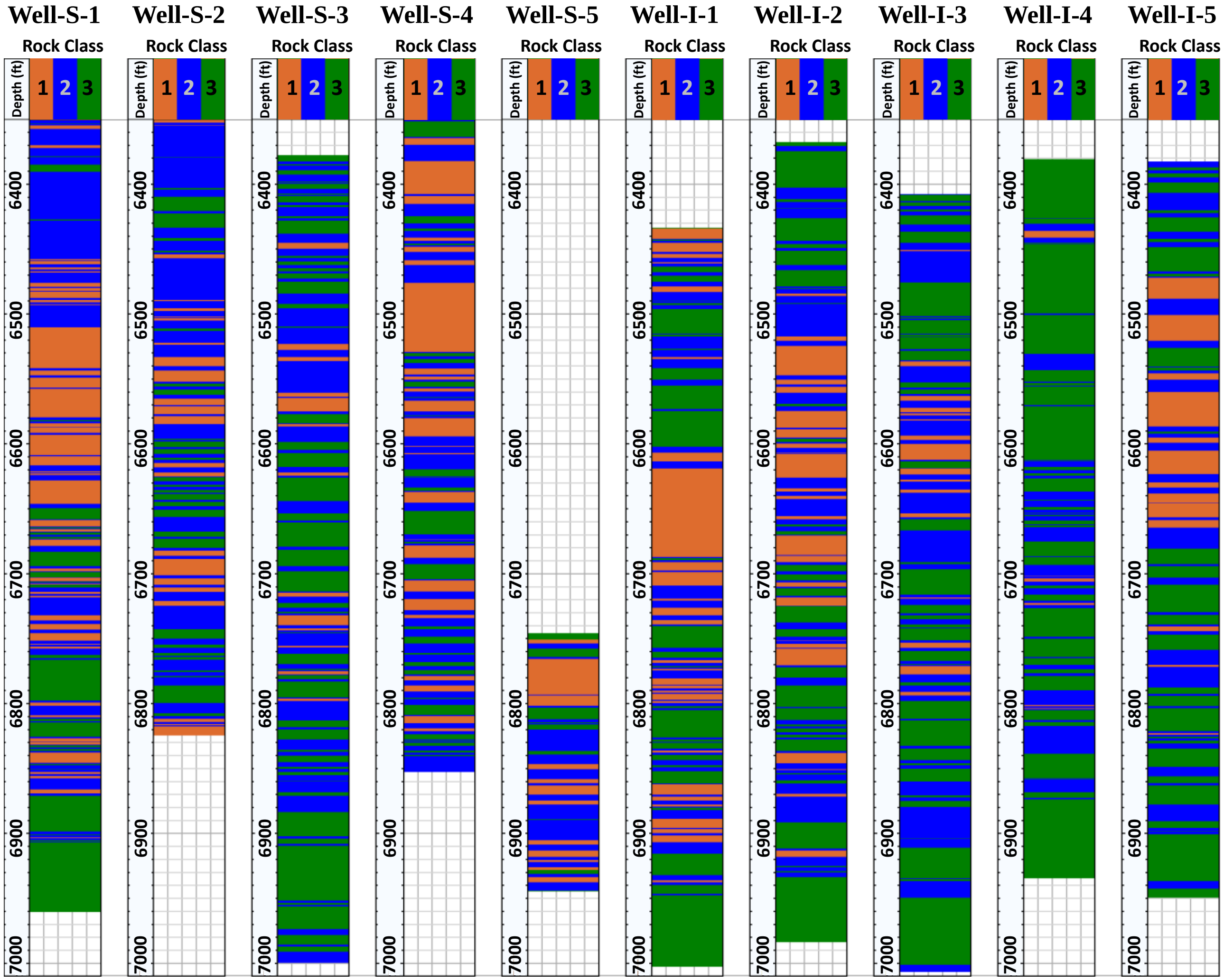

Fig. 5.6—SACROC Unit: the results of rock classification in five WAG-sensitive and five WAG-insensitive wells. Distribution of rock classes in WAG-sensitive wells is relatively more heterogeneous compared to WAG-insensitive wells.

Fig. 5.7 illustrates the identified spatial heterogeneity coefficient in all ten wells. The comparison of the average spatial heterogeneity coefficients of the WAG-sensitive wells and the WAG-insensitive wells showed that the spatial heterogeneity of the formation is approximately 30% higher in the WAG-sensitive wells.

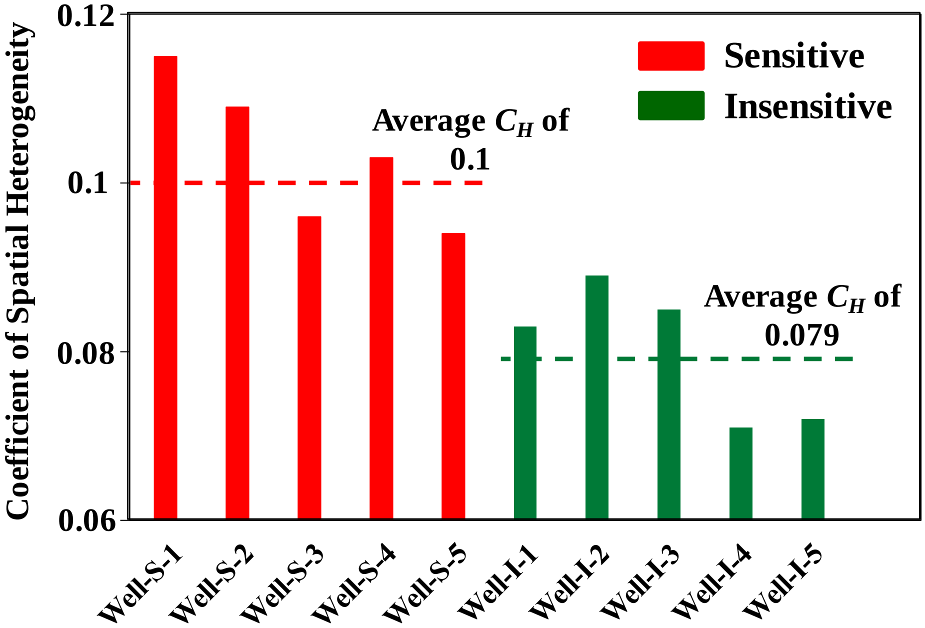

Fig. 5.7—SACROC Unit: the spatial heterogeneity coefficient determined in five WAG-sensitive and five WAG-insensitive wells. The average value of the spatial heterogeneity coefficient in the WAG-sensitive wells is approximately 30% higher than that in the WAG-insensitive wells.

Additionally, **Fig. 5.8** indicates the average concentration of rock classes in the WAG-sensitive and WAG-insensitive wells. The results illustrate 32% and 43%, higher average concentration of rock classes 1 and 2, respectively, in the WAG-sensitive wells, as compared to the WAG-insensitive wells. The higher values of spatial heterogeneity and greater concentration of rock classes with high porosity and permeability coincide with the occurrence of the injectivity loss during WAG operations in the WAG-sensitive wells.

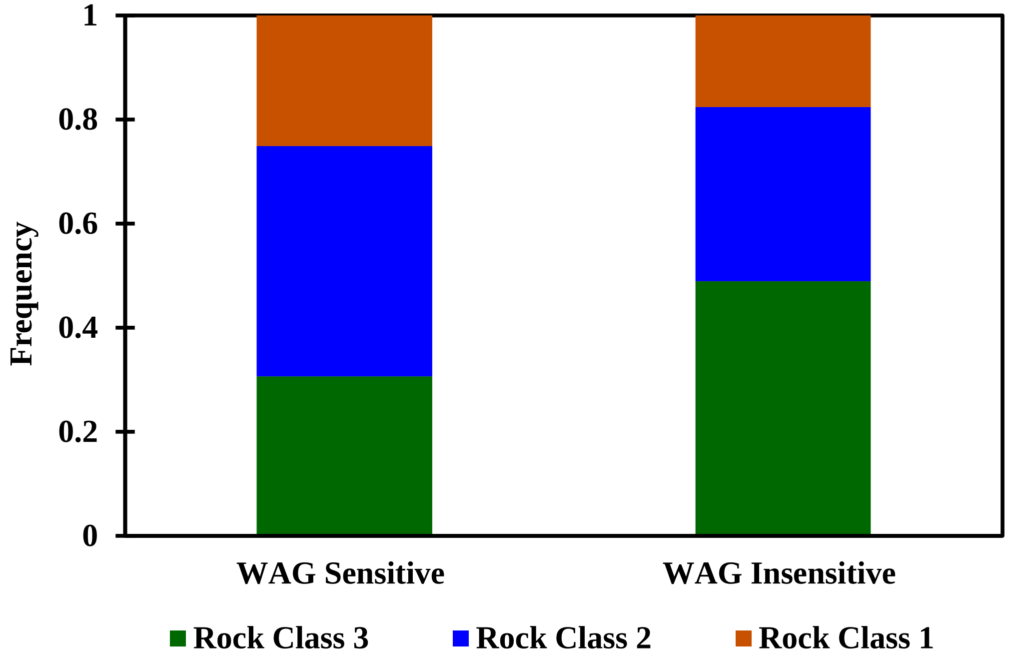

Fig. 5.8—SACROC Unit: the average concentration of three rock classes in WAG sensitive and WAG insensitive wells. The average concentration of rock classes 1 and 2, with relatively high porosity and permeability, are 32% and 43%, respectively, higher in the WAG sensitive wells, compared to the WAG insensitive wells.

Furthermore, I applied variogram analysis to validate the application of the new spatial heterogeneity coefficient. The spatial heterogeneity analysis by the new coefficient is conducted on the distribution of porosity, permeability, and mineralogy, categorized in the form of rock classes. However, variogram analysis cannot be applied to a distribution of qualitatively labelled rock categories (e.g., rock classes and geological lithofacies) in the formation. Thus, to evaluate viability of the new spatial heterogeneity coefficient, I first determined PC1 of the estimates of porosity, permeability, and volumetric concentrations of calcite and clay in all ten wells. I then conducted variogram analysis on the determined PC1 using the exponential variogram model. **Figs. 5.9** and **5.10** show the variograms of Well-S-1 and Well-I-, respectively.

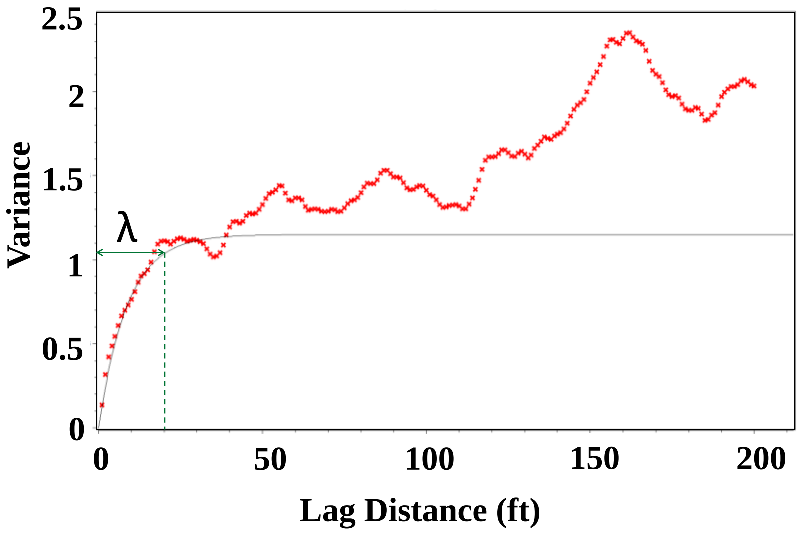

Fig. 5.9—SACROC Unit: variogram analysis in Well-S-1. The estimated correlation length, *λ*, is approximately 20 ft.

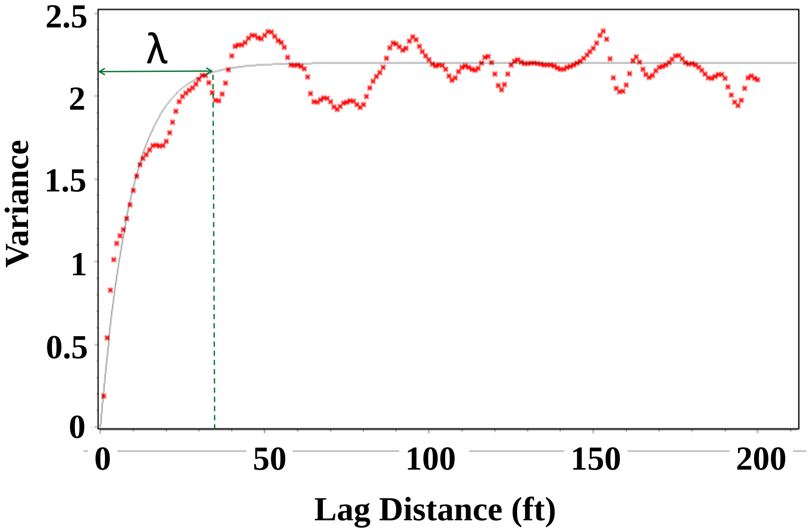

Fig. 5.10—SACROC Unit: variogram analysis in Well-I-1. The estimated correlation length, *λ*, is approximately 35 ft.

The first structure displayed on the variogram plot was used to determine the correlation length, as the first few variogram points are known to be more reliable for model-fitting and determination of the correlation length (Beatty 2010). The correlation lengths in Well-S-1 and Well-I-1 were approximately 20 ft and 35 ft, respectively. **Fig. 5.11** illustrates all variograms of (a) WAG-sensitive wells and (b) WAG-insensitive wells. The results show that the variograms of the WAG-sensitive wells correspond to a smaller correlation length and a higher heterogeneity, compared to those of the WAG-insensitive wells.

The heterogeneity analysis on petrophysical rock classes using the new coefficient involves minimal computational time and effort, as compared to the combined PCA and variogram analysis for quantifying the spatial distribution of petrophysical properties and volumetric concentrations of minerals.

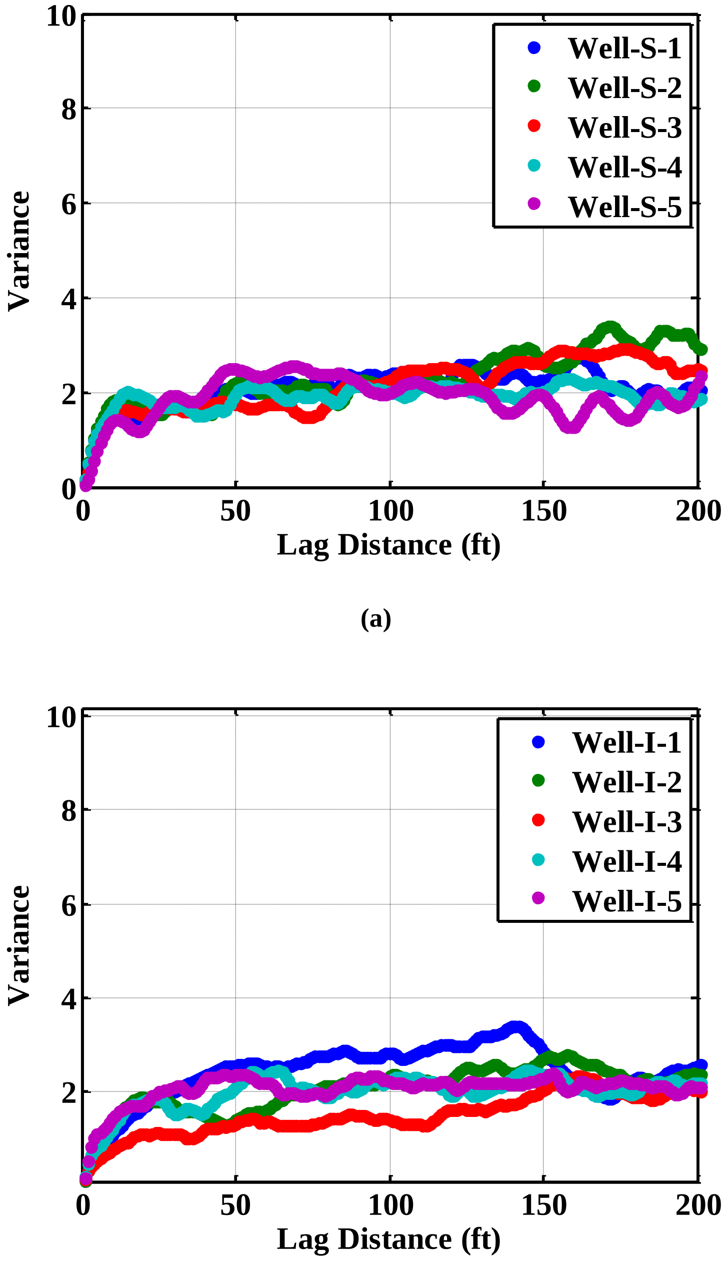

(a)

(b)

Fig. 5.11—SACROC Unit: variogram analysis in (a) five WAG-sensitive and (b) five WAG-insensitive wells. The variograms of WAG-insensitive wells exhibit larger correlation length and are more homogeneous, compared to the variograms of WAG-sensitive wells.

5.5 Conclusions

In this chapter, I investigated the impact of spatial heterogeneity in the distribution of petrophysical rock classes on the WAG injectivity loss in ten wells of the SACROC Unit. I conducted petrophysical rock classification using an unsupervised artificial neural network, with inputs of porosity, permeability, pre-defined pore types, and volumetric concentrations of minerals. A new heterogeneity coefficient was introduced and applied for quantifying the spatial variability of the identified rock classes. I determined the heterogeneity coefficients in all ten wells and compared their magnitude to investigate the impact of the formation spatial heterogeneity on the WAG injectivity loss. The results showed that in the wells with WAG injectivity loss, the distribution of rock classes is approximately 30% more heterogeneous, compared to the wells with no injectivity loss. In the same wells, I also observed about 32% and 43% higher occurrence of rock classes 1 and 2, respectively, compared to the wells with no injectivity loss. PCA on petrophysical properties and mineralogy was conducted in conjunction with variogram analysis to validate the outcome of heterogeneity analysis using the new coefficient.

The results are promising for successful application of the introduced well-log-based method for pre-selection of candidate wells for WAG injection for successful enhanced oil recovery. Although formation spatial heterogeneity can affect the success of WAG operations, there remains other formation properties and WAG design parameters that must be further investigated for their impact on WAG sensitivity.

CHAPTER VI

ROCK CLASSIFICATION IN THE HAYNESVILLE SHALE BASED ON PETROPHYSICAL AND ELASTIC PROPERTIES ESTIMATED FROM WELL LOGS*

Rock classification can enhance fracture treatment design for successful field developments in organic-shale reservoirs. Petrophysical and elastic properties of the formation are both important to consider when selecting the best candidate zones for fracture treatment. Rock classification techniques based on well logs can be advantageous compared to conventional ones based on cores and enable depth-by-depth formation characterization. This chapter proposes and evaluates three rock classification techniques in organic-rich shale formations which incorporate well logs and well-log-based estimates of elastic properties, petrophysical properties, mineralogy, and organic-richness. The three rock classification techniques include (a) a 3D cross-plot analysis of organic richness, volumetric concentrations of minerals, and rock brittleness index, (b) an unsupervised artificial neural network, built from an input of well logs, and (c) an unsupervised artificial neural network, constructed using an input of well-log-based estimates of petrophysical, compositional, and elastic properties. The self-consistent

---

*Reprinted with permission from “Rock Classification in the Haynesville Shale Based on Petrophysical and Elastic Properties Estimated from Well Logs” by Mehrnoosh Saneifar, Alvaro Aranibar, and Zoya Heidari, 2014. *SEG Interpretation Journal*, 3, SA65–SA75, Copyright 2014 by the Society of Exploration Geophysicists and American Association of Petroleum Geologists. http://dx.doi.org/10.1190/INT-2013-0198.1.

approximation model is applied to estimate elastic rock properties. This model enables estimation of the elastic properties based on the well-log-derived estimates of mineralogy and the shapes of rock components, in the absence of acoustic-wave velocity logs. Finally, the three proposed techniques were applied to the Haynesville Shale for rock classification. The identified rock types were verified using thin-section images and the previously-identified lithofacies. The results showed that well logs can be directly used for rock classification instead of petrophysical/compositional properties obtained from well-log interpretation. Use of well logs, instead of the well-log-derived estimated properties, can reduce uncertainty associated with the physical models used to estimate elastic moduli and petrophysical/compositional properties. The three proposed well-log-based rock classification techniques can potentially enhance fracture treatment for production from complex organic-shale reservoirs through (a) detecting the best candidate zones for fracture treatment and (b) optimizing the number of required fracture stages.

6.1 Introduction

Recent advances in completion techniques such as hydraulic fracturing have transformed organic-shales into economic plays during the past decade. Production from these resources is challenged by the complex and tight pore structures of the shale reservoirs (King 2010). Parameters such as hydrocarbon content and formation porosity alone are not sufficient for sweet-spot selection in organic-shale formations. It is possible to have a well with good storage capacity (porosity) and high total organic content (TOC), but small hydrocarbon production because of hydraulic fracture failure (Gupta et al. 2012). Petrophysical, compositional, and elastic properties are needed to select hydraulic fracture initiation points in organic-shale reservoirs. However, selection of fracture locations can be difficult due to the heterogeneous distribution of rock properties in organic-shale formations. Rock classification can be used to improve fracture placement.

Rock classification in conventional reservoirs has been proven to be effective for subsurface reservoir description (Xu et al. 2012; Xu and Torres-Verdin 2013a and 2013b). However, conventional rock typing techniques using core porosity and core permeability measurements (Amaefule et al. 1993; Leverett 1941; Lucia 2007; Pittman 1992) are not reliable for organic-shale reservoirs. Unlike in carbonate and sandstone formations, ranges of porosity and permeability variation in organic-shale formations are narrow. Furthermore, the uncertainty in laboratory measurements of the ultra-low permeability is significant in these formations (Kale et al. 2010).

Recent studies on rock classification in organic-shale reservoirs were based on core measurements of TOC, porosity, and mineralogy (Gupta et al. 2012; Kale et al. 2010). Hammes and Frébourg (2012) identified the main lithofacies in the Haynesville Shale using an extensive core database. Characterization of rock heterogeneity and rock typing based on core data in organic-shale reservoirs requires a large database of core measurements. They usually cover small depth sampling intervals. However, acquisition of a large core database is expensive and uncertainties in core measurements in organic-shale formations are large.

Well logs are good alternative input data for rock typing in organic-shale reservoirs, where core measurements are sparse and uncertain. Popielski et al. (2012) conducted rock classification in the Barnett and the Haynesville shales based on bed-by-bed estimates of total porosity, concentrations of kerogen and other minerals, and fluid saturations, simultaneously obtained from nonlinear joint inversion of well logs. However, elastic rock properties should be included in rock classification for a reliable selection of fracture candidate zones (Gupta et al. 2012).

Elastic rock properties (e.g., Young's modulus and Poisson's ratio) provide information about brittleness of a formation and its reaction to fracture treatment. Poisson's ratio and Young's modulus reflect the possibility of fracture initiation and the ability of the rock to keep the fracture open after propagation, respectively (Rickman et al. 2008). Gupta et al. (2012) and King (2010) also discuss the influence of Young's modulus and Poisson's ratio on the ability of the rock to be fractured. They agree with Rickman et al. (2008) on the possible increased fracture potential of rocks with high Young's modulus and low Poisson's ratio. In situ assessment of elastic rock properties in organic-shale formations, however, can be complicated. Previous publications showed that empirical rock-physics techniques might not be reliable in organic-shale formations which can result in estimates that do not agree with laboratory measurements (Jiang and Spikes 2011). Furthermore, the abnormally high pore pressure in geopressured shale-gas formations (e.g., the Haynesville Shale) causes a slow-down in the first compressional arrival that does not represent the true elastic properties of the formation (Parker et al. 2009). Effective medium theories are other alternatives that can be applied to estimate elastic properties in complex organic-shale formations (Jiang and Spikes 2011; Montaut et al. 2013). They take into account the impact of shapes and volumetric concentrations of rock components (i.e., minerals and pore space) in estimation of elastic properties.

In this chapter, three well-log-based rock classification techniques based on petrophysical, compositional, and elastic properties are proposed and compared. The three proposed rock classification techniques include (a) 3D cross-plot analysis of organic richness, volumetric concentrations of minerals, and rock brittleness index, (b) unsupervised artificial neural network constructed from a direct input of well logs, and (c) unsupervised artificial neural network constructed using an input of well-log-based estimates of petrophysical, compositional, and elastic properties. The main advantage of the three proposed rock classification techniques, compared to the previous rock classification methods in organic-shale formations (Gupta et al. 2012; Hammes and Frébourg 2012; Kale et al. 2010; Popielski et al. 2012), is the inclusion of well-log-based estimates of elastic properties, in addition to petrophysical and compositional properties, in rock classification. The proposed rock classification techniques can be applied to enhance selection of fracture candidate zones and production planning in organic-shale reservoirs. The following sections describe the proposed techniques and their application to the Haynesville Shale.

6.2 Method

In this section, I first describe the three proposed rock classification techniques (a) 3D cross-plot analysis of organic richness, volumetric concentrations of minerals, and rock brittleness index, (b) unsupervised artificial neural network using an input of well logs, and (c) unsupervised artificial neural network built from an input of well-log-based estimates of petrophysical, compositional, and elastic properties. Next, I explain the methods employed to obtain the well-log-based estimates of petrophysical, compositional, and elastic properties.

6.2.1 Three Rock Classification Techniques

In the first rock classification technique, I applied a 3D cross-plot analysis to identify different rock classes based on well-log-derived properties, including organic richness, volumetric concentrations of minerals, and rock brittleness index. I used the *K*-means clustering technique (MacQueen 1967; Lloyd 1982; Spath 1985) to identify different rock classes.

In the second and the third rock classification techniques, unsupervised artificial neural network was applied to classify automatically different rock types in organic-shale formations (Saneifar et al. 2014a). The difference between the second and the third techniques was the input data to the network. **Fig. 6.1** shows the input data and the output of two unsupervised artificial neural networks used in the second and the third rock classification techniques.

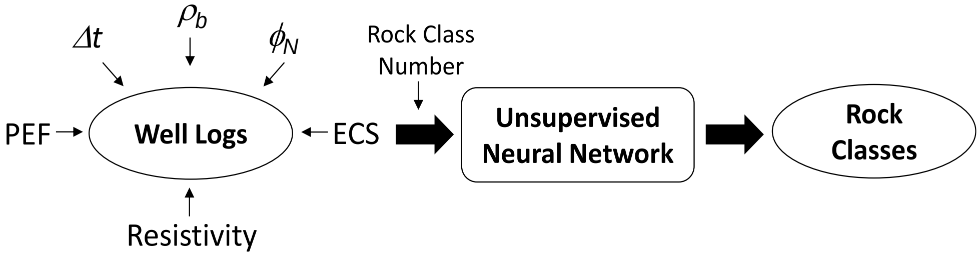

(a)

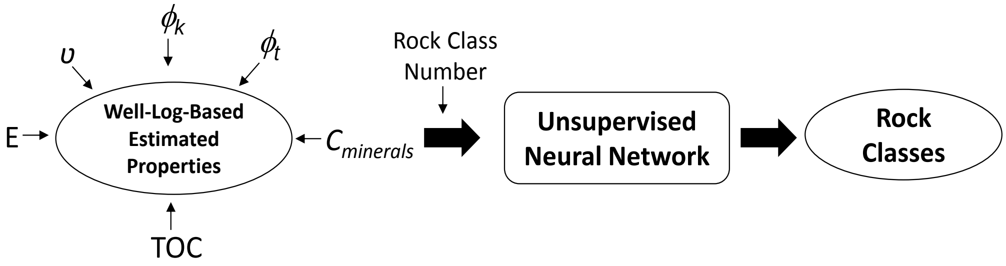

(b)

Fig. 6.1—Workflows showing inputs and output (i.e., rock classes) of the unsupervised artificial neural networks used in the second and the third rock classification techniques in the Haynesville Shale. (a) The second rock classification technique: the input data to the artificial neural network include well logs; (b) The third rock classification technique: the input data to the artificial neural network include well-log-based estimated properties.

The input data for both artificial neural networks were selected to be representative of petrophysical, compositional, and elastic properties of the formation. Fig. 6.1a shows the second rock classification technique based on an artificial neural network, built using an input of well logs, including bulk density, neutron porosity, photoelectric factor (PEF), apparent deep resistivity, compressional- and shear-wave slowness, and Elemental Capture Spectroscopy (ECS) logs. Fig. 6.1b shows the third rock classification technique based on an artificial neural network, constructed using an input of well-log-based estimated properties, including TOC, Poisson's ratio, Young's modulus, total porosity, and volumetric concentrations of minerals. The number of rock types, determined based on previous field studies (Hammes and Frébourg 2012), thin sections, and core images, were also inputs to both networks.

The applied artificial neural networks adopted a Self-Organizing Map (SOM), also known as Kohonen map, to index different input parameters by a fuzzy clustering algorithm (Kohonen 2001). The fuzzy clustering algorithm enables classifying input data with similar behavior. The self-organizing process includes simple iterative steps to organize similar input data and to assign them to particular nodes on the map. Unlike a supervised artificial neural network, an unsupervised network does not require training with pre-determined rock classes (Gottlib-Zeh 2000). The following sections explain the methods to obtain input data for all three proposed rock classification techniques.

6.2.2 Well-Log Interpretation

A joint inversion of PEF, bulk density, neutron porosity, apparent resistivity, compressional- and shear-wave slowness, and ECS logs was conducted to estimate total porosity and volumetric/weight concentrations of minerals and fluids. The assumed petrophysical and compositional model included non-clay minerals, clay minerals, organic matter, fluid saturations, and total pore space (Ambrose et al. 2010; Quirein et al. 2010). The types of existing minerals were identified based on core X-Ray Diffraction (XRD) measurements (Saneifar et al. 2014a).

The large number of unknown petrophysical and compositional properties leads to non-uniqueness of the results. To mitigate this non-uniqueness, well-log-based estimates of volumetric concentration of kerogen were used as an input to the joint inversion of well logs. The ΔlogR technique was employed to estimate TOC using compressional-wave slowness and resistivity well logs (Passey et al. 1990; Quirein et al. 2010). Estimates of TOC were verified using core measurements (Saneifar et al. 2014a). Volumetric concentration of kerogen was then calculated based on the estimates of TOC and by taking into account the organic maturity of the formation (Passey et al. 1990; Quirein et al. 2010).

6.2.3 Assessment of Kerogen Porosity

Kerogen porosity corresponds to the hydrocarbon storage capacity in organic-rich shale formations and, therefore, it is important to be taken into account in rock classification in these formations. I estimated kerogen porosity using a model introduced by Alfred and Vernik (2012). This model assumes that kerogen pore space is filled with hydrocarbon, and water is stored in the non-kerogen matrix. Kerogen porosity in this model is defined by kerogen pore volume divided by kerogen bulk volume. The first step to estimate kerogen porosity is to identify kerogen density. To estimate kerogen density, I derived the correlation between grain density and total organic content (TOC) using core measurements (Quirein et al. 2010). This correlation is given by

$$\frac{1}{\rho_{grain}} = 0.003\mathrm{TOC} + 0.36\,, \tag{6.1}$$

in the Haynesville Shale field example evaluated in this chapter. I then estimated kerogen density by assuming TOC is equal to 100%. The constants in **Eq. 6.1** can be updated for different formations using core measurements.

I then estimated kerogen porosity by solving the bulk density equation given by

$$\rho_b = \rho_{bnk} - \frac{TOC\rho_{nk}(1-\phi_{nk})(\rho_{bnk}-\rho_{bk})}{A + TOC\rho_{nk}(\phi_k - \phi_{nk})}, \tag{6.2}$$

where ϕ_k and ϕ_{nk} are kerogen and non-kerogen porosities, ρ_b and ρ_{nk} are bulk density and non-kerogen matrix density, and ρ_{bk} and ρ_{bnk} are kerogen and non-kerogen bulk densities (Alfred and Vernik 2012). Kerogen and non-kerogen bulk densities are given by

$$\rho_{bk} = \rho_k - \phi_k(\rho_k - \rho_{hc}) \tag{6.3}$$

and

$$\rho_{bnk} = \rho_{nk} - \phi_{nk}(\rho_{nk} - \rho_w), \tag{6.4}$$

respectively, where ρ_k is kerogen density, ρ_{hc} is hydrocarbon density, and ρ_w is water density. Non-kerogen porosity and *A* are given by

$$\phi_{nk} = \phi_t - \frac{\phi_k V_{bk}}{V_{bnk}} \tag{6.5}$$

and

$$A = (1-\phi_k)[TOC(\rho_{nk} - \rho_k) + C_k\rho_k], \tag{6.6}$$

respectively, where ϕ_t is total porosity, V_{bk} is volumetric concentration of kerogen, V_{bnk} is non-kerogen bulk volumetric concentration, and C_k is organic carbon percentage in kerogen. I assumed that the organic carbon percentage in kerogen is equal to the inverse of kerogen density (Quirein et al. 2010) as given by

$$C_k \rho_k \approx 1. \tag{6.7}$$

6.2.4 Assessment of Elastic Properties of the Rock

An effective medium theory, the self-consistent approximation, was used to estimate elastic properties of the rock (Mavko et al. 2009). The self-consistent approximation model incorporates the effect of mineralogy as well as shape and elastic properties of matrix inclusions in estimation of effective elastic properties of the porous media. This technique estimates the effective bulk and shear moduli by solving the coupled equations given by

$$\sum_{i=1}^{N} x_i (K_i - K_{SC}^*) P^{*i} = 0 \tag{6.8}$$

and

$$\sum_{i=1}^{N} x_i (\mu_i - \mu_{SC}^*) Q^{*i} = 0, \tag{6.9}$$

where i refers to each rock component, x_i is the volumetric concentration of the rock component i, K_i and μ_i are the bulk and the shear moduli of the rock component i, N is the total number of inclusions, and K^*_{SC} and μ^*_{SC} are the effective bulk and shear moduli of the rock. Estimates of the volumetric concentrations of the rock components are obtained using well-log interpretation. The factors P^*_i and Q^*_i correspond to the shape geometry of each rock component and are functions of the aspect ratio and the elastic moduli of individual rock components, as well as effective elastic moduli of the rock. P^*_i and Q^*_i are determined using equations provided by Berryman (1995). The aspect ratios for grains and pores were initially determined based on thin-sections and then were iteratively updated in each rock class to guarantee an agreement between the estimated elastic moduli and core measurements (Saneifar et al. 2014a).

The self-consistent approximation model estimates high-frequency behavior for saturated rocks in terms of the wave induced fluid flow. Additionally, this model estimates homogenized low-frequency elastic properties. The self-consistent approximation simulates rocks with isolated cavities with respect to the flow where there is no time for wave-induced pore pressure to equilibrate. Therefore, the self-consistent approximation is reliable for tight organic-shale formations because their permeability is in the nano-Darcy range. Furthermore, the pores can be assumed to be isolated with minimal hydraulic communication within the fluid components of the rock (Jiang and Spikes 2011).

6.2.5 Brittleness Index

Brittleness index is a function of (a) fracture initiation potential in a rock, represented by Young's modulus and (b) the capability of the rock to maintain a fracture, reflected by Poisson's ratio. I quantified the brittleness of the rock based on dynamic Young's modulus and Poisson's ratio using a model introduced by Rickman et al. (2008). The brittleness index, expressed as a percentage, is calculated via

$$Britt_{Index} = \left(\frac{E_{Britt} + \upsilon_{Britt}}{2} \right) 100, \tag{6.10}$$

where E_{Britt} and υ_{Britt} are normalized Young's modulus and Poisson's ratio, respectively, given by

$$E_{Britt} = \frac{E - E_{\min}}{E_{\max} - E_{\min}} \tag{6.11}$$

and

$$\upsilon_{Britt} = \frac{\upsilon - \upsilon_{\max}}{\upsilon_{\min} - \upsilon_{\max}}, \tag{6.12}$$

where E_{max} and E_{min} are the maximum and the minimum Young's moduli, and υ_{max} and υ_{min} are the maximum and the minimum Poisson's ratios, respectively. Dynamic Young's modulus and Poisson's ratio were calculated using the well-log-based estimates of bulk and shear moduli (i.e., K^*_{SC} and μ^*_{SC}) from the self-consistent approximation (Birch 1960).

6.3 Field Example: The Haynesville Shale

The three proposed rock classification techniques, described in the method section, were applied to a dataset acquired from a well in the upper Jurassic Haynesville Shale in Caddo Parish, Louisiana (Saneifar et al. 2014a). The organic-rich Haynesville Shale is currently one of the most productive shale-gas plays in the United States (Hammes et al. 2011). It extends through part of northeast Texas and northwest Louisiana and is bordered by the Bossier shale from above and the Smackover limestone from below. The Haynesville Shale is composed of clay, organic matter, siliceous silt, and carbonates. Although the carbonate fraction is mainly calcite, in some layers calcite is replaced by dolomite, resulting in dolomite being the dominant carbonate mineral. The porosity ranges from 8% to 12%, and TOC varies from 1% to 8.5% (Hammes et al. 2011).

Development of the Haynesville Shale is known to be challenging due to its highly laminated nature and abruptly changing reservoir properties. A reliable rock classification is required for optimizing completion design and production enhancement in this formation. Hammes and Frébourg (2012) conducted lithofacies classification based on mineralogy, fabric, biota, and texture. Their identified lithofacies included (a) unlaminated peloidal mudstone (i.e., the most organic-rich facies), (b) laminated peloidal calcareous or siliceous mudstone, (c) bioturbated calcareous or siliceous mudstone, and (d) organic-poor facies. Although a comprehensive study on the geological attributes can contribute significantly to reservoir development, a reliable petrophysical rock classification can quantitatively categorize rock classes based on petrophysical, compositional, elastic properties.

The first step to obtain petrophysical, compositional, and elastic properties was to conduct joint-interpretation of well logs and core measurements (Saneifar et al. 2014a). **Table 6.1** summarizes the assumed Archie's parameters and fluid and formation properties used for well-log interpretation. The types of matrix mineral components were chosen based on XRD measurements. To minimize the number of unknown parameters and, consequently, the non-uniqueness of the results, minerals with similar physical properties such as illite-mica and mixed-layer clay were grouped. Then, minerals with less than 2.5% volumetric concentration were eliminated from the initial petrophysical/compositional model. The matrix components assumed in the model included quartz, plagioclase, calcite, dolomite, pyrite, illite, kerogen, gas, and saline water. To further decrease the non-uniqueness of the results from the joint inversion of well logs, a linear correlation between weight concentrations of quartz and plagioclase based on XRD data was included. The outputs of the joint inversion of well logs included estimates of porosity, fluid saturations, and volumetric/weight concentrations of clay and non-clay minerals (Saneifar et al. 2014a). The estimated volumetric concentrations of rock components were then used to estimate kerogen porosity using **Eqs. 6.1–6.7**.

Variable	**Value**	**Units**
Archie's Winsauer factor, a	1.00	( )
Archie's porosity exponent, m	2.40	( )
Archie's saturation exponent, n	2.00	( )
Formation-water salt concentration	200	kppm NaCl
Bound-water salt concentration	200	kppm NaCl
In situ water density	1.05	g/cm^3
In situ gas density	0.19	g/cm^3
In situ kerogen density	1.3	g/cm^3
Formation temperature	140	°C

Table 6.1—Summary of assumed Archie's parameters and fluid and formation properties.

Next, effective bulk and shear moduli were estimated using the self-consistent approximation method. Spherical shapes were assumed for stiffer rock components (e.g., quartz) and penny-crack shapes were assumed for softer rock components (e.g., illite). Reservoir fluids were assumed to fill the penny-shaped cracks. Calcite was partially included with a spherical shape and the rest with a penny-crack shape, based on pore-scale core images in the Haynesville Shale (Saneifar et al. 2014a).

Fig. 6.2 shows the well logs and the estimates of petrophysical, compositional, and elastic properties including total porosity, kerogen porosity, shear and bulk moduli, water saturation, and volumetric concentrations of minerals compared to the available core measurements. Relative errors of less than 13% and 10% were observed in the estimates of bulk and shear moduli, respectively, compared to the core measurements.

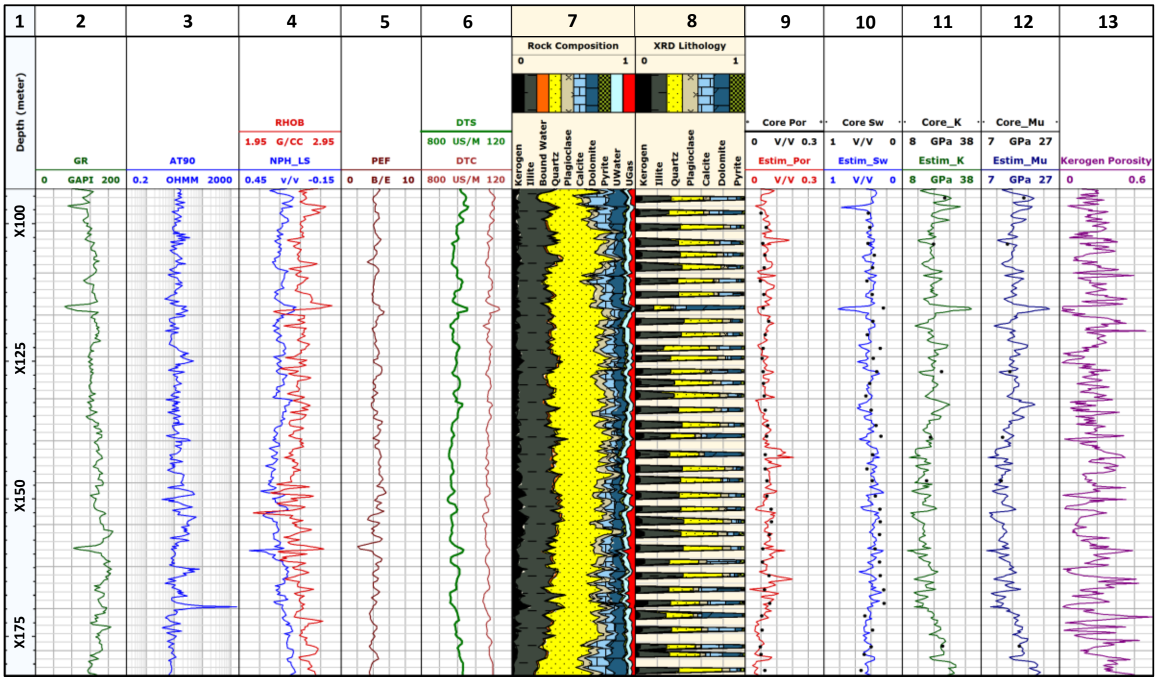

Fig. 6.2—Petrophysical and compositional well-log interpretation in the Haynesville Shale. Tracks from left to right include, Track 1: depth; Tracks 2-6: gamma ray (GR), apparent deep resistivity, neutron porosity (in water-filled limestone porosity units), bulk density, PEF, and compressional-wave slowness logs; Track 7: volumetric concentrations of minerals estimated using well logs; Track 8: solid volumetric concentrations of minerals obtained using XRD measurements; Track 9-10: total porosity and total water saturation, compared against core measurements; Track 11-12: Well-log-based estimates of bulk and shear moduli, compared against core measurements; Track 13: kerogen porosity (i.e., kerogen pore volume divided by kerogen bulk volume).

I then quantified the brittleness of the formation by calculating the rock brittleness index using well-log-based estimates of elastic properties. Results depicted in **Fig. 6.3** show that an increase in Young’s modulus and a decrease in Poisson’s ratio increases brittleness in the Haynesville Shale field example. Mineralogy of the formation as well affects rock brittleness. **Fig. 6.4** shows the impact of the increase in volumetric concentrations of quartz and illite on the brittleness index in the Haynesville Shale. Higher quartz concentration results in an increase in brittleness index, whereas higher illite concentration results in a decrease in brittleness index. I found that the impact of calcite and dolomite concentrations on the brittleness is not significant in the Haynesville Shale.

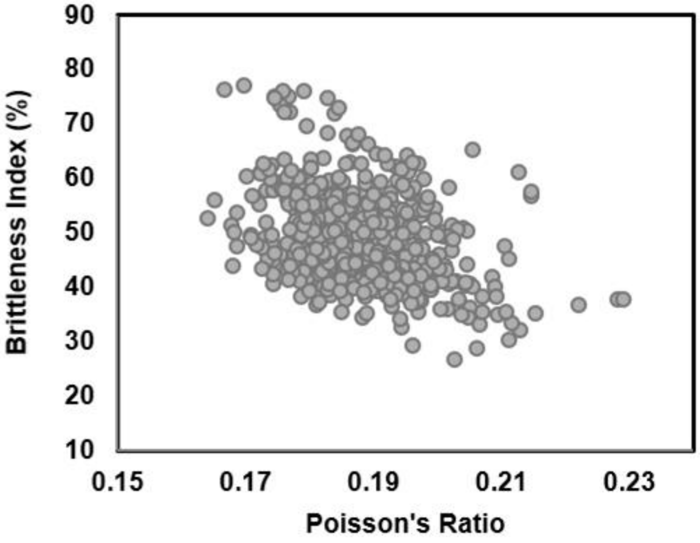

(a)

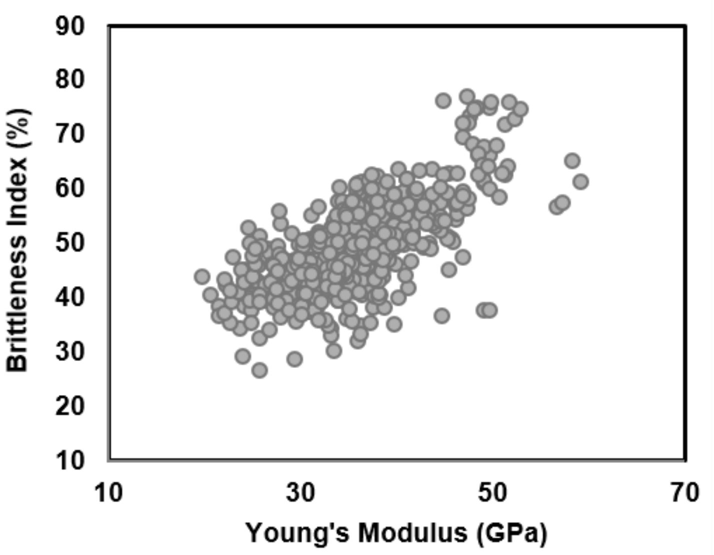

(b)

Fig. 6.3—Impact of (a) Poisson's ratio and (b) Young's modulus on rock brittleness index in the Haynesville Shale. Brittleness index, Young's modulus, and Poisson's ratio are estimated using well logs.

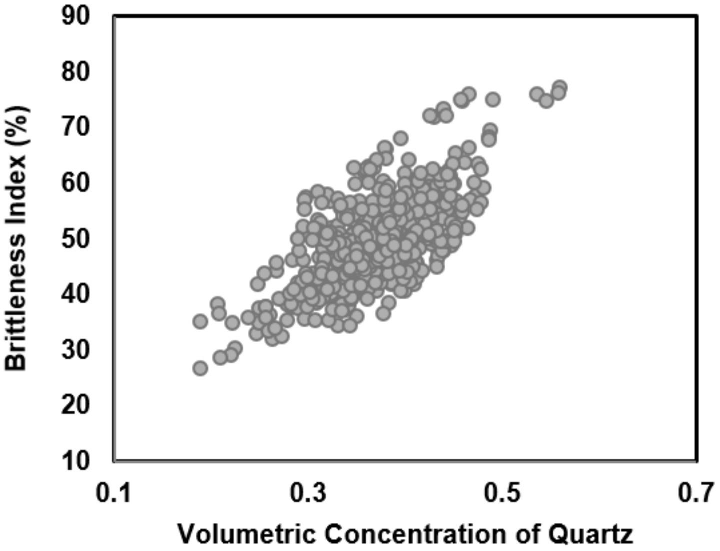

(a)

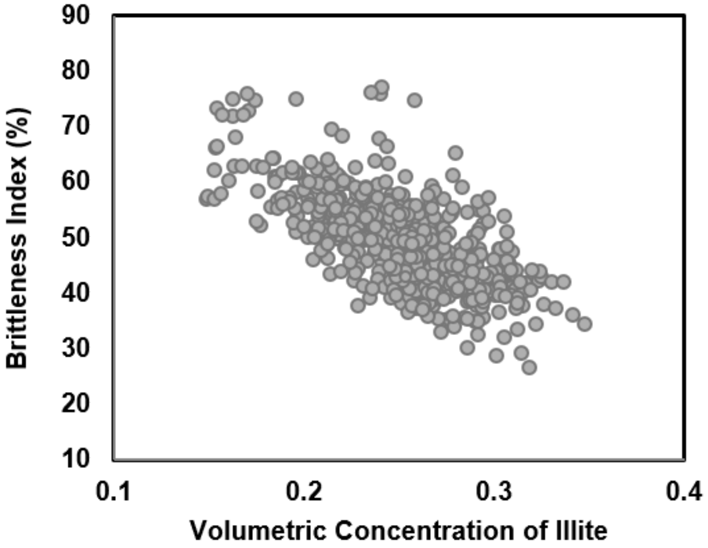

(b)

Fig. 6.4—Impact of volumetric concentrations of (a) quartz and (b) illite on the rock brittleness index in the Haynesville Shale. Volumetric concentrations of minerals and the brittleness index are estimated using well logs.

Next, I implemented the first rock classification technique, 3D cross-plot analysis, to identify different rock classes in this field example based on ΔlogR, kerogen porosity, volumetric concentrations of minerals (i.e., quartz and illite), and rock brittleness index. **Figs. 6.5** and **6.6** show the 3D cross-plots of ΔlogR, brittleness index, and volumetric concentrations of quartz and illite, respectively. The color bar in Fig. 6.6b quantifies kerogen porosity. Fig. 6.6b shows that kerogen porosity is inversely proportional to TOC and ΔlogR, with a few exceptions. I applied kerogen porosity in the first rock classification technique (i.e., 3D cross-plot analysis) to narrow the desired depth intervals for production and fracture treatment by avoiding low gas-filled kerogen porosity.

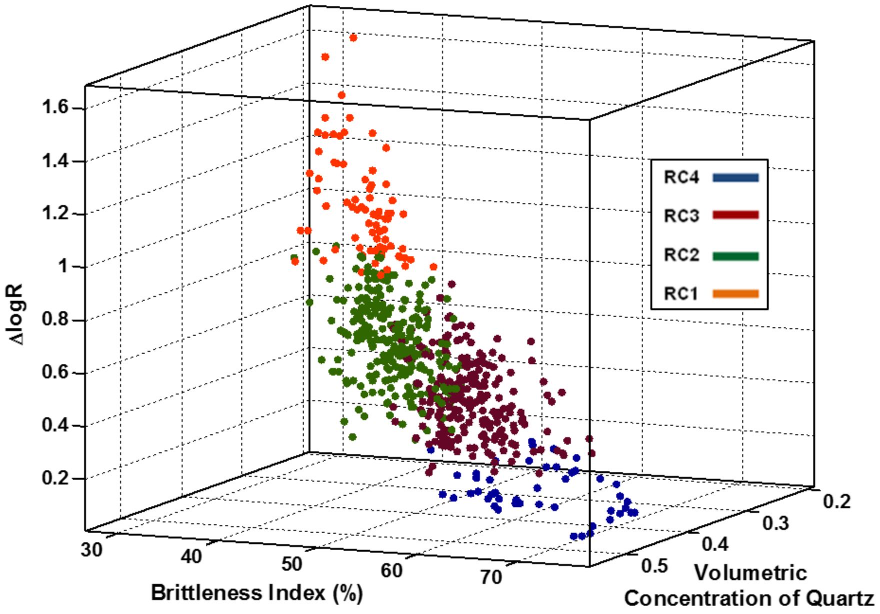

Fig. 6.5—Cross-plot analysis in the Haynesville Shale: 3D cross-plot of ΔlogR, rock brittleness index, and volumetric concentration of quartz. The identified rock classes 1, 2, 3, and 4 are represented by orange, green, maroon, and blue dots, respectively.

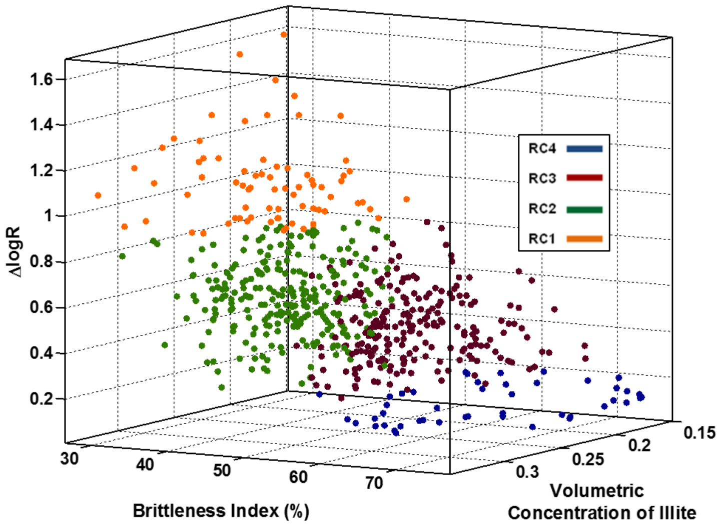

(a)

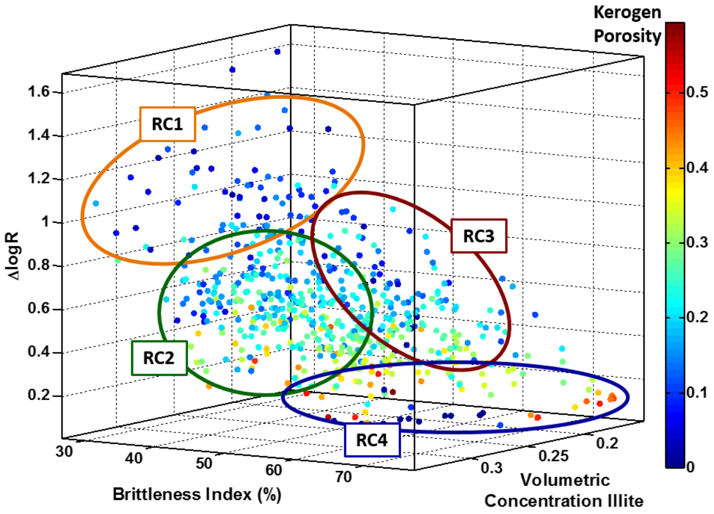

(b)

Fig. 6.6—Cross-plot analysis in the Haynesville Shale. 3D cross-plot of ΔlogR, rock brittleness index, and volumetric concentration of illite where (a) Identified rock classes 1, 2, 3, and 4 are represented by orange, green, maroon, and blue dots, respectively and (b) the color bar shows kerogen porosity (i.e., kerogen pore volume divided by kerogen bulk volume).

Finally, the second and the third rock classification techniques, using two unsupervised artificial neural networks, were applied to execute automatic rock classification. In the second rock classification technique, the artificial neural network was built using an input of well logs (i.e., bulk density, neutron porosity, PEF, apparent deep resistivity, compressional- and shear-wave slowness, and ECS logs) and in the third rock classification technique, the artificial neural network was constructed from an input of well-log-based estimated rock properties (i.e., TOC, Poisson's ratio, Young's modulus, kerogen porosity, total porosity, and volumetric concentrations of calcite, illite, and quartz). I assumed four rock types in this formation, based on the previous field studies (Hammes et al. 2011), available thin sections, and core images.

Fig. 6.7 shows the identified rock classes obtained from the second and the third rock classification techniques and the comparison against the rock classes identified from cross-plot analysis. Furthermore, the outcomes of both the second and the third rock classification techniques were in agreement with the rock classes obtained from 3D cross-plot analysis executed in the first technique. A comparison of the results obtained from the second and the third rock classification techniques shows that inputs of well logs and well-log-based estimated properties to the artificial neural networks, respectively, provided similar rock classes, except in limited depth intervals. There were not enough core measurements available to prove the reliability of the second or the third rock classification technique over the other one in terms of the minor differences in the boundaries detected for different rock classes. However, I expect that having physical properties (i.e., well logs) as inputs to rock classification instead of estimated petrophysical properties can eliminate the uncertainties associated with the assumptions made for well-log interpretation.

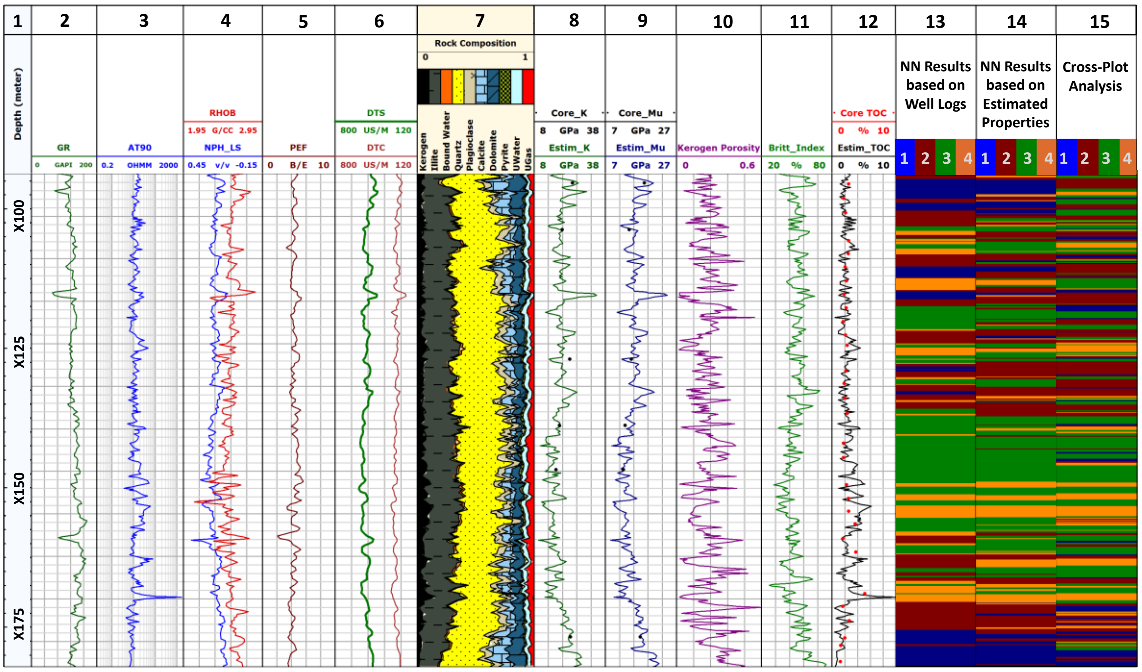

Fig. 6.7—Well-log-based rock classification in the Haynesville Shale. Tracks from left to right include, Track 1-6: depth, GR, apparent deep resistivity, neutron porosity (in water-filled limestone porosity units), bulk density, PEF, and compressional-wave slowness logs; Track 7: volumetric concentrations of mineral constituents; Track 8-9: bulk and shear moduli, compared to core measurements; Track 10: Kerogen porosity (i.e., kerogen pore volume divided by kerogen bulk volume); Track 11-12: well-log-based estimates of TOC and brittleness index; Track 13-14: identified rock classes using the second and the third rock classification techniques, in which well logs and well-log-based estimates of petrophysical and compositional properties are inputs to the artificial neural network, respectively; Track 15: rock classes using the first rock classification technique, 3D cross-plot analysis, after refinement by including kerogen porosity.

Table 6.2 lists the properties of the four identified rock classes in terms of organic richness (ΔlogR), brittleness index, and volumetric concentrations of quartz and illite. I cross-validated the identified rock classes determined from all the three techniques using 45 thin-section images obtained at the depths corresponding to the four identified rock classes. The properties of the identified petrophysical rock classes (Table 6.2) were in agreement with the geological lithofacies described by Hammes and Frébourg (2012) in the Haynesville Shale.

Rock Class	Brittleness Index (%)	ΔlogR	Volumetric Concentration of Quartz	Volumetric Concentration of Illite
RC1	20-55	0.9-1.8	0.19-0.45	0.20-0.35
RC2	30-50	0.23-0.9	0.19-0.45	0.20-0.34
RC3	50-70	0.23-0.9	0.18-0.49	0.15-0.30
RC4	47-80	0-0.23	0.30-0.56	0.15-0.30

Table 6.2—Compositional properties and brittleness index of the identified rock classes in the Haynesville Shale.

Fig. 6.8 shows four thin-section images from the four identified rock types as representatives of those rock types. Based on the results from all three rock classification techniques, rock class 4 represents the most brittle rock, while being the least organic-rich among the other rock classes. Thin-section images at the depth intervals corresponding to rock class 4, confirmed a low concentration of kerogen and lack of natural fractures (Fig. 6.8). Rock class 4 has similar properties to organic-poor facies, as characterized by the lowest TOC among the other lithofacies (Hammes and Frébourg 2012).

The petrophysical and elastic properties obtained for rock class 3 showed that this rock class is organic-rich and brittle in nature, which is confirmed by the presence of kerogen and natural fractures in thin-section images at corresponding depths. The characteristics of rock class 3 were consistent with the most abundant facies, laminated peloidal siliceous facies, with medium range of TOC and brittleness (Hammes and Frébourg 2012).

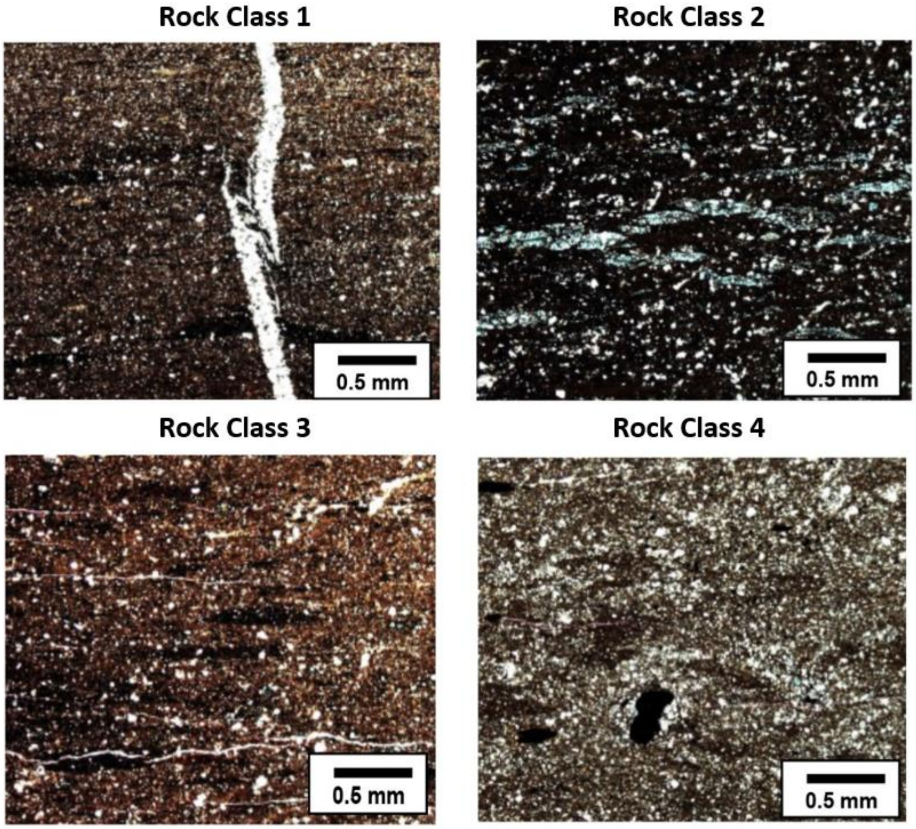

Fig. 6.8—Typical core thin-section images in the four identified rock types. The thin-section representing rock class 1 shows unlaminated organic matter (in black), dispersed randomly between siliciclastic and carbonaceous grains. The thin-section from rock class 2 contains laminations of burrows and fine-grained siliceous grains, organics (black), carbonate, and clay. The thin-section from rock class 3 confirms increased abundance of silt-sized siliceous grains, laminated among peloids. The thin-section from rock class 4 contains the least amount of the organic matter compared to other rock classes.

The outcomes of all three rock classification techniques showed that rock class 2 is less brittle compared to rock classes 3 and 4, whereas the kerogen content in rock class 2 and rock class 3 is similar. Apparent laminations of burrows and fine-grained siliceous grains, organics, carbonate, and clay observed on the thin-section images of rock class 2, confirm that this rock class has similar properties to bioturbated siliceous facies (Hammes and Frébourg 2012).

Finally, rock class 1 is the most organic-rich and the least brittle among all the identified rock classes. Rock class 1 corresponds to unlaminated, peloidal, siliceous facies. The thin-section image of this rock class in Fig. 6.8 shows that organic matter is randomly dispersed in the rock among siliciclastic and carbonate grains.

6.4 Discussion

The main advantage of the three proposed rock classification techniques, compared to the previous ones (Gupta et al. 2012; Hammes and Frébourg 2012; Kale et al. 2010; Popielski et al. 2012) in organic-shale formations, is the incorporation of elastic properties, in addition to petrophysical and compositional properties. Hence, the three integrated rock classification techniques that include elastic properties can be applied to identify sweet spots that are good candidates for fracture treatment.

Among the three rock classification techniques applied, the first one, 3D cross-plot analysis, is the most conventionally used technique. However, in complex organic-rich shale formations, several rock properties, such as elastic properties, volumetric concentrations of minerals, porosity, TOC, and kerogen porosity, should be incorporated for a reliable rock classification. In such cases, the application of conventional 3D cross-plot analysis might be challenging and can be subjected to significant uncertainty. In the second and the third rock classification techniques, the application of unsupervised artificial neural networks allows inclusion of more than three input parameters for an automatic and reliable rock classification. In particular, direct application of well logs, as inputs to the artificial neural network in the second rock classification technique, allows real-time rock classification and can further reduce uncertainties associated with (a) the rock physics models used for petrophysical and compositional evaluation of organic-rich shale formations and (b) the assumed rock-physics models such as resistivity-porosity-saturation models (e.g., Archie's, Waxman-Smits, and dual water models) and effective medium theories.

I estimate elastic moduli by applying an effective medium theory, the self-consistent approximation, which takes into account shapes and volumetric concentrations of rock components. The effective medium theories enable estimation of the elastic moduli where compressional- and shear-wave velocity logs are not available or where they are not reliable. There are, however, limitations associated with these models. The effective medium theories assume isotropic elastic medium of arbitrary distributed components with symmetric idealized shapes. This assumption can introduce error into the assessment of elastic moduli in formations with significant anisotropy, such as the Haynesville Shale, which has a highly-laminated nature. I verified the well-log-based estimates of elastic moduli in the field example using core measurements. Although the number of core measurements were limited in the field example, they were sufficient to validate the estimates in different rock types. Access to more core measurements would be beneficial for better validation of the accuracy of the well-log-based estimates of elastic moduli. Nevertheless, I emphasize that there might be uncertainties in core measurements because of the differences between laboratory and reservoir conditions.

Furthermore, none of the three applied rock classification techniques require calibration against core measurements. Consequently, they are less influenced by the uncertainty associated with core measurements resulting from the use of conventional laboratory techniques.

To further improve the proposed rock classification techniques, assessment of brittleness can be improved by assimilating the stress profile and pore pressure. Moreover, production data, where available, can be integrated to core-measured and well-log-based properties to improve rock classification.

6.5 Conclusions

I proposed three well-log-based rock classification techniques in organic-shale formations that incorporated petrophysical, compositional, and elastic properties of the formation. I applied these three techniques to classify rock types in the Haynesville Shale. I then verified the rock classes using thin-section images and the previously-identified lithofacies in the Haynesville Shale. The rock classes determined using the first rock classification technique, 3D cross-plot analysis, are in agreement with the results of the second and the third rock classification techniques obtained from unsupervised artificial neural networks, with the inputs of well logs and well-log-based estimated properties, respectively. Furthermore, I compared the application of well logs in the second rock classification technique against the use of well-log-based estimates of petrophysical, compositional, and elastic properties as inputs to the third rock classification technique. Rock classification using both the second and the third rock classification techniques resulted in similar rock classes. The results are promising for the direct application of well logs for rock classification, instead of using the estimated properties.

The well-log interpretation results showed that the rock types with the highest organic-richness were the least brittle, because of the ductile nature of the organic matter. Therefore, to ensure a successful fracture treatment, the selection of the best rock types for initiating fractures needs to be enhanced by taking into account both brittleness and organic-richness in rock classification. Furthermore, I showed that assimilating kerogen porosity in rock classification can narrow down the choice of good candidate depth intervals for production and fracture treatment. An advantage of the well-log-based rock classification techniques applied in this chapter is their minimal dependency on core measurements, which makes them reliable tools for characterization of rock classes and heterogeneity in organic-shale formations.

CHAPTER VII

CONCLUSIONS AND RECOMMENDATIONS

This chapter summarizes the main contributions of the research conducted in this dissertation. Main conclusions are reiterated, and recommendations regarding future research are also provided.

7.1 Summary

The objective of this dissertation was to develop an integrated rock classification scheme based on conventional well logs and core data to improve characterization of spatial heterogeneity in carbonate formations. Thus, I introduced an integrated rock classification scheme that incorporates geological attributes, static and dynamic petrophysical properties, mineralogy, and elastic properties, estimated from conventional well logs, for rock classification in complex formations. The application of conventional well logs is emphasized in this dissertation, as the advanced logging tools (e.g., Nuclear magnetic resonance and Formation Micro-Imager) are not available in all wells. The following are the main contributions of the introduced rock classification method compared to previous conventional techniques:

- Integration of depositional and diagenetic attributes for rock classification in carbonate formations by incorporating the impact of the shapes of different pore types and minerals in each geological facies on electrical resistivity measurements and formation elasticity.

- Application of conventional well logs for the depth-by-depth assessment of elastic moduli and interparticle and intraparticle porosity, where acoustic well logs are not available.
- Incorporation of depth-by-depth estimates of elastic properties, as well as petrophysical properties and mineralogy for rock classification in complex formations.
- Characterization of pore-throat radius distribution, obtained from MICP data, using a multi-modal Gaussian function for simultaneous inclusion of pore system attributes corresponding to pore modality, pore volume, and pore connectivity. An advantage of this approach, compared to previous pore typing techniques, is incorporation of no user-defined modality criteria.
- Integration of MICP-based pore types for reliable rock classification in the core and well-log scales.
- Introduction of rock classification techniques with minimal dependence on core measurements, in cases where core data are not adequate for characterizing carbonate heterogeneity.
- Introduction of rock classification methods based on the visible trend of mud filtrate invasion on resistivity well logs with different volumes of investigation to qualitatively take into account the dynamic petrophysical properties, rooted in diagenesis.

7.2 Conclusions

This section lists the conclusions based on the results reported in the dissertation.

7.2.1 Integrated Rock Classification in Carbonate Formations Based on Elastic and Petrophysical Properties Estimated from Conventional Well Logs

i. Petrophysical rock classification can improve selection of candidate zones for fracture treatment by taking into account petrophysical, compositional, and elastic rock properties. Rock classification in conjunction with accurate well-log-based assessment of permeability and water saturation can further improve sweet-spot selection, while reducing the cost, by minimizing the number of perforations and fracture stages.

ii. Outcomes of the integrated rock classification in WELL B showed that the low values of Young's modulus estimated at fracture locations may be the reason for unsuccessful fracture treatment and negligible production from this well.

iii. Estimates of interparticle porosity and Young's modulus in WELL A and WELL B were in agreement with core measurements and thin-section images with 14% and 8% average relative error, respectively.

iv. An improvement of approximately 40% was observed in the assessment of interconnected porosity compared to the initial application of Wyllie's time-average equation.

v. Estimates of permeability and water saturation in WELL A and WELL B were improved by approximately 50% and 20%, respectively, compared to those from conventional techniques.

7.2.2 Characterization of Pore Structure in Carbonate Formations Using a Multi-Modal Gaussian Function for Analyzing the Impact of Pore Systems on Electrical Resistivity

i. A quantitative analysis of MICP-based pore-throat radius distributions was conducted for pore typing in three wells at the SACROC Unit.

ii. The three identified pore types were successfully predicted at core-plug and well-log scales in the SACROC Unit.

iii. The results indicated a correlation coefficient of approximately 57% between the fluid-corrected resistivity measurements and the formation pore types, confirming that the pore structure has a strong influence on the electrical resistivity measurements.

7.2.3 Application of Conventional Well Logs to Characterize Spatial Heterogeneity in Carbonate Formations Required for Prediction of Acid Fracture Conductivity

i. Two well-log-based rock classification techniques with minimal dependency on core data were introduced including (a) a real-time well-log-derived analytical factor and (b) unsupervised artificial neural network.

ii. A third rock classification technique based on supervised artificial neural network was proposed. The supervised network, trained using the available core data, can be applied for prediction of rock classes in uncored wells in the field.

iii. The introduced techniques were successfully applied in two carbonate field examples including Hugoton gas field and Happy Spraberry oil field. The results obtained for Hugoton gas field suggest that supervised neural network provides the most reliable estimates for rock classification and permeability assessment among all the introduced methods, with 54% improvement in permeability assessment. Direct application of well logs provides a more reliable rock classification compared to the application of well-log-based estimates of petrophysical/compositional properties.

iv. In cases with limited core measurements, I recommend the application of the introduced analytical rock quality index or unsupervised artificial neural network for rock classification. In the Hugoton gas field, I observed 50% and 38% relative improvements in permeability assessment using analytical rock quality index and unsupervised artificial neural network for rock classification, respectively.

v. The variogram analysis in both field examples showed that well logs as well as well-log-based estimates of petrophysical/compositional properties can be applied in variogram analysis in lieu of well-log-based permeability estimates, in the lack of enough core data for calibration. This work can be further improved by incorporating the accurate volumes of investigation of different logging tools based on their geometrical configuration in the variogram analysis.

7.2.4 An Investigation on the Impact of Heterogeneity in Carbonate Formations on Fluid Injectivity Loss during Water-Alternating-Gas Injection

i. I investigated the impact of spatial heterogeneity in the distribution of petrophysical rock classes on the injectivity loss experienced during WAG injection in the SACROC Unit.

ii. A new heterogeneity coefficient was introduced for quantifying the spatial variability in the identified petrophysical properties. PCA on petrophysical properties and mineralogy was conducted in conjunction with variogram analysis to validate the introduced heterogeneity coefficient.

iii. The results showed that wells with higher heterogeneity in the distribution of petrophysical rock classes are more likely to experience injectivity abnormalities during WAG injection.

iv. A higher concentration of rock layers with high porosity and permeability, in the wells with heterogeneous distribution of rock classes, can contribute to the occurrence of WAG injectivity abnormalities.

v. The results are promising for successful application of the introduced well-log-based method for pre-selection of candidate wells for WAG injection for successful enhanced oil recovery.

7.2.5 Rock Classification in the Haynesville Shale Based on Petrophysical and Elastic Properties Estimated from Well Logs

i. I proposed three well-log-based rock classification techniques in organic-shale formations that incorporated petrophysical, compositional, and elastic properties of the formation. I successfully applied these three techniques to classify rock types in the Haynesville Shale. The rock classes were verified using thin-section images and the previously-identified lithofacies in the Haynesville Shale.

ii. Rock classes determined using 3D cross-plot analysis are consistent with the results of rock classification using unsupervised artificial neural networks, with the inputs of well logs and well-log-based estimated properties.

iii. Results are promising for the direct application of well logs for rock classification, instead of using the estimated petrophysical and compositional properties.

iv. Well-log interpretation results showed that the rock types with the highest organic-richness were the least brittle, because of the ductile nature of the organic matter. Therefore, to ensure a successful fracture treatment, the selection of the best rock types for initiating fractures needs to be enhanced by taking into account both brittleness and organic-richness in rock classification.

v. Assimilation of kerogen porosity in rock classification can narrow the choice of good candidate depth intervals for production and fracture treatment.

vi. An advantage of the well-log-based rock classification techniques was their minimal dependency on core measurements, which makes them reliable tools for characterization of rock classes and heterogeneity in organic-shale formations, where extensive core data might not be available.

7.3 Recommendations

Although this dissertation focused on addressing some of the challenges in carbonate formations, there remain many unsolved problems in the areas of petrophysics and rock classification in complex formations. The following is a list of possible research avenues for future work that could expand the technical contribution of this dissertation:

i. An extensive analysis of scale-dependency of petrophysical properties and flow characteristics in carbonates reservoirs.
ii. Comprehensive and quantitative assessment of different pore types (intergrain, intercrystal, moldic, interagrain, etc.) in carbonate formations by image analysis of SEM images, thin-sections, and micro-CT and CT scans of core samples and whole-core samples.
iii. Introduction of new upscaling techniques for reliable extrapolation of petrophysical properties from small measurement scales (e.g., pore scale) to log and field scales in heterogeneous formations.
iv. Formulation of a new and reliable resistivity model for the assessment of water saturation in carbonate formations with complex pore systems based on multi-scale analysis of effective porosity, capillarity effects, and electrical resistivity
v. Development of well-log-based techniques for the direct assessment of effective porosity from resistivity well logs.
vi. Integration of production data with geological and petrophysical attributes for rock classification in carbonate formations.
vii. Assimilation of stress profiles and pore pressure measurements in the assessment of mechanical properties and selection of completion candidate zones.
viii. Incorporation of geochemical and geomechanical properties to assess maturity and fracability for rock classification in unconventional reservoirs.

REFERENCES

Ahr, W.M. 2008. *Geology of Carbonate Reservoirs*. Hoboken, New Jersey: Wiley-InterScience.

Al-Farisi, O., Elhami, M., Al-Felasi, A., et al. 2009. Revelation of Carbonate Rock Typing – the Resolved Gap. SPE/EAGE Reservoir Characterization and Simulation Conference, Abu Dhabi, UAE, 19–21 October. SPE-125576. http://dx.doi.org/10.2118/125576-MS.

Alfred, D. and Vernik, L. 2012. A New Petrophysical Model for Organic Shales. *Petrophysics* **54** (3): 240–247.

Amaefule, J.O., Altunbay, M., Tiab, D., et al. 1993. Enhanced Reservoir Description: Using Core and Log Data to Identify Hydraulic (Flow) Units and Predict Permeability in Uncored Intervals/Wells. SPE ATCE, Houston, Texas, USA, 3–6 October. SPE-26436. http://dx.doi.org/10.2118/26436-MS.

Ambrose, R., Hartman, R.C., Diaz-Campos, M., et al. 2010. New Pore-Scale Considerations for Shale Gas in Place Calculations. SPE Unconventional Gas Conference, Pittsburgh, Pennsylvania, USA, 23–25 February. SPE-131772. http://dx.doi.org/10.2118/131772-MS.

Archie, G.E. 1942. The Electrical Resistivity Log as an Aid in Determining Some Reservoir Characteristics. In *Transactions of the AIME,* Vol. 146, 54–62.

Archie, G.E. 1952. Classification of carbonate Reservoir Rocks and Petrophysical Considerations. *AAPG Bulletin* **36**: 278–298.

Babadagli, T. and Al-Salimi, S. 2002. Improvement of Permeability Prediction for Carbonate Reservoirs Using Well Log Data. SPE Asia Pacific Oil and Gas Conference and Exhibition, Melbourne, Australia, 8–10 October. SPE-77889. http://dx.doi.org/10.2118/77889-MS.

Backus, G.E. 1962. Long-Wave Elastic Anisotropy Produced by Horizontal Layering. *Geophysics* **67**, 4427–4440.

Beatty, C.V. 2010. Characterization of Small Scale Heterogeneity for Prediction of Acid Fracture Performance. MS thesis, Texas A&M University, College Station, Texas (August 2010).

Berryman, J.G. 1995. Mixture Theories for Rock Properties. In *Rock Physics and Phase Relations: A Handbook of Physical Constants*. American Geophysical Union: 205–228.

Birch, F. 1960. The Velocity of Compressional Waves in Rocks to 10 Kilobars. *Journal of Geophysical Research* **65** (4): 1083–1102.

Brie, A., Johnson, D.L., and Nurmi, R.D. 1985. Effect of Spherical Pores on Sonic and Resistivity Measurements. SPWLA 26th Annual Logging Symposium, Dallas, Texas, USA, 17–20 June. Paper W.

Brnak, J., Petrich, B., and Konopczynski, M.R. 2006. Application of SmartWell Technology to the SACROC CO_2 EOR Project. SPE/DOE Symposium on Improved Oil Recovery, Tulsa, Oklahoma, USA, 22–26 April. SPE-100117. http://dx.doi.org/10.2118/100117-MS.

Buiting, J.J.M and Clerke, E.A. 2013. Permeability from Porosimetry Measurements: Derivation for a Tortuous and Fractal Tubular Bundle. *J. Pet Sci & Tech* **108**: 267–278.

Caudle, B.H. and Dyes, A.B. 1958. Improving Miscible Displacement by Gas-Water Injection. In *Transactions of the AIME*, Vol. 213, 281–284.

Chicheng, X. and Torres-Verdín, C. 2013. Core-Based Petrophysical Rock Classification by Quantifying Pore-System Orthogonality with a Bimodal Gaussian Density Function. International Symposium of the Society of Core Analysts, Napa Valley, California, USA, 16–19 September.

Choquette, P.W. and Pray, L.C. 1970. Geologic Nomenclature and Classification of Porosity in Sedimentary Carbonates. *AAPG* **54**: 207–250.

Christensen, J.R., Stenby, E.H., and Skauge, A. 2001. Review of WAG Field Experience. *SPE Res Eval & Eng* **4** *(2)*. SPE-71203-PA. http://dx.doi.org/10.2118/71203-PA.

Clerke, E.A., Mueller III, H.W., Phillips, E.C., et al. 2008. Application of Thomeer Hyperbolas to Decode the Pore Systems, Facies and Reservoir Properties of the Upper Jurassic Arab D Limestone, Ghawar Field, Saudi Arabia: A Rosetta Stone Approach. *GeoArabia* **13** (4): 113–160.

Clerke, E.A. 2009. Permeability, Relative Permeability, Microscopic Displacement Efficiency, and Pore Geometry of M_1 Bimodal Pore Systems in Arab D Lime-Stone. *SPE J.* **14** (3): 524–531. SPE-105259-PA. http://dx.doi.org/10.2118/105259-PA.

Clerke, E.A., Allen, D.F., Crary, S.C., et al. 2014. Wireline Spectral Porosity Analysis of The Arab Limestone—From Rosetta Stone to Cipher. SPWLA 55th Annual Logging Symposium, Abu Dhabi, UAE, 18–22 May.

Coates, G. and Denoo, S. 1981. The Producibility Answer Product. The Technical Review, Schlumberger, Houston, 29 June, No. 2: 54.

Conte, R.A. 2014. Integrated Reservoir Characterization of Upper Leonardian Detrital Carbonate Rocks, Glasscock County, Texas, USA. Unpublished M.S. thesis, Texas A&M University, College Station, TX: 89 (December 2014).

Cook, H.E. 1983. Sedimentology of Some Allochthonous Deepwater Carbonate Reservoirs, Lower Permian, West Texas: Carbonate Debris Sheets, Aprons, or Submarine Fans?. *AAPG Bulletin* **63**: 442.

Cover, T.M. and Hart P.E. 1967. Nearest Neighbor Pattern Classification. In *Transactions of the IEEE*, Vol. 13, No. 1: 21–27. doi:10.1109/TIT.1967.1053964.

Darcy, H. 1856. Les Fontaines Publiques de la Ville de Dijon, Dalmont, Paris.

Deng, J., Zhu, D., and Hill, A.D. 2011. A Theoretical Study of Acid Fracture Conductivity under Closure Stress. *SPE Prod & Oper* **26** (1): 9–17. SPE-124755-PA. http://dx.doi.org/10.2118/124755-PA.

Deng, J., Mou, J., Hill, A.D., et al. 2012. A New Correlation of Acid-Fracture Conductivity Subject to Closure Stress. *SPE Prod & Oper* **27** (2): 158–169. SPE-140402-PA. http://dx.doi.org/10.2118/140402-PA.

Dunham, R.L. 1962. Classification of Carbonate Rocks According To Depositional Texture. *American Association of Petroleum Geologists*, Memoir 1: 108–121.

Dubois, M.K., Byrnes, A.P., Bhattacharya, S., et al. 2006. Hugoton Asset Management Project (HAMP): Hugoton Geomodel Final Report: KGS Open File Report.

Dykstra, H. and Parsons, R.L. 1950. The Prediction of Oil Recovery by Water Flood. In *Secondary Recovery of Oil in the United States*, second edition, 160–174. Washington, DC: API.

Embry, A.F. and Klovan, J.E. 1971. A Late Devonian Reef Tract on Northeastern Banks Island, Northwest Territories. *Canadian Petroleum Geology Bulletin* **19**: 730–781.

Gandhi, A., Torres-Verdín, C., Voss, B., et al. 2010. Construction of Reliable Static and Dynamic Multi-Layer Petrophysical Models in Camisea Gas Reservoirs, Peru. SPWLA 51st Annual Logging Symposium, Perth, Australia, 19–23 June. SPWLA-40710.

Gentry, M.D. 2003. Applications of Artificial Neural Networks in the Identification of Flow Units, Happy Spraberry field, Garza County, Texas. MS thesis, Texas A&M University, College Station, Texas (December 2003).

Genty, C., Jensen, J.L., and Ahr, W.M. 2007. Distinguishing Carbonate Reservoir Pore Facies with Nuclear Magnetic Resonance Measurements. *Natural Resources Research* **16** (1): 45–54.

George, B.K., Torres-Verdín, C., Delshad, M., et al. 2003. A Case Study Integrating the Physics of Mud-filtrate Invasion with the Physics of Induction Logging: Assessment of In-situ Hydrocarbon Saturation in the Presence of Deep Invasion and Highly Saline Connate Water. SPWLA 44th Annual Logging Symposium, Galveston, Texas, 22–25 June. Paper K.

Goggin, D.J., Chandler, M.A., Kocurek, G., et al. 1992. Permeability Transects of Eolian Sands and Their Use in Generating Random Permeability Fields. *SPE J.* **7** (1)*:* 7–16. SPE-19586-PA. http://dx.doi.org/10.2118/19586-PA.

Gomez, C., Scotellaro, C., Vanorio, T., et al. 2009. Effective Medium Modeling of Laboratory Velocity and Resistivity Data on Carbonates from Apulia Platform, Italy. SEG Annual Meeting, Houston, Texas, USA, 25–30 October.

Gorell, S.B. 1990. Implications of Water-Alternate-Gas Injection, for Profile Control and Injectivity. SPE/DOE Enhanced Oil Recovery Symposium, Tulsa, Oklahoma, USA, 22–25 April. SPE-20210. http://dx.doi.org/10.2118/20210-MS.

Gottlib-Zeh, S. 2000. Synthèse Des Données Géologiques et Pétrophysiques Acquises en Forages Pétroliers à L'Aide de Traitements Statistiques et Neuronaux. Applications aux dépôts turbiditiques et aux plates-formes mixtes. Doctoral Thesis, Montpellier University, Montpellier, France.

Gringarten, E. and Deutsch, C.V. 1999. Methodology for Variogram Interpretation and Modeling for Improved Reservoir Characterization. SPE ATCE, Houston, Texas, 3–6 October. SPE-56654. http://dx.doi.org/10.2118/56654-MS.

Guha, S., Rastogi, R., and Shim, K. 1998. Cure: An Efficient Clustering Algorithm for Large Databases. Proc., ACM SIGMOD International Conference on Management of data, New York, June, Vol. 27, 73–84.

Gupta, N., Rai, C.S., and Sondergeld, C.H. 2012. Integrated Petrophysical Characterization of The Woodford Shale in Oklahoma. SPWLA 53rd Annual Logging Symposium, Cartagena, Colombia, 16–20 June. Paper LLL.

Hammel, B.S. 1996. High Resolution Reservoir Characterization of the Permian (upper Leonardian) Spraberry Formation, Happy Spraberry Field, Garza County, Texas. Unpublished MS thesis, Texas A&M University, College Station, Texas.

Hammes, U. and Frébourg, G. 2012. Haynesville and Bossier Mudrocks: A Facies and Sequence Stratigraphic Investigation, East Texas and Louisiana. *Marine and Petroleum Geology* **31** (1): 8–26.

Hammes, U., Hamlin, H.S., and Ewing, T.E. 2011. Geologic Analysis of The Upper Jurassic Haynesville Shale in East Texas and West Louisiana. *AAPG Bulletin* **95**: 1643–1666.

Han, W.S., Mcpherson, B.J., Lichtner, P.C., et al. 2010. Evaluation of Trapping Mechanisms in Geologic CO_2 Sequestration: Case Study of SACROC Northern Platform, a 35-Year CO_2 Injection Site. *American Journal of Science* **310**: 282–324. doi: 10.2475/04.2010.03.

Harvey, M.T. Jr., Shelton, J.L., and Kelm, C.H. 1977. Field Injectivity Experiences With Miscible Recovery Projects Using Alternate Rich-Gas and Water Injection. *Journal of Petroleum Technology*, September: 1051. SPE-4738-PA. http://dx.doi.org/10.2118/4738-PA.

Heidari, Z., Hamman, J.G., Day, P.I., et al. 2011. Assessment of Movable Gas Saturation and Rock Typing Based on the Combined Simulation of Petrophysical Borehole Measurements. SPWLA 52nd Annual Logging Symposium, The Woodlands, Colorado Springs, 14–18 May. Paper NN.

Heidari Z. and Torres-Verdín C. 2012. Estimation of Dynamic Petrophysical Properties of Water-Bearing Sands Invaded with Oil-Base Mud from Multi-Physics Borehole Geophysical Measurements. *Geophysics* **77** (6).

Huang, E.T.S. and Holm, L.W.1988. Effect of WAG Injection and Rock Wettability on Oil Recovery during CO_2 Flooding. *SPE Res Eval & Eng* **February**: 119. SPE-15491-PA. http://dx.doi.org/10.2118/15491-PA.

Isaaks, E.H. and Srivastava, R.M. 1989. *An Introduction to Applied Geostatistics*. NewYork: Oxford University Press, Inc.

Jackson, D.D., Andrews, G.L., and Claridge, E.L. 1985. Optimum WAG Ratio vs. Rock Wettability in CO_2 Flooding. SPE ATCE, Las Vegas, Nevada, USA, 22–25 September. SPE-14303. http://dx.doi.org/10.2118/14303-MS.

Jiang, M. and Spikes, K.T. 2011. Pore-Shape and Composition Effect on Rock-Physics Modeling in the Haynesville Shale. The 81st Annual International Meeting, SEG: 2079–2083. doi: 10.1190/1.3627618.

Jennings, J.W. and Lucia, F.J. 2003. Predicting Permeability from Well Logs in Carbonates with a Link to Geology for Inter-well Permeability Mapping. *SPE Res Eval & Eng* **6** (4): 215–225. SPE-84942-PA. http://dx.doi.org/10.2118/84942-PA.

Kale, S., Rai, C.S., and Sondergeld, C.H. 2010. Rock Typing in Gas Shales. SPE ATCE, Florence, Italy, 19–22 September. SPE-134539. http://dx.doi.org/10.2118/134539-MS.

Kane, A.V. 1979. Performance Review of a Large-Scale CO_2-WAG Enhanced Recovery Project, SACROC Unit Kelly-Snyder Field. *Journal of Petroleum Technology* **31** (2). SPE-7091-PA. http://dx.doi.org/10.2118/7091-PA.

Katz, A.J. and Thompson, A.H. 1986. *Quantitative Prediction of Permeability in Porous Rock*. Phys. Rev. B, 1 December, 34: 8179.

Kazatchenko, E., Markov, M., and Mousatov, A. 2004. Joint Modeling of Acoustic Velocities and Electrical Conductivity from Unified Microstructure of Rocks. *Journal of Geophysical Research* **109**: 1–8.

Iverson, K.E. 1962. *A Programming Language*, New York. Wiley, 11.

King, G. 2010. Thirty Years of Gas Shale Fracturing: What Have We Learned?. SPE ATCE, Florence, Italy, 19–22 September. SPE-133456. http://dx.doi.org/10.2118/133456-MS.

Kittridge, M.G., Lake, L.W., Lucia, J.F., et al. 1990. Outcrop/Subsurface Comparisons of Heterogeneity in the San Andres Formation. *SPE Form Eval* **5** (3): 233–240. SPE-19596-PA. http://dx.doi.org/10.2118/19596-PA.

Kohonen, T. 2001. The Self-Organizing Map. *Springer Series in Information Sciences*. Vol. 30, No. 3, 501.

Kumar, M. and Han, D.H. 2005. Pore Shape Effect on Elastic Properties of Carbonate Rocks. SEG Annual Meeting, Houston, Texas, USA, 6–11 November.

Langston, M.V., Hoadley, S.F., and Young, D.N. 1988. Definitive CO_2 Flooding Response in the SACROC Unit. SPE Enhanced Oil Recovery Symposium, Tulsa, Oklahoma, USA, 16–21 April. SPE-17321. http://dx.doi.org/10.2118/17321-MS.

Layman, J.M. 2002. Porosity Characterization Utilizing Petrographic Image Analysis: Implications for Identifying and Ranking Reservoir Flow Units, Happy Spraberry Field, Garza County, Texas. Unpublished MS thesis, Texas A&M University, College Station, Texas.

Lee, S.H. and Datta-Gutpa, A. 2002. Electrofacies Characterization and Permeability Predictions in Complex Reservoirs. *SPE Res Eval & Eng* **5** (3): 237–248. SPE-78662-PA. http://dx.doi.org/10.2118/78662-PA.

Leslie, H.D. and Mons, F. 1982. Sonic Waveform Analysis. SPWLA 23th Annual Logging Symposium, Corpus Christi, Texas, USA, 6–9 July.

Levenberg, K. 1944. A Method for the Solution of Certain Non-Linear Problems in Least Squares. *Quarterly of Applied Mathematics* **2**: 164–168.

Leverett, M.C. 1941. Capillary Behavior in Porous Solids. In *Transactions of the AIME*, Vol. 142, No. 1, 159–172.

Lloyd, S.P. 1982. Least Squares Quantization in PCM. In *Transactions of the IEEE on Information Theory*, Vol. 28, 129–137.

Lucia, F.J. 1995. Rock-Fabric/Petrophysical Classification of Carbonate Pore Space for Reservoir Characterization. *AAPG Bulletin* **79** (9): 1275–1300.

Lucia, F.J. 2007. *Carbonate Reservoir Characterization*. Berlin, Germany: Springer-Verlag.

MacQueen, J.B. 1967. Some Methods for Classification and Analysis of Multivariate Observations. In *Proceedings of 5-th Berkeley Symposium on Mathematical Statistics and Probability*, Berkeley, University of California Press, Vol. 1: 281–297

Markov, M., Levine, V., Mousatov, A. et al. 2005. Elastic Properties of Double-Porosity Rocks Using the Differential Effective Medium Model. *Geophysical Prospecting* **53**: 733–754.

Marquardt, D. 1963. An Algorithm for Least-Squares Estimation of Nonlinear Parameters. *SIAM Journal of Applied Mathematics* **11**: 431–441.

Marzouk, I., Takezaki, H., and Miwa, M. 1995. Geologic Controls on Wettability of Carbonate Reservoirs, Abu Dhabi, U.A.E. SPE Middle East Oil Show, Bahrain, 11–14 March. SPE-29883. http://dx.doi.org/10.2118/29883-MS.

Mavko, G., Mukerji, T., and Dvorkin, J. 2009. *The Rock Physics Handbook*, second edition. New York: Cambridge Univ. Press.

Mathisen, T., Lee, S.H., and Datta-Gutpa, A. 2003. Improved Permeability Estimates in Carbonate Reservoirs Using Electrofacies Characterization: A Case Study of the North Robertson Unit, West Texas. *SPE Res Eval & Eng* **6** (3): 176–184. SPE-84920-PA. http://dx.doi.org/10.2118/84920-PA.

Mazingue-Desailly, V.P. 2004. Assessing the Influence of Diagenesis on Reservoir Quality: Happy Spraberry Field, Garza County, Texas. MS thesis, Texas A&M University, College Station, Texas (May 2004).

Miranda, L. J., Torres-Verdín, C., and Lucia, J. 2009. Modeling Mud-filtrate Invasion Effects on Resistivity Logs to Estimate Permeability of Vuggy and Fractured Carbonate Formations. SPE EUROPEC Conference, Amsterdam, Netherlands, 8–11 June. SPE-121136. http://dx.doi.org/10.2118/121136-MS.

Mohaghegh, S., Balan, B., and Amer, S. 1997. Permeability Determination from Well Log Data. *SPE Form Eval* **12** (3)*:* 170–174. SPE-30978-PA. http://dx.doi.org/10.2118/30978-PA.

Montaut, A., Sayar, P., and Torres-Verdin, C. 2013. Detection and Quantification of Rock Physics Properties for Improved Hydraulic Fracturing in Hydrocarbon-Bearing Shale. SPWLA 54th Annual Logging Symposium, New Orleans, Louisiana, USA, 22–26 June. Paper KK.

Mou, J., Zhu, D., and Hill, A.D. 2011. New Correlations of Acid-Fracture Conductivity at Low Closure Stress Based on the Spatial Distributions of Formation Properties. *SPE Prod & Oper* **26** (2): 195–202. SPE-131591-PA. http://dx.doi.org/10.2118/131591-PA.

Mullins, H.T. and Cook, H.E. 1986. Carbonate Apron Models: Alternations to the Submarine Fan Model for Paleoenvironmental Analysis and Hydrocarbon Exploration. *Sedimentary Geology* **48**: 37–79.

Nimmo, J.R. 2004. Porosity and Pore Size Distribution, In Encyclopedia of Soils in the Environment. *Elsevier* **3**: 295–303.

Oeth, C., Hill, A.D., and Zhu, D. 2011. Characterization of Small Scale Heterogeneity to Predict Acid Fracture Performance. SPE Hydraulic Fracturing Technology Conference, The Woodlands, Texas, 24–26 January. SPE-140336. http://dx.doi.org/10.2118/140336-MS.

Oeth, C., Hill, A.D., and Zhu, D. 2013. Acid Fracturing: Fully 3D Simulation and Performance Prediction. SPE Hydraulic Fracturing Technology Conference, The

Woodlands, Texas, USA, 4–6 February. SPE-163840. http://dx.doi.org/10.2118/163840-MS.

Olson, T.M., Babcock, J. A., Prasad, K.V.K., et al. 1997. Reservoir Characterization of the Giant Hugoton Gas Field, Kansas. *AAPG Bulletin* **81** (11): 1785–1803.

Olson, T.M. 1998. Porosity and Permeability Prediction in Low-permeability Gas Reservoirs from Well Logs Using Neural Networks. SPE Rocky Mountain Regional/Low-Permeability Reservoirs Symposium, Denver, Colorado, 5–8 April. SPE-39964. http://dx.doi.org/10.2118/39964-MS.

Osborn, J.A. 1945. Demagnetizing Factors of the General Ellipsoid. *Physical Review* **67** (11): 351–357.

Palabos. 2013. The Palabos software project: http://www.palabos.org/documentation/tutorial/permeability.html.

Parker, M., Buller, D., Petre, E., et al. 2009. Haynesville Shale-Petrophysical Evaluation. SPE Rocky Mountain Petroleum Technology Conference, Denver, Colorado, USA, 14–16 April. SPE-122937. http://dx.doi.org/10.2118/122937-MS.

Passey, Q.R., Creaney, S., Kulla, J.B., et al. 1990. A Practical Model for Organic Richness from Porosity and Resistivity Logs. *AAPG Bulletin* **74** (12): 1777–1794.

Peters, E.J. 2012. *Advanced Petrophysics*, Volumes 1 and 2. Austin, Texas: Greenleaf Book Group.

Pittman, E.D. 1992. Relationship of Porosity and Permeability to Various Parameters Derived from Mercury Injection- Capillary Pressure Curves for Sandstone. *AAPG Bulletin* **76** (2): 191–198.

Playton, T.E., Janson, X., and Kerans, C. 2010. Carbonate Slopes, N.P. James and R.W. Dalrymple, eds., *Facies Models 4*. Geological Association of Canada: 449–476.

Popielski, A.C., Heidari, Z., and Torres-Verdin, C. 2012. Rock Classification from Conventional Well Logs in Hydrocarbon-Bearing Shale. SPE ATCE, San Antonio, Texas, USA, 8–10 October. SPE-159255. http://dx.doi.org/10.2118/159255-MS.

Potter, G.F. 1987. The Effects of CO_2 Flooding on Wettability of West Texas Dolomitic Formations. SPE ATCE, Dallas, USA, 27–30 September. SPE-16716. http://dx.doi.org/10.2118/16716-MS.

Purcell, W.R. 1949. Capillary pressures - Their Measurement Using Mercury and The Calculation of Permeability. In *Transactions of the AIME*, Vol. 186: 39–48.

Quirein, J., Witkowsky, J., Truax, J., et al. 2010. Integrating Core Data and Wireline Geochemical Data for Formation Evaluation and Characterization of Shale Gas Reservoirs. SPWE ATCE, Florence, Italy, 19–22 September. SPE-134559. http://dx.doi.org/10.2118/134559-MS.

Rickman, R., Mullen, M., Petre, E., et al. 2008. A Practical Use of Shale Petrophysics for Stimulation Design Optimization: All Shale Plays Are Not Clones of The Barnett Shale. SPE ATCE, Denver, Colorado, USA, 21–24 September. SPE-115258. http://dx.doi.org/10.2118/115258-MS.

Remy, N., Boucher, A., Wu, J., et al. 2008. *SGeMS: Stanford Geostatistical Modeling Software Version 2.1 [computer software]*. Palo Alto, California: Board of Trustees of Stanford University.

Rickman, R., Mullen, M., Petre, E., et al. 2008. A Practical Use of Shale Petrophysics for Stimulation Design Optimization. SPE ATCE, Denver, Colorado, USA, 21–24 September. SPE-115258. http://dx.doi.org/10.2118/115258-MS.

Rogers, J.D. and Grigg, R.B. 2001. A Literature Analysis of the WAG Injectivity Abnormalities in the CO_2 Process. *SPE Res Eval & Eng* **4** (5). SPE-73830-PA. http://dx.doi.org/10.2118/73830-PA.

Roper, M.K., Cheng, C.T., Varnon, J.E., et al. 1992. Interpretation of a CO_2 WAG Injectivity Test in the San Andres Formation Using a Compositional Simulator. SPE/DOE Symposium on Enhanced Oil Recovery, Tulsa, Oklahoma, USA, 22–24 April. SPE-24163. http://dx.doi.org/10.2118/24163-MS.

Roy, E. 1998. High Resolution Mapping of Flow Units for Enhanced Recovery Program Planning, Happy Spraberry Lime Field, Garza County, Texas. Unpublished MS thesis, Texas A&M University.

S-Plus 2000 Guide to Statistics.Vol. 2. Data Analysis Products Division, MathSoft, Seattle, Washington.

Salazar, J.M., Torres-Verdín, C., Alpak, F.O., et al. 2006. Estimation of Permeability from Array Induction Measurements: Applications to the Petrophysical Assessment of Tight-gas Sands. *Petrophysics* **47** (6): 527–544.

Saneifar, M., Aranibar, A., and Heidari, Z. 2014a. Rock Classification in the Haynesville Shale Based on Petrophysical and Elastic Properties Estimated from Well Logs. *SEG Interpretation Journal* **3** (1): SA65–SA75. http://dx.doi.org/10.1190/INT-2013-0198.1.

Saneifar, M., Conte, R., Valdes C.C., et al. 2015. Integrated Rock Classification in Carbonate Formations Based on Elastic and Petrophysical Rock Properties Estimated from Conventional Well Logs. Paper BLTN14-167 accepted for publication in the *AAPG Bulletin*.

Saneifar, M., Heidari, Z., and Hill, A.D. 2014b. Application of Conventional Well Logs to Characterize Spatial Heterogeneity in Carbonate Formations Required for Prediction of Acid-Fracture Conductivity. Paper SPE-173183-PA accepted for publication in the *SPE Production and Operations Journal*. http://dx.doi.org/10.2118/173183-PA.

Saner, S., Kissami, M., and Al Nufaili, S. 1997. Estimation of Permeability From Well Logs Using Resistivity and Saturation Data. *SPE Form Eval* **12** (1): 27–31. SPE-26277-PA. http://dx.doi.org/10.2118/26277-PA.

Schalger, W., and Chermak, A., 1979, Sediment Facies of Platform-Basin Transition, Tongue of the Ocean, Bahamas: *SEPM* **27**: 193–208.

Schlumberger. 1989. Log Interpretation, Principles, and Applications. Schlumberger Educational Services.

Schmalz, J.P. and Rahme, H.S. 1950. The Variation in Water Flood Performance with Variation in Permeability Profile. *Producers Monthly* **15**: 9–12.

Schneider, F.N. and Owens, W.W. 1976. Relative Permeability Studies of Gas-Water Flow Following Solvent Injection in Carbonate Rocks. *SPE Journal* **16** (1). SPE-5554-PA. http://dx.doi.org/10.2118/5554-PA.

Serra, O. and Abbott, H.T. 1980. The Contribution of Logging Data to Sedimentology and Stratigraphic. Paper SPE-9270-PA, *SPE J.* **22** (1): 117–131. http://dx.doi.org/10.2118/9270-PA.

Silva, F.P.T, Ghano, A.A., Al Mansoori, A., et al. 2002. Rock Type Constrained 3D Reservoir Characterization and Modeling. Abu Dhabi International Petroleum Exhibition and Conference, Abu Dhabi, UAE, 13–16 October. SPE-78504. http://dx.doi.org/10.2118/78504-MS.

Skalinski, M., Gottlib-Zeh, S., and Moss, B. 2005. Defining and Predicting Rock Types in Carbonates – Preliminary Results from an Integrated Approach Using Core and Log Data in Tengiz Field. SPWLA 46th Annual Logging Symposium, New Orleans, Louisiana, USA, June 26–29. Paper Z.

Skalinski, M. and Kenter, J. 2014. Carbonate Petrophysical Rock Typing: Integrating Geological Attributes and Petrophysical Properties while Linking with Dynamic Behavior. *The Geological Society of London* **406**: 229–259. http://dx.doi.org/10.1144/SP406.6.

Sok, R.M., Knackstedt, M.A, Varslot T., et al. 2010. Pore Scale Characterization of Carbonates at Multiple Scales: Integration of Micro-CT, BSEM, and FIBSEM. *Petrophysics* **51** (6): 379–387.

Spath, H. Cluster Dissection and Analysis: Theory. 1985. *FORTRAN Programs, Examples*. Translated by J. Goldschmidt. New York: Halsted Press.

Spencer, D.W. 1963. The Interpretation of Grain Size Distribution Curves of Clastic Sediments. *Journal of Sedimentary Petrology* **33** (1): 180–190.

Surguchev, L.M., Korbol, R., and Krakstad, O.S. 1992. Optimum Water Alternate Gas Injection Schemes for Stratified Reservoir. SPE ATCE, Washington, DC, USA, 4–7 October. SPE-24646. http://dx.doi.org/10.2118/24646-MS.

Thomeer, J.H.M. 1960. Introduction of a Pore Geometrical Factor Defined by the Capillary Pressure Curve. *Journal of Petroleum Technology*. **12** (3): 73–77. SPE-1324-G http://dx.doi.org/10.2118/1324-G.

Timur, A. 1968. An Investigation of Permeability and Porosity, and Residual Water Saturation Relationship for Sandstone Reservoirs. The Log Analyst, July–August, 4: 8.

Wang, Z.Z. 2001. Fundamentals of Seismic Rock Physics. *Geophysics* **66** (2): 398–412.

Ward, J.H. 1963. Hierarchical Grouping to Optimize an Objective Function. *Journal of the American Statistical Association* **58**: 236–244.

Worthington, P.F. 2004. The Effect of Scale on The Petrophysical Estimation of Intergranular Permeability. *Petrophysics* **45** (1).

Wu, T.T. 1966. The Effect of Inclusion Shape on the Elastic Moduli of a Two-Phase Material. *International Journal of Solids Structures* **2** (1): 219–227.

Wyllie, M.R.J. and Rose, W.D. 1950. Some Theoretical Considerations Related to the Quantitative Evaluation of the Physical Characteristics of Reservoir Rock from Electric Log Data. In *Transactions of the AIME*, Vol. 189, 105.

Xu, C. and Torres-Verdín, C. 2012. Saturation-Height and Invasion Consistent Hydraulic Rock Typing Using Multi-Well Conventional Logs. SPWLA 53rd Annual Logging Symposium, Cartagena, Colombia, 16–20 June. SPWLA-071.

Xu, C., Heidari, Z., and Torres-Verdín, C. 2012. Rock Classification in Carbonate Reservoirs Based on Static and Dynamic Petrophysical Properties Estimated from Conventional Well Logs. SPE ATCE, San Antonio, Texas, 8–10 October. SPE-159991. http://dx.doi.org/10.2118/159991-MS.

Xue, G., Datta-Gupta, A., Valko, P., et al. 1997. Optimal Transformations for Multiple Regression: Application to Permeability Estimation from Well Logs. *SPE Form Eval* **12** (2): 85–94. SPE-35412-PA. http://dx.doi.org/10.2118/35412-PA.

Yao, C.Y. and Holditch, S.A. 1993. Estimating Permeability Profiles Using Core and Log Data. SPE Eastern Regional Conference and Exhibition, Pittsburgh, Pennsylvania, 2–4 November. SPE-26921. http://dx.doi.org/10.2118/26921-MS.

Ye, S.J., Rabiller, P., and Keskes, N. 1998. Automatic High Resolution texture Analysis on Borehole Imagery. SPWLA 39th Annual Logging Symposium, Colorado, USA, May 26–28. Paper M.

Zhan, X., Fullmer, S.M., Lu, C., et al. 2012. Study Geophysical Response of Middle East Carbonate Reservoir Using Computational Rock Physics Approach. SEG Annual Meeting, Las Vegas, Nevada, USA, 4–9 November.

APPENDIX

LIST OF PUBLICATIONS

The research conducted in this Ph.D. dissertation was published in several peer-reviewed journal and conference papers, as listed in the following sections.

Refereed Journal Publications

Saneifar, M., Conte, R., Valdes, C.C., et al. 2015. Integrated Rock Classification in Carbonate Formations Based on Elastic and Petrophysical Rock Properties Estimated from Conventional Well Logs. Paper BLTN14-167 accepted for publication in the *AAPG Bulletin*.

Saneifar, M., Heidari, Z., and Hill, A.D. 2014. Application of Conventional Well Logs to Characterize Spatial Heterogeneity in Carbonate Formations Required for Prediction of Acid-Fracture Conductivity. Paper SPE-173183-PA accepted for publication in the *SPE Production and Operations Journal*. http://dx.doi.org/10.2118/173183-PA.

Saneifar, M., Aranibar, A., and Heidari, Z. 2014. Rock Classification in the Haynesville Shale Based on Petrophysical and Elastic Properties Estimated from Well Logs. *SEG Interpretation Journal* **3** (1): SA65–SA75. http://dx.doi.org/10.1190/INT-2013-0198.1.

Refereed Conference Proceedings

Saneifar, M. and Heidari, Z. 2015. An investigation on the Impact of Heterogeneity in Carbonate Formations on Fluid Injectivity Loss during Water-Alternating-Gas Injection. Paper SPE-175064-MS to be presented at the SPE ATCE, Houston, Texas, USA, 28–30 September.

Oyewole, E., Saneifar, M., and Heidari, Z. 2015. Multi-Scale Characterization of Pore Structure in Carbonate Formations for Enhanced Assessment of Petrophysical and Compositional Properties. Paper to be presented at the SPWLA 56th Annual Symposium in Long Beach, California, USA, 18–22 July.

Saneifar, M., Conte, R., Valdes, C.C., et al. 2014. Integrated Rock Classification in Carbonate Formations Based on Elastic and Petrophysical Rock Properties Estimated from Conventional Well Logs. SPWLA 55th Annual Symposium, Abu Dhabi, UAE, 18–22 May. Paper B.

Saneifar, M., Aranibar, A., and Heidari, Z. 2013. Rock Classification in the Haynesville Shale-Gas Formation Based on Petrophysical and Elastic Rock Properties Estimated from Well Logs. SPE ATCE, New Orleans, Louisiana, USA, 30 September–2 October. SPE-166328. http://dx.doi.org/10.2118/166328-MS.

Aranibar, A., Saneifar, M., and Heidari, Z. 2013. Petrophysical Rock Typing in Organic-Rich Source Rocks Using Well Logs. Unconventional Resources

Technology Conference, Denver, Colorado, USA, 12–14 August. SPE-168913-MS. http://dx.doi.org/10.1190/URTEC2013-117.

Saneifar, M., Heidari, Z., and Hill, A.D. 2013. Permeability Assessment in Carbonate Formations Using Conventional Well Logs Required for Prediction of Acid Fracture Conductivity. SPWLA 54th Annual Symposium, New Orleans, Louisiana, USA, 22–26 June. Paper R.